

Abstract of thesis entitled

Search for chargino and neutralino production in final states with two same-sign leptons, jets and missing transverse momentum at $\sqrt{s} = 13$ TeV with the ATLAS detector

Submitted by

Cheuk Yee LO

for the degree of Doctor of Philosophy
at The University of Hong Kong
in November 2018

The Standard Model in particle physics has successfully explained almost all experimental results in the microscopic scale with high accuracy. However, the nature of the dark matter and the hierarchy problem of Higgs mass are still the unanswered questions. Supersymmetry (SUSY) is one of the most promising theories beyond the Standard Model, that might answer these questions. In the recent searches for supersymmetric particles that are involved in strong interaction, their masses are above 1 TeV. This might suggest that the pair production of electroweak gauginos is a dominant SUSY production process at the Large Hadron Collider (LHC). Also, the recent upgrade that the center-of-mass energy of the proton-proton collisions \sqrt{s} has increased to 13 TeV, opened a new phase of exploration for SUSY.

In this thesis, a search is presented for the electroweak pair production of a chargino and a neutralino ($p + p \rightarrow \tilde{\chi}_1^\pm + \tilde{\chi}_2^0$), where the chargino decays to the lightest neutralino and a W boson ($\tilde{\chi}_1^\pm \rightarrow \tilde{\chi}_1^0 + W$), and the second lightest

neutralino decays to the lightest neutralino and a Standard Model like Higgs boson with mass 125 GeV ($\tilde{\chi}_2^0 \rightarrow \tilde{\chi}_1^0 + h$). The final state with two same-sign leptons, jets and missing transverse momentum are considered in this search. The two leptons come from the leptonically decay of the W boson and the Higgs boson with the decay modes of $h \rightarrow WW$, $h \rightarrow \tau\tau$ or $h \rightarrow ZZ$. This analysis is based on the proton-proton collision data delivered by the LHC at $\sqrt{s} = 13$ TeV with the ATLAS detector. The integrated luminosity of data is 36.1 fb^{-1} .

The exclusion limits for the masses of $\tilde{\chi}_1^\pm$ and $\tilde{\chi}_2^0$ are extended up to 245 GeV, while the exclusion limits for the mass of $\tilde{\chi}_1^0$ are extended up to 40 GeV, with 95% confidence level, in the context of a simplified supersymmetric model.

An abstract of exactly 286 words

**Search for chargino and neutralino
production in final states with two
same-sign leptons, jets and missing
transverse momentum at $\sqrt{s} = 13$ TeV
with the ATLAS detector**

by

Cheuk Yee LO

A thesis submitted in partial fulfilment of the requirements for
the Degree of Doctor of Philosophy
at The University of Hong Kong.

November 2018

Declarations

I declare that this thesis represents my own work, except where acknowledgement is made, and that it has not been previously included in a thesis, dissertation or report submitted to this University or to any other institution for a degree, diploma or other qualifications.

Signed
.....

Cheuk Yee LO

Acknowledgments

I would like to thank my supervisor Tu Yanjun for giving me the opportunity to do the research, for her support on my research and for her guidance and suggestions on my analysis.

I would like to thank Zhang Dongliang. He taught me almost everything on the analysis, including linux shell, ROOT, vim, svn, RootCore, dq2, rucio, grid, panda, latex, trigger system, GRL, and more. He also help our group to write the multiLepSearch package to generate the ntuple.

I would like to thank my postdoc Daniela Paredes. She gave a lot of suggestions on my analysis. She also help our group to do analysis.

Contents

Abstract	i
Title Page	iii
Declaration	iv
Acknowledgments	v
Contents	vi
List of Figures	ix
List of Tables	xiv
List of Abbreviations and Symbols	xvi
1 Theoretical Background	1
1.1 Introduction	1
1.2 Standard Model	1
1.2.1 Matter particles	2
1.2.2 Forces and carrier particles	3
1.2.3 Feynman diagram	3
1.3 Limitation of Standard Model	3
1.3.1 Dark matter	3
1.3.2 Hierarchy problem	5
1.3.3 Unification of forces	6
1.4 Supersymmetry	6
1.4.1 Minimal Supersymmetric Standard Model	7
1.5 Signal scenario	9

2 Experimental Setup	12
2.1 Introduction	12
2.2 The Large Hadron Collider	12
2.3 ATLAS detector	14
2.3.1 The coordinate system and basic variables	16
2.3.2 The magnetic system	18
2.3.3 The inner detector	19
2.3.4 Calorimeter	24
2.3.5 Muon Spectrometer	32
3 Dataset inputs and event selection	36
3.1 Dataset inputs	36
3.1.1 Data samples	36
3.1.2 MC samples	36
3.2 Pre-selection and event cleaning	38
3.3 Trigger strategy	39
3.4 Object definitions	39
3.4.1 Elections	40
3.4.2 Muons	40
3.4.3 Jets	40
3.4.4 Missing transverse momentum	41
3.4.5 Overlap Removal	41
4 Signal Region	43
4.1 Discriminant variables	43
4.2 Signal region optimization	45
4.2.1 Pre-selection	47
4.2.2 Samples	47
4.2.3 Running for optimization	50
4.2.4 Results for optimization	50
5 Background estimation	55
5.1 charge flip background	55
5.1.1 Sources for charge flip background	55
5.1.2 Likelihood method	57

5.1.3	Background subtraction	59
5.1.4	Results without systematic uncertainty	59
5.1.5	Systematic uncertainties due to background subtraction . .	61
5.1.6	Systematic uncertainties due to likelihood method	61
5.1.7	Results with total uncertainties	63
5.1.8	MC validation	64
5.2	Fake lepton background	66
5.2.1	Sources for fake lepton background	66
5.2.2	Matrix method	67
5.2.3	Measurement of real efficiencies	71
5.2.4	Measurement of fake efficiencies	73
5.2.5	Validation for the fake lepton background	73
6	Validation regions	80
7	Results	85
8	Conclusion	90
A	List of MC samples	91
A.1	List of data samples	91
A.2	List of background MC samples	91
A.3	List of signal MC samples	96
References		99

List of Figures

1.1	The table for all fundamental particles in SM. [1]	2
1.2	All allowed fundamental Feynman vertices in SM, except higgs-related vertices. [2]	4
1.3	All allowed fundamental higgs-related Feynman vertices in SM.	5
1.4	The particles in Standard Model and their corresponding super-partners and their names	7
1.5	The exclusion contours for the masses $m_{\tilde{\chi}_1^\pm, \tilde{\chi}_2^0}$ and $m_{\tilde{\chi}_1^0}$ in the Run-I analysis [4].	9
1.6	The Feynman diagram for the Wh same-sign signal scenario in this thesis. The final states in this process are two same-sign leptons (electron or muon), quarks (i.e. jets) and missing transverse momentum contributed by the lightest neutralinos $\tilde{\chi}_1^0$ and neutrinos ν .	10
2.1	The schematic diagram of the CERN accelerator complex, which shows a series of accelerators and facilities. [7]	13
2.2	The cut-away view of the ATLAS detector. It is 25 m high and 44 m long. [12]	15
2.3	The cross section of the ATLAS detector. This shows different components of the ATLAS and how ATLAS detect different types of particles [13]	15
2.4	This figure shows how the impact parameters z_0 and d_0 are defined by the nearest point (the small circle) of the track to the z-axis. It also shows how the azimuthal angle ϕ and the polar angle θ of the momentum \mathbf{p} are defined. p_T is the projection of the momentum \mathbf{p} onto the x-y plane.	17

2.5	The red lines show different directions corresponding to different positive values of pseudorapidity. [14]	18
2.6	Schematic view of the magnetic system of the ATLAS detector. [15]	19
2.7	The whole structure of the ATLAS inner detector. [16]	20
2.8	The distances R from the beam for the 3 components: pixel, SCT and TRT. [16]	21
2.9	The shapes, the orientations and the η coverage for each sensor. [11]	22
2.10	Schematic view for the calorimeter system of the ATLAS detector. [17]	25
2.11	Schematic view for one side of the end-cap and forward calorimeter. [18]	25
2.12	Schematic view for one side of the end-cap and forward calorimeter. One layer of forward calorimeter is electromagnetic and two are hadronic. [11]	26
2.13	The granularity in η and ϕ of the cells of each of the three layers in the electromagnetic calorimeter. [11]	27
2.14	Schematic view of one module of the tile calorimeter. [11]	29
2.15	Schematic view of the arrangement of the HEC readout structure in the 8.5 mm inter-plate gap. All dimensions are in mm. [11]	30
2.16	Electrode structure of FCal 1 with the matrix of copper plates and the copper tubes and rods with the LAr gap for the electrodes. The Molière radius, R_M , is represented by the solid disk. [11]	31
2.17	Cut-away view of the muon spectrometer. [19]	33
2.18	The cross section of the barrel region for the muon spectrometer. Three concentric cylindrical layers of barrel MDT are shown. [11]	34
2.19	The cross section of the end-cap region for the muon spectrometer. Four layers of end-cap MDT are shown in blue colour. Three layers of barrel MDT are also shown in green colour. [11]	35
2.20	The cross-section of a MDT tube. When the muon passes through the tube, free electrons are produced along the track. The free electrons are drifted to the anode wire. [11]	35

4.1	Distribution of the kinematic variables used for the optimization in SRjet1. The pre-selection, except the b-jet veto, has been applied. Only the statistical uncertainty is considered in the significance calculation.	48
4.2	Distribution of the kinematic variables used for the optimization in SRjet23. The pre-selection, except the b-jet veto, has been applied. Only the statistical uncertainty is considered in the significance calculation.	49
4.3	The N-1 plots for SRjet1. Only statistical uncertainties are considered in the significance calculation in the lower plot.	52
4.4	The N-1 plots for SRjet23. Only statistical uncertainties are considered in the significance calculation in the lower plot.	53
4.5	The expected combined signal significances for different mass points.	54
5.1	This shows how the track of the electron is incorrectly reconstructed (the orange track), due to the process of bremsstrahlung and γ conversion.	56
5.2	This shows how the track of the electron is incorrectly reconstructed (the orange track), due to very high p_T of the electron.	56
5.3	The measured values of the charge-flip rate ϵ_i in data. Only uncertainties due to the likelihood method are included.	60
5.4	The systematic variations of the charge-flip rate ϵ_i in data, due to the background subtraction.	62
5.5	This diagram shows how the original electron is found through the decay chain.	62
5.6	The comparison between the likelihood method and the MC truth method, by using the $Z \rightarrow ee$ MC samples. Hence, the systematic uncertainties due to likelihood method can be estimated.	64
5.7	The measured values of the charge-flip rate ϵ_i in data, with total uncertainties.	65
5.8	The comparison between the weighted OS events and the SS events, with different variables.	66
5.9	The real efficiencies for electrons (left) and muons (right). Only statistical uncertainties are considered.	72

5.10	The fake efficiencies for electrons (left) and muons (right). Only statistical uncertainties are considered.	74
5.11	Signal contributions in the validation region are shown for different mass points.	76
5.12	Distribution of the leading lepton p_T , m_{eff} , m_T , E_T^{miss} and n_{jets} in the electron-electron channel. The ratio of data to background is shown in the lower plot. The error bar includes all the systematic uncertainties except for the theoretical uncertainties.	77
5.13	Distribution of the leading lepton p_T , m_{eff} , m_T , E_T^{miss} and n_{jets} in the muon-muon channel. The ratio of data to background is shown in the lower plot. The error bar includes all the systematic uncertainties except for the theoretical uncertainties.	78
5.14	Distribution of the leading lepton p_T , m_{eff} , m_T , E_T^{miss} and n_{jets} in the electron-muon channel. The ratio of data to background is shown in the lower plot. The error bar includes all the systematic uncertainties except for the theoretical uncertainties.	79
6.1	Percentages of signal contribution are shown for the VRjet1 (left) and VRjet23 (right).	81
6.2	Background composition for the VRjet1 (left) and SRjet1 (right). . .	82
6.3	Background composition for the VRjet23 (left) and SRjet23 (right). .	82
6.4	Distributions of some variables in the VRjet1 for the background estimation and the data are shown. A signal of a mass point $(m_{\tilde{\chi}_1^\pm, \tilde{\chi}_2^0}, m_{\tilde{\chi}_1^0}) = (175, 0)$ is also shown. The internal shaded area refers to the statistical uncertainties, while the external shaded area refers to the total uncertainty.	83
6.5	Distributions of some variables in the VRjet23 for the background estimation and the data are shown. A signal of a mass point $(m_{\tilde{\chi}_1^\pm, \tilde{\chi}_2^0}, m_{\tilde{\chi}_1^0}) = (175, 0)$ is also shown. The internal shaded area refers to the statistical uncertainties, while the external shaded area refers to the total uncertainty.	84

7.1 N-1 plots for different variable distributions in the SRjet1 for the background estimation and the data. The signal of the mass point with the highest significance ($m_{\tilde{\chi}_1^\pm, \tilde{\chi}_2^0}, m_{\tilde{\chi}_1^0} = (175,0)$) is shown by the red dashed line. The internal shaded area refers to the statistical uncertainties, while the external shaded area refers to the total uncertainty. The vertical dashed line shows the SR cut of that variable. The lower plot shows the ratio of data with respect to the total background.	86
7.2 N-1 plots for different variable distributions in the SRjet23 for the background estimation and the data. The signal of the mass point with the highest significance ($m_{\tilde{\chi}_1^\pm, \tilde{\chi}_2^0}, m_{\tilde{\chi}_1^0} = (175,0)$) is shown by the red dashed line. The internal shaded area refers to the statistical uncertainties, while the external shaded area refers to the total uncertainty. The lower plot shows the ratio of data with respect to the total background.	87
7.3 The expected and observed exclusion limits for the combined SRjet1 and SRjet23 are shown. Experimental and theoretical systematic uncertainties are applied to background and signal samples and illustrated by the yellow band and the red dotted contour lines respectively. The red dotted lines indicate the $\pm 1\sigma$ variation on the observed exclusion limit due to theoretical uncertainties on the signal cross-section.	89

List of Tables

1.1	The spin and R-parity for the Standard Model particles and their superpartners.	8
2.1	The granularity in η and ϕ for different layers in the barrel region. [11]	27
2.2	The granularity in η and ϕ for different layers in the end-cap region. [11]	28
2.3	The granularity in the x-y plane in the forward calorimeter. [11]	32
3.1	List of the single lepton triggers used in this analysis.	39
3.2	List of the di-lepton triggers used in this analysis.	40
3.3	Summary of the electron and muon selection criteria. The signal selection requirements are applied on top of the baseline criteria.	41
3.4	Summary of the jet selection criteria.	42
4.1	Kinematic variables used in the optimization.	50
4.2	Final SR definitions	51
4.3	The background yields in the two signal regions. The unweighted event are also shown in parentheses.	51
5.1	Binning in p_T and $ \eta $ for the charge-flip rate ϵ_i	57
5.2	Binning in p_T and $ \eta $ for real efficiencies.	72
5.3	Binning in p_T and $ \eta $ for fake efficiencies.	74
5.4	Percentages of different backgrounds in the Validation region. The numbers in brackets are the yields.	76
6.1	The definition of the two validation regions, on top of the pre-selections in section 4.2.1. The values in red colour represent the changes with respect to the cuts in the signal regions.	80

6.2	The expected number of background events and the observed number of data events for the VRjet1 (the second column) and VRjet23 (the third column). The uncertainties includes the statistical and systematic uncertainties.	82
7.1	The observed events and the background yields in the signal regions are shown. The uncertainties include the statistical and systematic uncertainties.	85
7.2	From left to right: 95% confidence level upper limits on the visible cross section ($\langle \sigma_{\text{vis}} \rangle_{\text{obs}}^{95}$) and on the observed number of signal events (S_{obs}^{95}). The third column (S_{exp}^{95}) shows the 95% confidence level upper limit on the expected number of signal events, with $\pm 1\sigma$ excursions on the expectation of the background events. The last column shows the discovery p -value (p_0).	88
A.1	List of simulated W+jets processes	92
A.2	List of simulated Z+jets processes	93
A.3	List of simulated single-top processes	93
A.4	List of the simulated $t\bar{t}$ sample	93
A.5	List of simulated $t\bar{t}$ plus vector boson processes	93
A.6	List of simulated Higgs related processes, including Higgs plus vector boson production and $t\bar{t}H$ processes	94
A.7	List of simulated diboson processes	94
A.8	List of simulated triboson processes	94
A.9	List of simulated DrellYan processes	94
A.10	List of simulated multi-top processes	94
A.11	List of simulated V+ γ processes	95
A.12	List of signal samples	97

List of Abbreviations and Symbols

LHC Large Hadron Collider

SUSY Supersymmetry

Chapter 1

Theoretical Background

1.1 Introduction

Particle physics is a branch of physics that studies the most fundamental particles and their interaction. We believe that all matter and radiation in the universe are made up of these fundamental particles, and their behaviour is described by the theories in particle physics. In 20th century, our understanding about the nature of fundamental particles has had great breakthrough and advance. Also, many particle colliders have been built to give much insight to develop the theories and test the theories. The currently mainstream theory of particle physics is called the Standard Model.

1.2 Standard Model

Standard Model(SM) is the current theory to describe the fundamental particles in particle physics. It has already gained huge success in predicting the experimental results, including the prediction of existence of the top quark, the tau neutrino, and the Higgs boson. It has also explained almost all experimental results with high accuracy. It represents our best understanding of how the fundamental particles interact with each other.

Physicists discovered that there are 4 fundamental forces in the universe: electromagnetic force, weak force, strong force, and gravitational force. However, SM can only describe 3 of them: electromagnetic, weak and strong interaction, and the gravity cannot be described by SM. Figure 1.1 shows all fundamental particles in SM, and their mass, electric charge and spin. All matter is made up of

Standard Model of Elementary Particles

three generations of matter (fermions)						
	I	II	III			
QUARKS	mass 2/3 1/2	$\approx 2.4 \text{ MeV}/c^2$ u up	$\approx 1.275 \text{ GeV}/c^2$ c charm	$\approx 172.44 \text{ GeV}/c^2$ t top	0 0 1	gluon
	$\approx 4.8 \text{ MeV}/c^2$ -1/3 1/2	d down	$\approx 95 \text{ MeV}/c^2$ s strange	$\approx 4.18 \text{ GeV}/c^2$ b bottom	0 0 1	Higgs
	$\approx 0.511 \text{ MeV}/c^2$ -1 1/2	e electron	$\approx 105.67 \text{ MeV}/c^2$ μ muon	$\approx 1.7768 \text{ GeV}/c^2$ τ tau	0 1	photon
	$< 2.2 \text{ eV}/c^2$ 0 1/2	ν_e electron neutrino	$< 1.7 \text{ MeV}/c^2$ 0 1/2	$< 15.5 \text{ MeV}/c^2$ ν_μ muon neutrino	0 1/2	Z boson
						W boson
SCALAR BOSONS						
GAUGE BOSONS						

Figure 1.1: The table for all fundamental particles in SM. [1]

fermions (purple and green), which is the first 3 columns in figure 1.1. Fermions are divided into two groups: quarks(purple) and leptons(green). The forces between the fermions are mediated by the force carriers, which is gauge bosons(red). Higgs bosons(yellow) is scalar bosons, which give mass to other massive particles.

1.2.1 Matter particles

There are 6 types of quarks: up quarks(u), down quarks(d), charm quarks(c), strange quarks(s), top quarks(t) and bottom quarks(b). Quarks interact with strong interaction, while leptons does not. There are 3 types of charged leptons: electrons, muons and taus. There are 3 types of neutral leptons: electron neutrinos, muon neutrinos and tau neutrinos. The first column is the first generation, which is the lightest and most stable particles. Hence, normal matter in our daily life is made from the particles in the first generation. The second and third col-

umn are the second and third generation respectively, which is heavier and less stable particles. These particles will finally decay into the particles in the first generation. Due to the phenomenon of neutrino oscillation, neutrinos should have non-zero masses, but their value are still uncertain in our current technology.

1.2.2 Forces and carrier particles

Photon is the force carrier for electromagnetic interaction. Gluon is the force carrier for strong interaction. Z and W bosons are the force carriers for weak interaction. The effects of these fundamental forces stem from the exchange of the corresponding force carrier. These forces also have different strengths and different ranges. Strong force is the strongest force, while the electromagnetic force is in the middle. The weak force is the weakest force among the three, but it still much much stronger than the gravity. The electromagnetic force has infinite range, while the strong and weak forces have very short ranges at the level of subatomic particles.

For example, a proton is composed of two up quarks and one down quark, and a neutron is composed of one up quark and two down quarks. The forces between quarks inside the proton are mediated by gluons.

1.2.3 Feynman diagram

The fundamental interactions among these fundamental particles are described by the allowed fundamental Feynman vertices. All allowed fundamental Feynman vertices in SM are shown in figures 1.2 and 1.3. These fundamental vertices are the basic building blocks for all physical processes, by jointing these vertices together.

1.3 Limitation of Standard Model

Although Standard Model can explain almost all experimental results, there still are some phenomena it cannot explain.

1.3.1 Dark matter

Dark matter is some unknown matter that does not involve in electromagnetic interaction, but involve in gravitational interaction. It was first discovered in the Milky Way, by studying the speed of the stars orbiting around the center of the

Standard Model Interactions (Forces Mediated by Gauge Bosons)

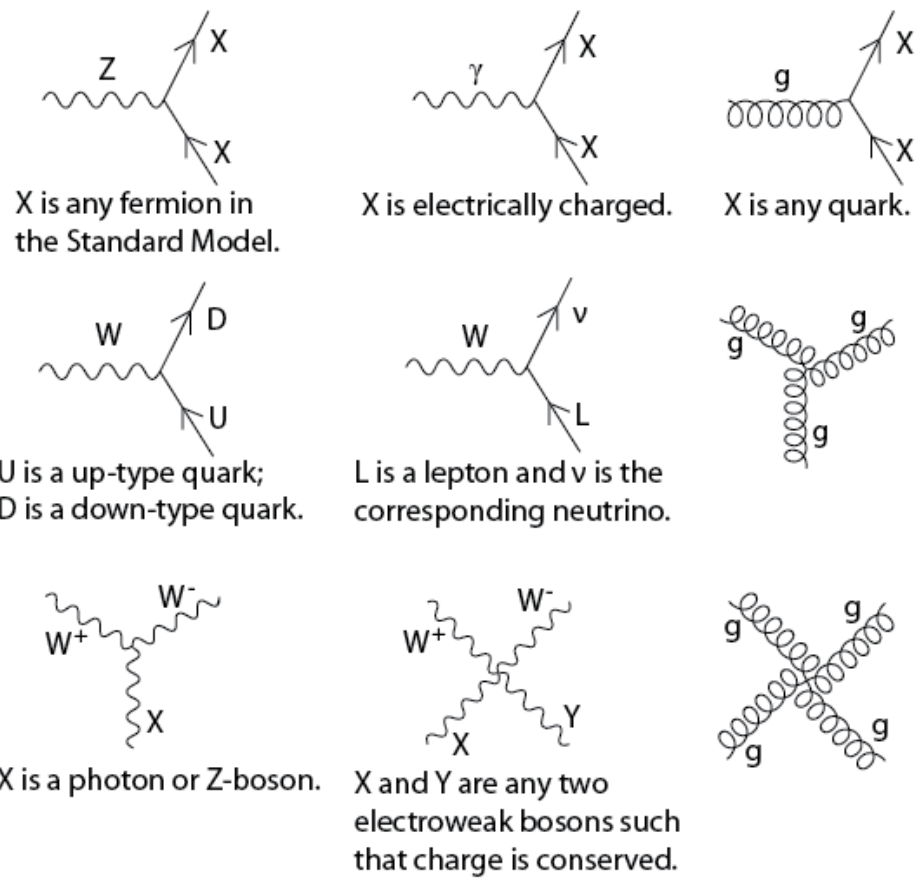


Figure 1.2: All allowed fundamental Feynman vertices in SM, except higgs-related vertices. [2]

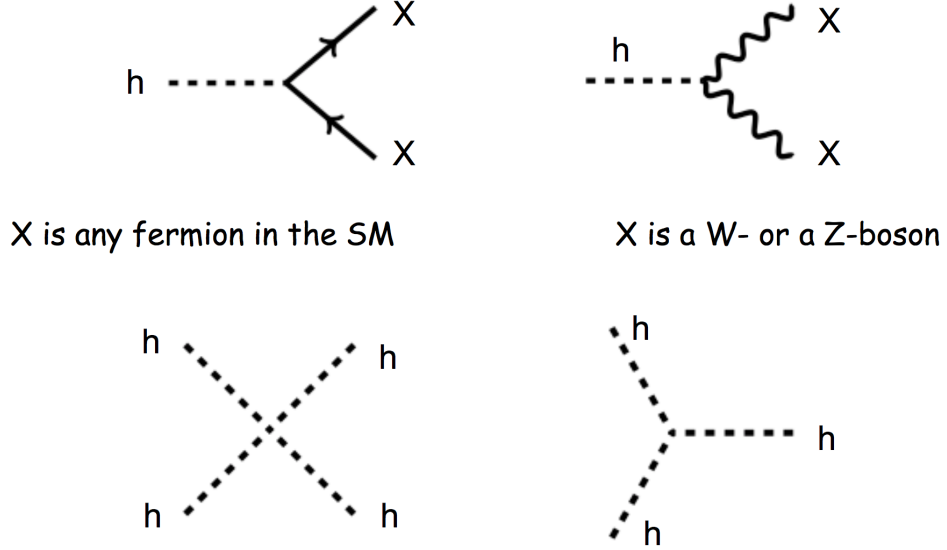


Figure 1.3: All allowed fundamental higgs-related Feynman vertices in SM.

Milky Way. Because it does not involve in electromagnetic interaction, it does not emit any electromagnetic radiation, and it cannot be seen by our telescopes. However, SM cannot explain the nature of dark matter, and what dark matter is made of.

1.3.2 Hierarchy problem

The hierarchy problem is the question why the weak force is stronger than the gravitational force by 10^{24} times. It is also asked why the mass of Higgs boson (~ 125 GeV) is much lighter than the Planck mass ($\sim 10^{19}$ GeV).

The Lagrangian for the interaction term between the fermion Dirac field ψ and the Higgs field h (i.e. Yukawa interaction) is given by

$$\mathcal{L}_{\text{Yukawa}} = -\lambda \bar{\psi} h \psi \quad (1.1)$$

where λ is the Yukawa coupling constant. The quantum correction to the square of the Higgs mass Δm_H^2 is then given by

$$\Delta m_H^2 = -\frac{|\lambda|^2}{16\pi^2} \Lambda^2 + \dots \quad (1.2)$$

where Λ is the energy scale up to which the Standard Model is valid, namely the Planck scale ($\sim 10^{19}$ GeV). Because Λ is quadratic divergent, the correction to the Higgs mass is in the order of Planck scale. Unless there are very delicate

cancellation between the correction terms, the Higgs mass should be in the order of Planck scale. But, we found that the experimental Higgs mass is in the order of 125 GeV, and this is called the hierarchy problem.

1.3.3 Unification of forces

In the 1860s, James Clerk Maxwell wrote down his famous equations Maxwell's equations, which unified two different phenomena: electricity and magnetism. Due to this unification, we now understand that electricity and magnetism are two different manifestations of the same phenomenon, and we now call it electromagnetism.

Similar thing happened in the 1970s, physicists developed a theory that unified two fundamental forces: electromagnetic force and weak force. At the energy scale above 246 GeV, these two forces will merge into a single force: electroweak force. This unification predicted the existence of weak neutral current and a force carrier to carry this weak force. This force carrier was later confirmed experimentally in CERN, and it is now called the Z boson.

After that, an effect of strong force was found experimentally that the strong force becomes weaker when the energy is higher. This may indicate that electroweak force and strong force will become a single force at even high energy. However, the energy scale at which these forces are the same is much larger than the energy the particle accelerators can reach. There are some theories beyond the Standard Model that try to unify these forces, such as supersymmetry.

1.4 Supersymmetry

Supersymmetry(SUSY) is an extension of the Standard Model, and try to answer some questions which the Standard Model cannot explain, mentioned in section 1.3. One of the problems SUSY can solve is the hierarchy problem of Higgs mass mentioned in section 1.3.2. We first notice that the negative sign in the equation 1.2 is due to the correction from the fermions. If we can somehow have a symmetry between the fermions and bosons, and add more positive correction terms due to the bosons, the correction terms will cancel with each other and the hierarchy problem can be solved. This new symmetry is called the supersymmetry (SUSY).

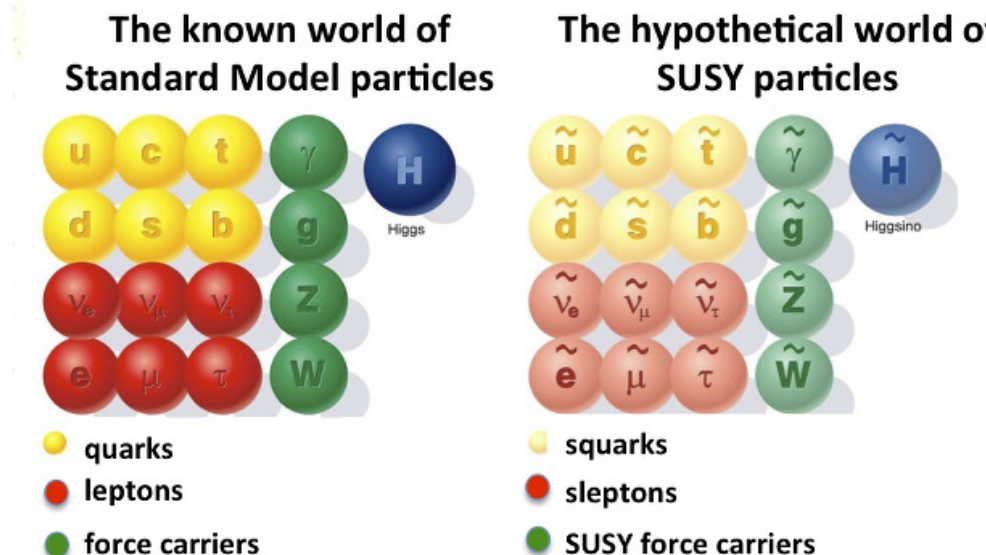


Figure 1.4: The particles in Standard Model and their corresponding superpartners and their names

1.4.1 Minimal Supersymmetric Standard Model

Minimal Supersymmetric Standard Model(MSSM) is the simplest realization of the supersymmetric theories that contain the minimum number of new particles and new interactions. It predicts that each particle in the Standard Model has its own partner particle, called the superpartner, as shown in figure 1.4. The name of the superpartner of a fermion is by adding a prefix “s”, followed by the name of the original Standard Model particle: squarks and sleptons, etc. For example, the superpartner of an electron is called selectron. For the superpartner of a Standard Model boson, the suffix “ino” is added: gluino and Higgsino, etc. As for the symbol for the superpartner, a tilde will be added above the original symbol. For example, the symbol for selectron is \tilde{e} . Also, the spin of the superpartner will differ from the Standard Model particle by 1/2. For fermions, the spin of their superpartner is 0, while for bosons, the spin of their superpartner is 1/2. The superpartners would interact with the same forces as the Standard Model particles, but they would have different masses. This is the new symmetry between the fermions and bosons, mentioned before. It is also the correction terms from these superpartners to fix the hierarchy problem of the Higgs mass.

In the MSSM, one neutral Higgs boson H and two charged Higgs bosons H^+ ,

H^- needed to be introduced. This means that for the Standard Model electro-weak bosons, there are 4 neutral bosons: γ , Z , h and H , and 4 charged bosons: W^+ , W^- , H^+ and H^- . The superpartners of the 4 neutral bosons together form 4 mass eigenstates, called neutralinos: $\tilde{\chi}_1^0$, $\tilde{\chi}_2^0$, $\tilde{\chi}_3^0$ and $\tilde{\chi}_4^0$. The superpartners of the 4 charged bosons together form two mass eigenstates with electric charge ± 1 , called charginos: $\tilde{\chi}_1^\pm$ and $\tilde{\chi}_2^\pm$. The subscripts of the symbol of the neutralinos and charginos are labeled by the ascending order in mass. Table 1.1 summarizes the Standard Model particles and their superpartners. If MSSM is correct, these supersymmetric particles should be detected in the LHC.

Type	SM particle	Symbol	Spin	R-parity	Superpartner	Symbol	Spin	R-parity
Fermions	Quark	q	$\frac{1}{2}$	+1	Squark	\tilde{q}	0	-1
	Lepton	l	$\frac{1}{2}$	+1	Slepton	\tilde{l}	0	-1
Gluon	Gluon	g	1	+1	Gluino	\tilde{g}	$\frac{1}{2}$	-1
Neutral EW Bosons	Photon	γ	1	+1	Neutralinos	$\tilde{\chi}_1^0, \tilde{\chi}_2^0, \tilde{\chi}_3^0, \tilde{\chi}_4^0$	$\frac{1}{2}$	-1
	Z Boson	Z	1	+1				
	Neutral Higgs	h, H	0	+1				
Charged EW Bosons	W Boson	W^+, W^-	1	+1	Charginos	$\tilde{\chi}_1^\pm, \tilde{\chi}_2^\pm$	$\frac{1}{2}$	-1
	Charged Higgs	H^+, H^-	0	+1				

Table 1.1: The spin and R-parity for the Standard Model particles and their superpartners.

The baryon number B is defined by $\frac{1}{3}(n_q - n_{\bar{q}})$, where n_q is the number of quarks and $n_{\bar{q}}$ is the number of anti-quarks. The lepton number L is defined by $n_l - n_{\bar{l}}$, where n_l is the number of leptons and $n_{\bar{l}}$ is the number of anti-leptons. In the Standard Model and the experimental data, $B - L$ is conserved, but in MSSM, it is no longer conserved. To keep this conservation and prevent the proton decay, the R-parity P_R is introduced.

$$P_R = (-1)^{3(B-L)-2s} \quad (1.3)$$

where s is the spin. By this definition, all Standard Model particles have R-parity +1, and all supersymmetric particles have R-parity -1. If the R-parity is conserved, the lightest supersymmetric particle (LSP) cannot decay and is stable. If the LSP is electrically neutral and interacts with matter only by the weak interaction and gravity, for example the lightest neutralinos $\tilde{\chi}_1^0$ or a sneutrino $\tilde{\nu}$, it could be a candidate for dark matter mentioned in section 1.3.1. In this thesis, the R-parity is assumed to be conserved, and the lightest neutralino $\tilde{\chi}_1^0$ is assumed to be the LSP. Due to the conservation of R-parity, the supersymmetric particles can only be pair-produced, and will eventually decay into Standard Model particles

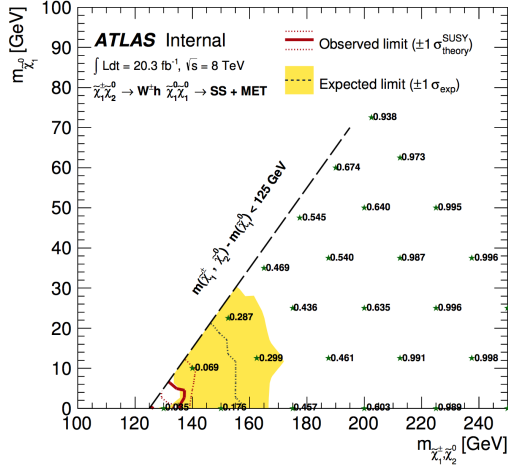


Figure 1.5: The exclusion contours for the masses $m_{\tilde{\chi}_1^\pm, \tilde{\chi}_2^0}$ and $m_{\tilde{\chi}_1^0}$ in the Run-I analysis [4].

and the lightest neutralino $\tilde{\chi}_1^0$, i.e. the LSP in this thesis.

1.5 Signal scenario

In the recent searches for the squarks and gluinos, the masses of gluinos and the first and second generation squarks are suggested to be larger than 1 TeV, while the masses of the third generation squarks are still allowed to be below 1 TeV [3]. In this case, the direct pair production of electroweak gauginos (i.e. neutralinos and charginos) may be the dominant SUSY production process at the LHC, if the masses of the gluinos and squarks are significantly heavier than the low mass electroweak gauginos, because the production cross sections of supersymmetric particles depend on the masses of the sparticles. With the results in the Run-I analysis [4] by using the center-of-mass energy $\sqrt{s} = 8 \text{ TeV}$ shown in figure 1.5, the electroweak pair production may be a promising hope for SUSY discovery at a higher center-of-mass energy $\sqrt{s} = 13 \text{ TeV}$ in Run-II using 2015 and 2016 data.

Same as the Run-I analysis, the supersymmetric process we are looking for is the pair production of the lightest chargino $\tilde{\chi}_1^\pm$ and the second lightest neutralino $\tilde{\chi}_2^0$. The masses of them are assumed to be the same, $m_{\tilde{\chi}_1^\pm} = m_{\tilde{\chi}_2^0}$, and denoted by $m_{\tilde{\chi}_1^\pm, \tilde{\chi}_2^0}$ in the later chapters. With the assumption that all sleptons are heavier than $\tilde{\chi}_1^\pm$ and $\tilde{\chi}_2^0$, $\tilde{\chi}_1^\pm$ will decay to W boson and $\tilde{\chi}_1^0$ (i.e. $\tilde{\chi}_1^\pm \rightarrow W^\pm + \tilde{\chi}_1^0$) and $\tilde{\chi}_2^0$ will decay to the lightest MSSM Higgs boson h and $\tilde{\chi}_1^0$ (i.e. $\tilde{\chi}_2^0 \rightarrow h + \tilde{\chi}_1^0$), or Z boson and $\tilde{\chi}_1^0$ (i.e. $\tilde{\chi}_2^0 \rightarrow Z + \tilde{\chi}_1^0$). In this thesis, we assume $\tilde{\chi}_1^\pm \rightarrow W^\pm + \tilde{\chi}_1^0$ and

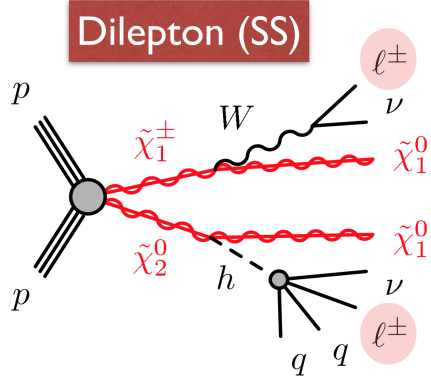


Figure 1.6: The Feynman diagram for the Wh same-sign signal scenario in this thesis. The final states in this process are two same-sign leptons (electron or muon), quarks (i.e. jets) and missing transverse momentum contributed by the lightest neutralinos $\tilde{\chi}_1^0$ and neutrinos ν .

$\tilde{\chi}_2^0 \rightarrow h + \tilde{\chi}_1^0$ decays with 100% branching ratio, which is the Wh channel we are looking for. The mass of the lightest MSSM Higgs boson h is set to 125 GeV.

The W boson from $\tilde{\chi}_1^\pm$ will decay into one lepton (electron or muon) and one neutrino (i.e. $W^\pm \rightarrow \ell^\pm + \nu$) with the SM branching ratio. The Higgs boson form $\tilde{\chi}_2^0$ will eventually decay into one lepton (electron or muon), quarks (i.e. jets) and neutrino(s) by various decay modes with the SM branching ratios. For example, $h \rightarrow W^+W^-$ and $h \rightarrow \tau^+\tau^-$ are the dominant decay modes, with one of the W/τ decays leptonically (e.g. $W^\pm \rightarrow \ell^\pm + \nu$) and another decays hadronically (e.g. $W \rightarrow q + q$). The Feynman diagram in figure 1.6 summarizes the whole signal scenario we are looking for in this thesis.

The two leptons in the final states are either electrons or muons, and the term “lepton” (with symbol ℓ) in the later chapters in this thesis refers to electron or muon, but not tau lepton or neutrino. We are only looking for two leptons with the same electric charge, in order to suppress the Standard Model backgrounds that have two leptons with opposite electric charge, mainly from Z boson decays. The mass splitting between the two lightest neutralinos ($m_{\tilde{\chi}_2^0} - m_{\tilde{\chi}_1^0}$) should be larger than the mass of Higgs boson (~ 125 GeV), in order to be able to pass the requirement of the signal lepton ($p_T > 25$ GeV), described in table 3.3. In the case that mass splitting is close to the mass of Higgs boson, which is called the compressed region, one of the lepton may not pass the requirement of the signal

lepton, due to the low momentum of the Higgs boson. However, if the Higgs boson eventually decays into two leptons, for example $h \rightarrow ZZ$ with one of the Z boson decays leptonically (e.g. $Z \rightarrow \ell^+ + \ell^-$) and another decays hadronically (e.g. $Z \rightarrow q + q$), the total number of leptons in the final state will be three. If one of the three leptons has low momentum and does not pass the signal requirement (i.e. not detected), and another two leptons have the same electric charge, this scenario will have the same final state as our signal. This means that in the compressed region, there are more decay modes for the Higgs boson, such that they have the same final state in our signal scenario, and hence this will contribute more sensitivity in the compressed region.

Because the two neutralinos $\tilde{\chi}_1^0$ and neutrinos ν in the final state cannot be detected, a large missing transverse momentum (i.e. unbalanced momentum in the detector) will be expected. This is also a signature for our signal.

This analysis is a collaborative work with other people and the results are mainly based on the paper [5] and the internal note [6].

Chapter 2

Experimental Setup

2.1 Introduction

Our experimental data was collected from the ATLAS particle detector in the Large Hadron Collider (LHC). The following section will introduce LHC and the ATLAS particle detector.

2.2 The Large Hadron Collider

The Large Hadron Collider (LHC) was built in the border between France and Switzerland by the European Organization for Nuclear Research (CERN). It is a circular particle collider under the ground with circumference 27 km. Two beams of protons will be accelerated in opposite directions, to almost the speed of light, and then these two beams will collide with each other at the collision point. The energy of each beam is 6.5 TeV, and hence the center-of-mass energy of the two beams \sqrt{s} is 13 TeV, which is the energy used in this experiment. This energy is equivalent to the speed that the beam will circulate the ring 11,245 times per second. Under this high energy, new physics phenomena will happen, including SUSY. Figure 2.1 shows the schematic diagram of the CERN accelerator complex, which contains a series of accelerators, from low energy to high energy. The dark blue big circle in figure 2.1 represents the LHC, on which there are 4 particle detectors at 4 different interaction points (yellow points): ATLAS, CMS, LHCb and ALICE. By analyzing these collisions, we can have a deeper understanding of the laws of nature.

Before the beam is injected into LHC, the protons need to be accelerated by a

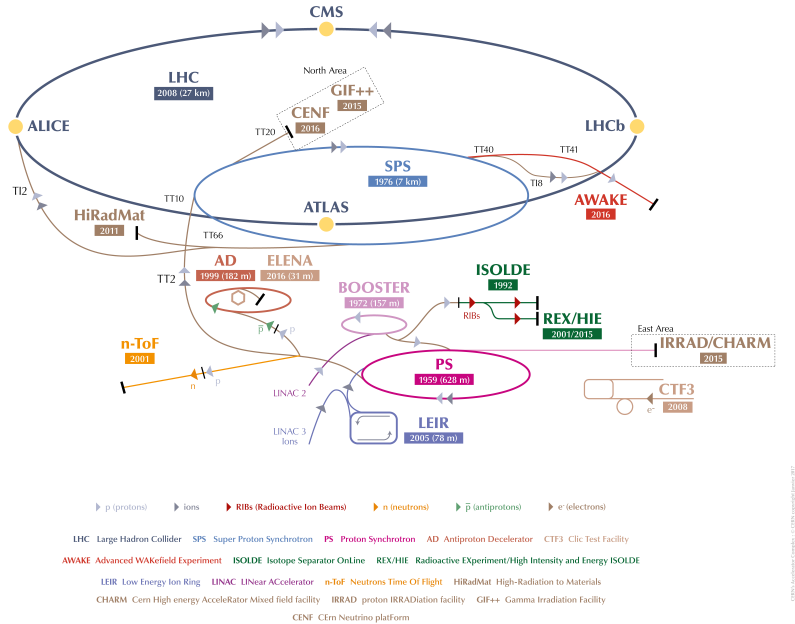


Figure 2.1: The schematic diagram of the CERN accelerator complex, which shows a series of accelerators and facilities. [7]

series of accelerators. The journey of the protons starts from a tank of hydrogen gas. The proton and the electron are separated by an electric field. The protons are then accelerated to 50 MeV by Linac2, which is a linear accelerator. The beam is then injected to the second accelerator called the Proton Synchrotron Booster (PSB), which accelerates the beam to 1.4 GeV. The beam is then injected to the third accelerator called the Proton Synchrotron (PS), which pushes the beam to 25 GeV. The beam is then injected to the fourth accelerator called the Super Proton Synchrotron (SPS), which further pushes the beam to 450 GeV. Finally, the beam is injected to the two beam pipes of the LHC. One of the beam moves in clockwise direction, while another beam moves in anti-clockwise direction. Two beams will be collided at the collision point inside the ATLAS detector. [8]

The circular path of the proton beam is maintained by many superconducting electromagnets along the LHC tunnel. There are 1232 main magnetic dipoles, and each of them generates a large magnetic field of 8.3 T. In order to generate such a high magnetic field, the coils need to have very high current of 11,080 A, and hence superconducting coil need to be used, to reduce the heat loss due to the electrical resistance. The material of superconducting coil is niobium-titanium

(NbTi). To reach the condition for superconductivity, the electromagnets operate at a very low temperature of 1.9 K. There are also 392 magnetic quadrupole to squeeze the proton beam, so that the chance of proton-proton collision will be higher. [9, 10]

The protons in the beam are grouped into different bunches, and there are about 10^{11} protons in each bunch. The time-spacing between two adjacent bunches is 25 ns (or 50 ns in the old configuration). This means that in each 25 ns, two bunches are collided at the collision point. For each bunch collision, there are about 10 to 50 proton-proton interaction. Hence, about 10^9 proton-proton collisions are produced in one second.

The interacting rate for a physics process $\frac{dN}{dt}$ is the product of the cross section of that physics process σ and the instantaneous luminosity \mathcal{L} .

$$\frac{dN}{dt} = \sigma \mathcal{L} \quad (2.1)$$

The instantaneous luminosity \mathcal{L} is a measure of the interacting rate of two protons at the collision point, which is related to the density of the protons and the speed of the protons. The instantaneous luminosity in this experiment is about 10^{34} $\text{cm}^{-2} \text{s}^{-1}$ (or $10 \text{ nb}^{-1} \text{s}^{-1}$).

2.3 ATLAS detector

A Toroidal LHC ApparatuS (ATLAS) is the particle detector used in this experiment [11]. Figure 2.2 shows the main components of the ATLAS detector. Its height is 25 m, its length is 44 m and its weight is 7000 tonne. The ATLAS detector is a general purpose particle detector, which is consisted of 3 main components: the inner detector, the calorimeter and the muon spectrometer. The heavy and hence short-lived particles will immediately decay into two or more lighter particles. The lighter particles and stable particles will pass through different parts of the detectors. These detectors mainly measure the momentum and energy of the particles. Figure 2.3 shows how the ATLAS distinguishes different types of particle, by using different components of the detector. The inner detector is surrounded by the solenoid, and with a strong magnetic field. The magnetic field will bend the track of the particle and the inner detector can detect the paths of the charged particles and its momentum. Photons and electrons will deposit most of their energy in the electromagnetic calorimeter, and finally stop by it.

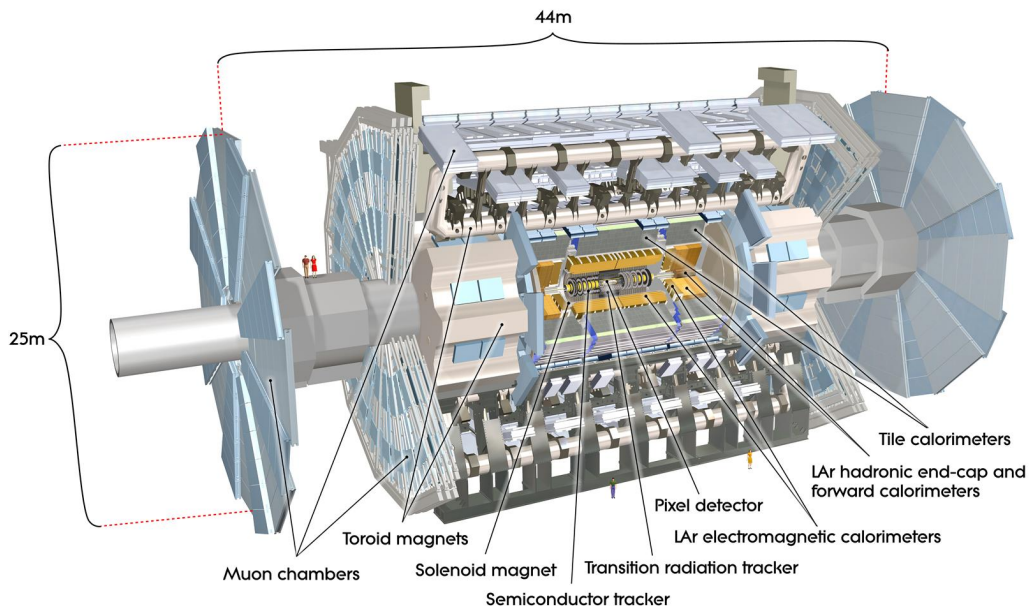


Figure 2.2: The cut-away view of the ATLAS detector. It is 25 m high and 44 m long. [12]

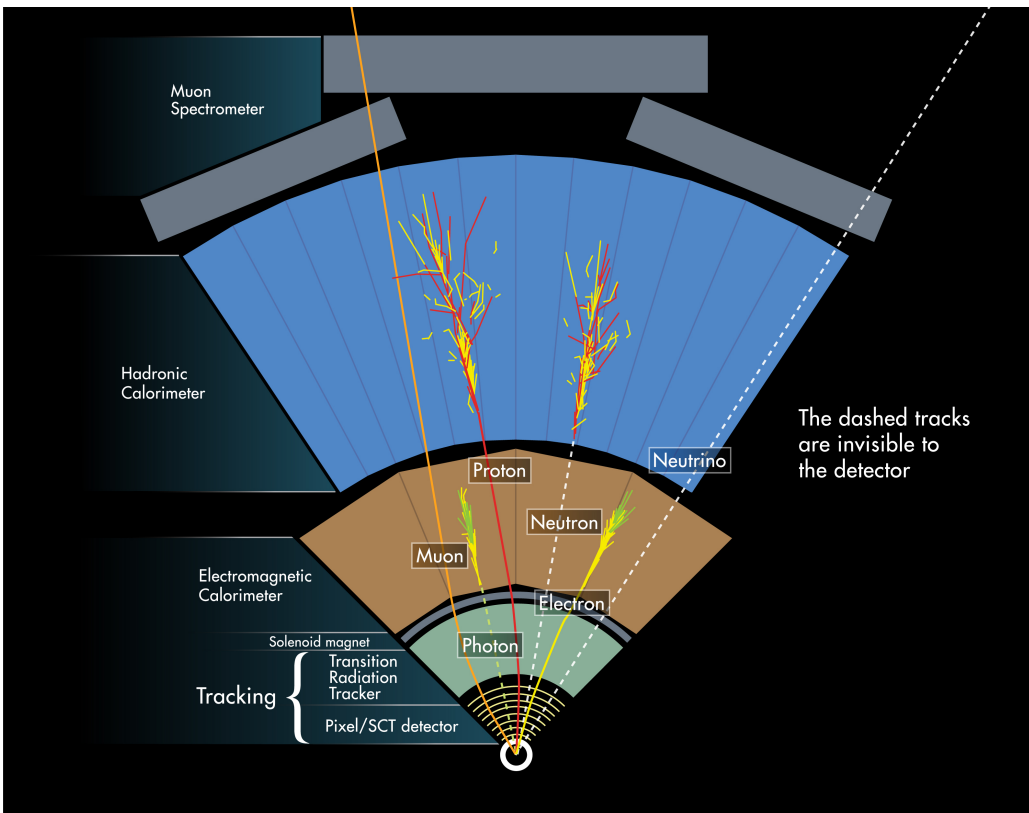


Figure 2.3: The cross section of the ATLAS detector. This shows different components of the ATLAS and how ATLAS detect different types of particles [13]

Hadrons(including protons and neutrons) and mesons will similarly stop by the hadronic calorimeter. Only muons and the neutrinos can reach the outermost muon spectrometer, but only muons can be detected by the muon spectrometer. Nearly all neutrinos will escape the whole ATLAS detector, which leads to some missing energy. In this design, different particles can be identified due to their own signature in different parts of ATLAS.

- **Electron** The track of an electron is measured by the inner detector, and its energy will be deposited in the electromagnetic calorimeter.
- **Proton** The track of a proton is measured by the inner detector, and its energy will be deposited in the hadronic calorimeter.
- **Photon** No track is inside inner detector, but its energy will be deposited in the electromagnetic calorimeter.
- **Neutron** No track is inside inner detector, but its energy will be deposited in the hadronic calorimeter.
- **Muon** The track of a muon is measured by the inner detector and the muon spectrometer. It will nearly not deposit its energy into the calorimeter and escape the detector.
- **Neutrino** Neutrino cannot be detected, and will escape the detector. It is only inferred by the missing momentum.

2.3.1 The coordinate system and basic variables

The nominal collision point is defined as the origin of the coordinate system. The z-axis is along the beam direction. The positive x-axis is pointing to the centre of the LHC ring. The positive y-axis is in the upward direction. The ATLAS detector has a reflection symmetry about the x-y plane.

The impact parameters of the track of a particle are z_0 and d_0 , described in figure 2.4. The nearest point of the track to the z-axis is marked by the small circle in the figure, with the smallest distance d_0 . The z-coordinate of the nearest point is z_0 .

The figure also shows the momentum \mathbf{p} of the particle when it passes through the nearest point. The azimuthal angle ϕ and the polar angle θ of the momentum

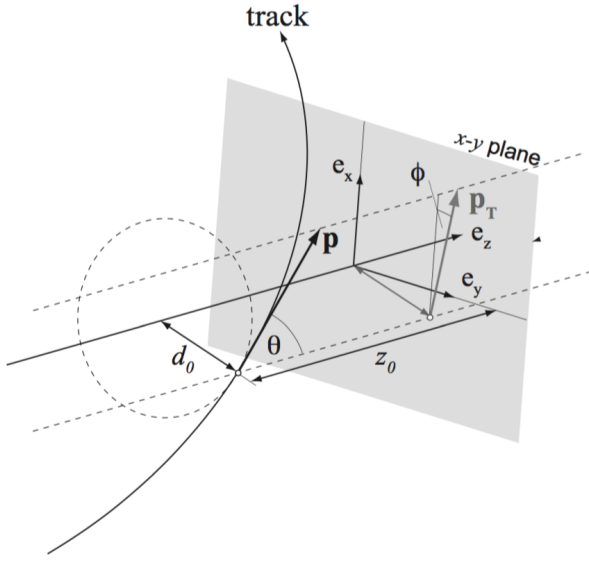


Figure 2.4: This figure shows how the impact parameters z_0 and d_0 are defined by the nearest point (the small circle) of the track to the z -axis. It also shows how the azimuthal angle ϕ and the polar angle θ of the momentum \mathbf{p} are defined. p_T is the projection of the momentum \mathbf{p} onto the x - y plane.

\mathbf{p} are defined as usual in the spherical coordinate system. The polar angle θ is the angle between the momentum \mathbf{p} and the positive z -direction. The pseudorapidity η is defined as:

$$\eta = -\ln \left(\tan \frac{\theta}{2} \right) \quad (2.2)$$

Different polar angles θ corresponding to different values of pseudorapidity η are shown in figure 2.5. The positive values of pseudorapidity η correspond to $0 < \theta < \frac{\pi}{2}$, while the negative values of pseudorapidity η correspond to $\frac{\pi}{2} < \theta < \pi$. The values of pseudorapidity η are reflective symmetric about the x - y plane.

$$(\eta \text{ at } \theta = \pi - x) = -\ln \left(\tan \frac{\pi - x}{2} \right) \quad (2.3)$$

$$= -\ln \left(\tan \left(\frac{\pi}{2} - \frac{x}{2} \right) \right) \quad (2.4)$$

$$= -\ln \left(\frac{1}{\tan \frac{x}{2}} \right) \quad (2.5)$$

$$= -\left(-\ln \left(\tan \frac{x}{2} \right) \right) \quad (2.6)$$

$$= -(\eta \text{ at } \theta = x) \quad (2.7)$$

The ATLAS detector covers the region where $|\eta| < 4.9$, but the reconstructed objects are often restricted to $|\eta| < 2.5$.

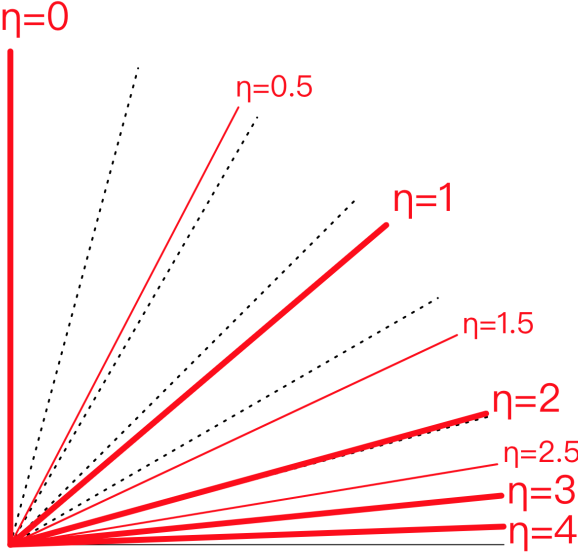


Figure 2.5: The red lines show different directions corresponding to different positive values of pseudorapidity. [14]

The projection of the nearest point onto the x-y plane is also shown in the figure 2.4. The transverse momentum of a particle, denoted by \mathbf{p}_T , is the projection of its momentum \mathbf{p} onto the x-y plane, as shown in the figure. The azimuthal angle ϕ of the momentum \mathbf{p} is the azimuthal angle of \mathbf{p}_T in the two-dimensional polar coordinate system on the x-y plane. The magnitude of \mathbf{p}_T is denoted by p_T .

$$p_T = \sqrt{p_x^2 + p_y^2} \quad (2.8)$$

In the later chapter, the term “transverse momentum” p_T refer to the magnitude of \mathbf{p}_T .

The distance ΔR in the pseudorapidity-azimuthal angle space of two particles is defined as:

$$\Delta R = \sqrt{(\Delta\phi)^2 + (\Delta\eta)^2} \quad (2.9)$$

It measures the angular separation of the momentum of two particles.

2.3.2 The magnetic system

There is a thin superconducting solenoid magnet around the inner detector, which generates a 2 T magnetic field in the z-direction inside the inner detector. There are also 3 large superconducting toroids around the calorimeter: one for barrel and two for end-caps. Each toroid consists of eight coils arranged symmetrically, which

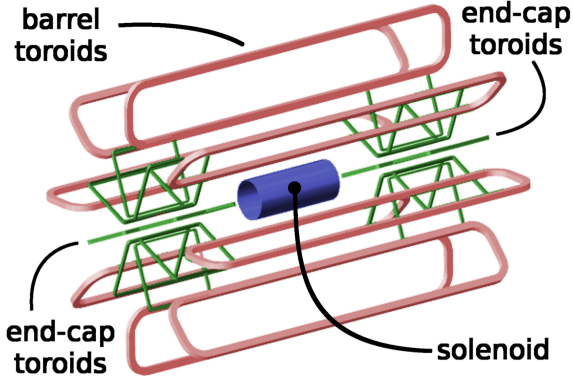


Figure 2.6: Schematic view of the magnetic system of the ATLAS detector. [15]

provide magnetic field in the ϕ -direction for the muon spectrometer. The end-cap toroids are rotated by 22.5° relative to the barrel toroid, in order to optimize the magnetic field at the region between the two coil systems. The strength of the magnetic field is 0.5 T in the barrel region and 1 T in the end-cap region. All these magnets are shown in figure 2.6.

2.3.3 The inner detector

The inner detector is a particle tracker. For each collision, about 1000 particles will be produced within $|\eta| < 2.5$. It mainly detects the tracks of charged particles and need to have good performance for measuring the momentum of the charged particles and locating the position of the vertices. Figure 2.7 shows the whole structure of the inner detector. The inner detector consists of 3 sub-detectors from inner to outer: the pixel detector, the silicon microstrip tracker (SCT) and the transition radiation tracker (TRT). Each part further divides into two parts: the barrel region with smaller $|\eta|$ and the end-cap region with larger $|\eta|$. Figure 2.8 shows the distances R from the beam for the 3 sub-detectors, and figure 2.9 shows the shapes and the orientations of each sensor and the η coverage, in both the barrel and the end-cap regions. The η coverage for the inner detector is $|\eta| < 2.5$. The shapes and the orientations of the sensors are different in the barrel and the end-cap regions. In the barrel region, the shape and the orientation of the sensors is concentric cylinder shells around the beam axis, while in the end-cap region, they are disks perpendicular to the beam axis.

The precision tracking detectors (pixels and SCT) has high resolution in space by using discrete space-points to detect the track of a charged particle, with

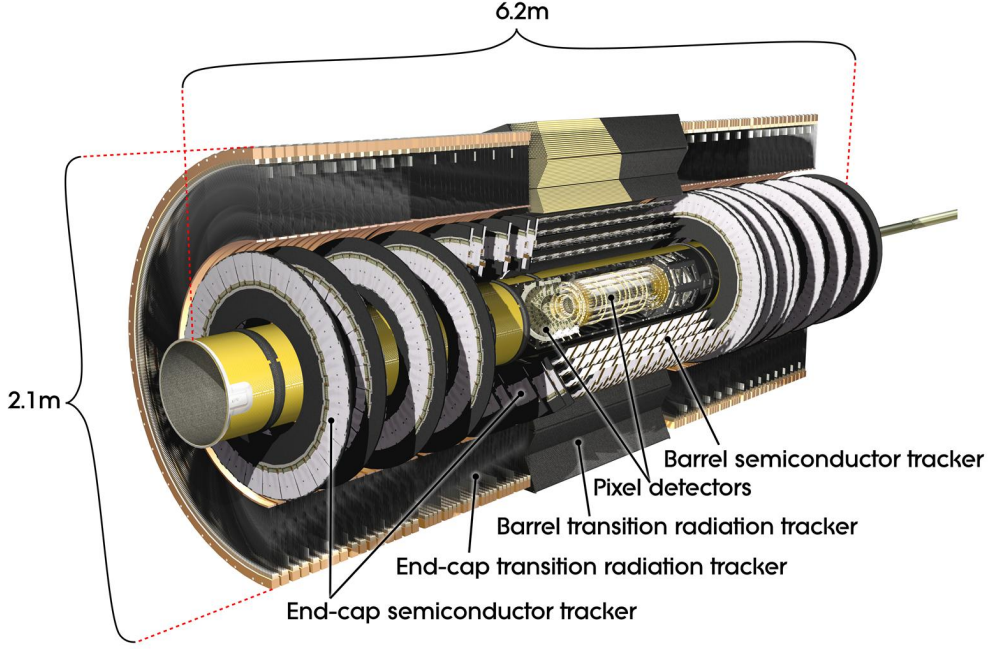


Figure 2.7: The whole structure of the ATLAS inner detector. [16]

the cutting-edge technology, in order to achieve the good performance of the inner detector. When the particle moves inside the inner detector, there are, in average, 36 hits per one track. By recording the positions of these hits, the path of the particle can be reconstructed. The whole inner detector is immersed in a 2 T magnetic field generated by the solenoid magnet, and hence the path of any charged particles will be bent. By measuring the curvature of the path, the charge and momentum of the particle can be measured. The equation for the circular path is

$$\frac{d\mathbf{p}}{dt} = q(\mathbf{v} \times \mathbf{B}) \quad (2.10)$$

where the relativistic momentum $\mathbf{p} = \gamma m \mathbf{v}$.

$$\frac{d\mathbf{p}}{dt} = q\left(\frac{\mathbf{p}}{\gamma m}\right) \times \mathbf{B} \quad (2.11)$$

$$= \frac{q}{\gamma m} (\mathbf{p} \times \mathbf{B}) \quad (2.12)$$

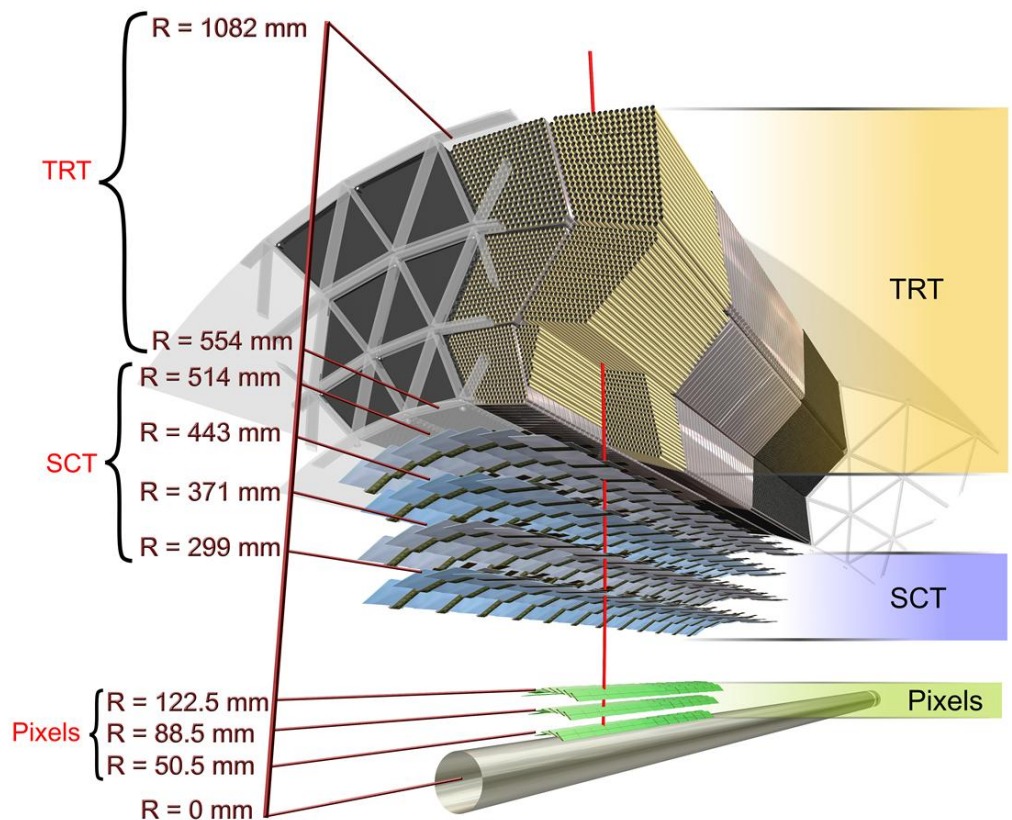


Figure 2.8: The distances R from the beam for the 3 components: pixel, SCT and TRT. [16]

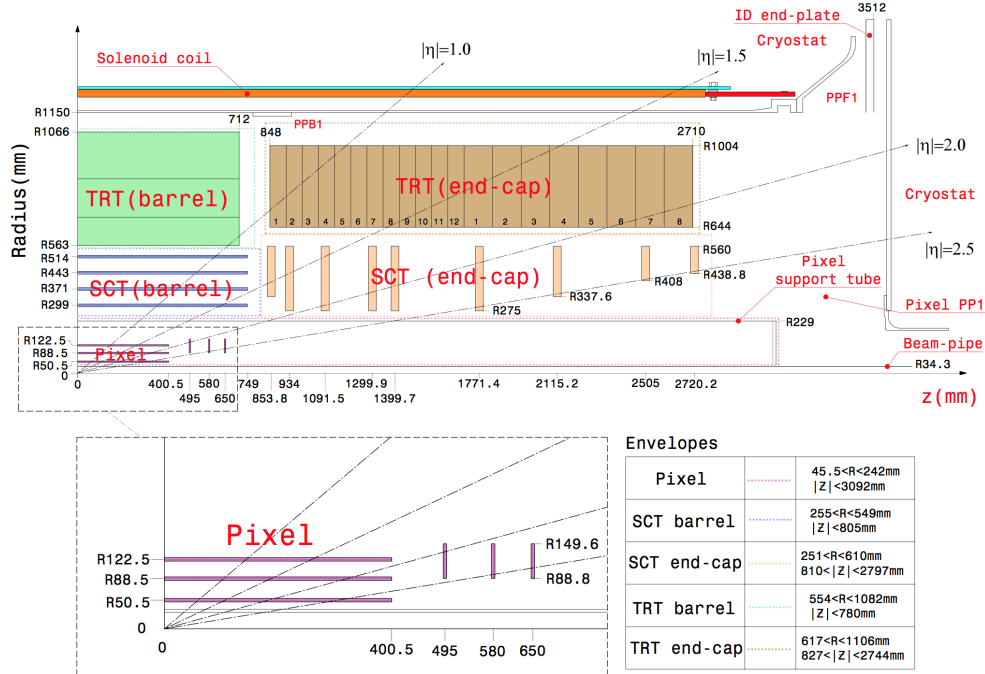


Figure 2.9: The shapes, the orientations and the η coverage for each sensor. [11]

From this equation, we can get the angular frequency ω ,

$$\omega = \frac{qB}{\gamma m} \quad (2.13)$$

$$\frac{v}{r} = \frac{qB}{\gamma m} \quad (2.14)$$

$$\frac{1}{r} = \frac{qB}{\gamma mv} \quad (2.15)$$

$$\frac{1}{r} = \frac{qB}{p} \quad (2.16)$$

$$p = rqB \quad (2.17)$$

By this equation, we can calculate the momentum of the particle, from the curvature of track $1/r$, the charge and the magnetic field strength.

2.3.3.1 Pixel detector

The pixel detector is the innermost part of the inner detector, and hence it needs to withstand the highest amount of radiation from the interaction point. As shown in figure 2.9, there are 3 layers of cylinder in the barrel region at radii 50.5 mm, 88.5 mm and 122.5 mm, and 3 layers of disk for each end-cap region at $z = 495$ mm, 580 mm and 650 mm. There are in total 1744 modules in the pixel detectors. Each module is identical, and has the size of $19\text{mm} \times 63\text{mm}$. The

module has 47232 pixels, which has size of $50\mu\text{m} \times 400\mu\text{m}$, and hence there are in total 80 million pixels for the whole pixel detector. Each pixel has the accuracy of $10\mu\text{m} \times 115\mu\text{m}$.

The sensor in the module is using planar n⁺-in-n type of silicon with $250\mu\text{m}$ thick, with n⁺-type at the readout side (i.e. the electronics chip) and n-type at another side. When the charged particle passes through the silicon, electrons are produced and attracted to the anode, which is attached to an electronics chip with $180\mu\text{m}$ thick.

The innermost layer of pixels at radius 50.5 mm is very important for measuring the secondary vertices of the long-lived b-hadrons. It helps identify the b-jets (jets originating from bottom quarks), which are the decay products of the top quarks and Higgs bosons.

2.3.3.2 SCT

The SCT is in the middle part of the inner detector. As shown in figure 2.9, there are 4 layers of cylinder in the barrel region, and 9 layers of disk for each end-cap region. There are in total 4088 modules in the SCT, and in total 6.3 million pixels. Each module has the thickness of $300\mu\text{m}$. It has a thermally conductive base-board in the middle, which provides the cooling of the sensor. The p-in-n silicon sensors are glued on each side of the base-board. The working principle is similar to the pixel detector. Each sensor has the spatial resolution of $17\mu\text{m} \times 580\mu\text{m}$.

2.3.3.3 TRT

The TRT is the outermost part of the inner detector. It continues detecting the track of the charged particle, and help distinguishing the electrons from other charged hadrons. It is a straw tube gaseous detector, with 96 TRT modules in the barrel and 20 TRT modules on each end-cap. There are in total 52544 straws in the barrel and 122880 straws in the end-cap. Each straw tube is a polyimide drift straw tube with 144 cm long and 4 mm diameter. It is filled with a non-flammable gas mixture of 70% Xe, 27% CO₂ and 3% O₂. When the charged particle passes through the gas, the charged particle ionizes the gas and produce transition radiation. The transition radiation further ionizes the gas and produce free electrons, which are attracted to the wire at the center of the straw tube. The electrons can be identified by detecting the amount of transition radiation,

because electrons will emit more transition radiation than other charged hadrons, like pions.

TRT has the spatial resolution of $130\mu\text{m}$ in the $\text{R}-\phi$ plane. The spatial resolution of z can only be provided by the length of the straw tube, 144 cm.

2.3.4 Calorimeter

The calorimeters measure the energy of the particle. Besides the measurement of the energy of the particles, it also helps identifying different particles, like electrons, photons and jets. It is because different particles will have different signature when the particle deposits its energy to the calorimeters. It contains two types of calorimeter: the electromagnetic calorimeter and the hadronic calorimeter. The electromagnetic calorimeter is designed to measure the energy of electrons and photon, while the hadronic calorimeter is for the hadrons, like protons, neutrons and mesons. The figure 2.10 shows the whole calorimeter system of the ATLAS detector. In the barrel region, the Liquid Argon (LAr) electromagnetic calorimeter (ECal) works as an electromagnetic calorimeter, while the tile calorimeter (TileCal) works as a hadronic calorimeter. In the end-cap region, the LAr ElectroMagnetic End-Cap (EMEC) calorimeter works as an electromagnetic calorimeter, while the LAr Hadronic End-Cap (HEC) calorimeter works as a hadronic calorimeter. In the forward region, the LAr Forward Calorimeter (FCal) has three layers: one is electromagnetic and two are hadronic. Figure 2.11 and 2.12 show the schematic view for one side of the end-cap and forward calorimeter. The large coverage $|\eta| < 4.9$ is to ensure a good measurement of the missing energy (E_T^{miss}).

2.3.4.1 Electromagnetic calorimeter

For the barrel region, it covers $|\eta| < 1.457$. For the end-cap region, there are two concentric wheels, with the outer one covering from $1.375 < |\eta| < 2.5$ and the inner one covering from $2.5 < |\eta| < 3.2$. The EM calorimeter is alternately interleaved with many accordion-shaped layers of electrodes and absorbers, and is filled with liquid argon between the layers at -185°C . The accordion geometry provides complete ϕ symmetry without azimuthal cracks. A layer of absorbers is made of a lead plate, to which two stainless-steel sheets (0.2 mm thick) are glued on both sides. The thickness of the lead plate is 1.53 mm for $|\eta| < 0.8$ and 1.13

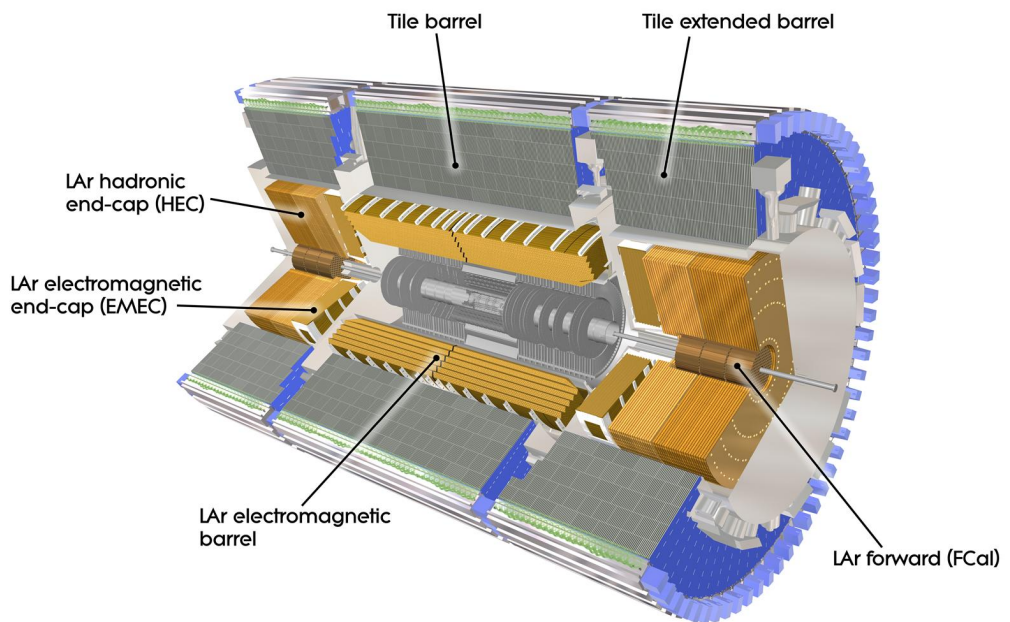


Figure 2.10: Schematic view for the calorimeter system of the ATLAS detector.

[17]

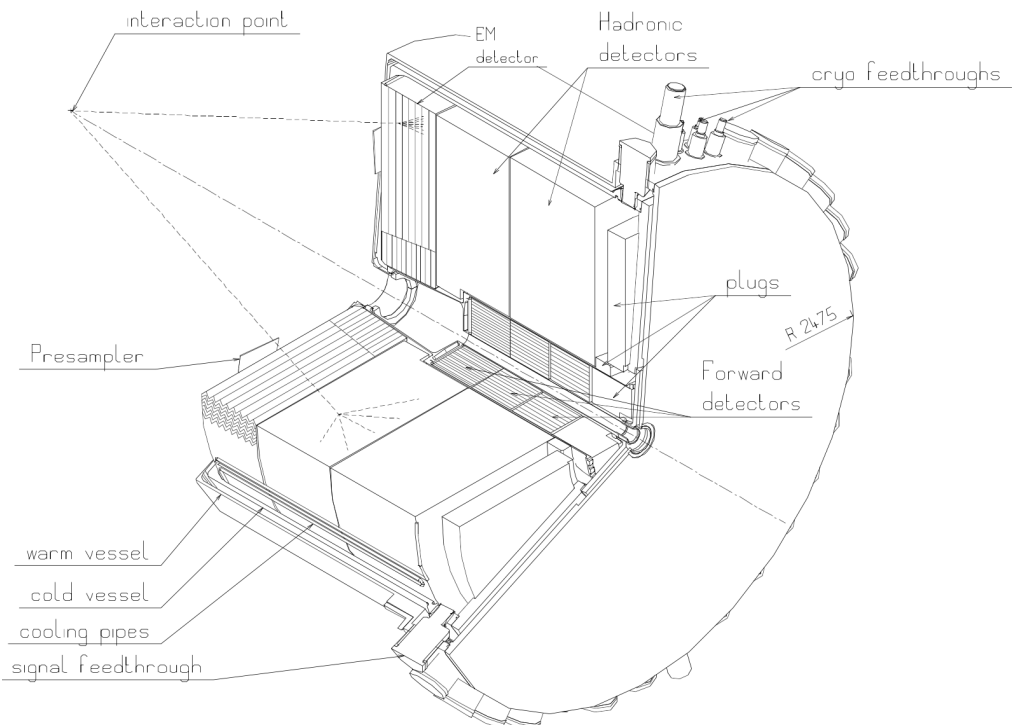


Figure 2.11: Schematic view for one side of the end-cap and forward calorimeter.

[18]

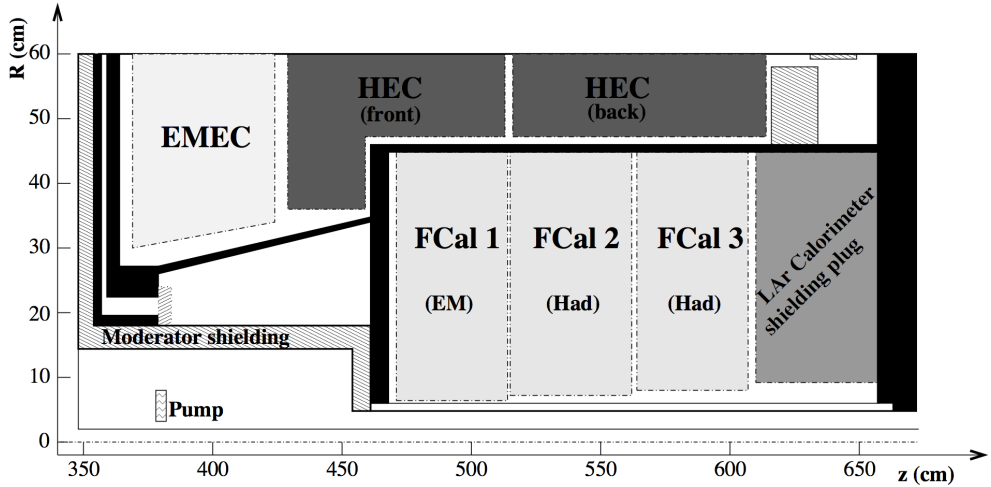


Figure 2.12: Schematic view for one side of the end-cap and forward calorimeter.

One layer of forward calorimeter is electromagnetic and two are hadronic. [11]

mm for $|\eta| > 0.8$ in the barrel region, and 1.7 mm for $|\eta| < 2.5$ and 2.2 mm for $|\eta| > 2.5$ in the end-cap region. A layer of electrode is made of three conductive copper layers, which are separated by insulating polyimide sheets. When the high energy electron or photon pass through the lead absorbers, a shower of lower energy electrons, positrons and photons is produced. The liquid argon atom, as the active material, is ionized by the particles in the shower, and free electrons are produced and attracted to the electrode. By measuring the current from the electrode, the energy of the electron or photon can be measured.

The lead absorber can also further reduce the energy of particles in the shower before they escape the calorimeter. Hence, only part of the energy is measured, and a correction need to be applied. The innermost layer, called the presampler, help calculate the correction due to the energy lost.

It has a fine granularity to have precise measurements for electrons and photons. The granularity depends on the layers, as shown in figure 2.13. Besides the layer of presampler, there are two or three layers (Layer 1, Layer 2 and Layer 3), depending the $|\eta|$. For the region used by the signal objects, i.e. $|\eta| < 2.5$, three layers are often used for precise measurement. Table 2.1 and 2.2 show the granularity for each layers in the barrel region and the end-cap region respectively.

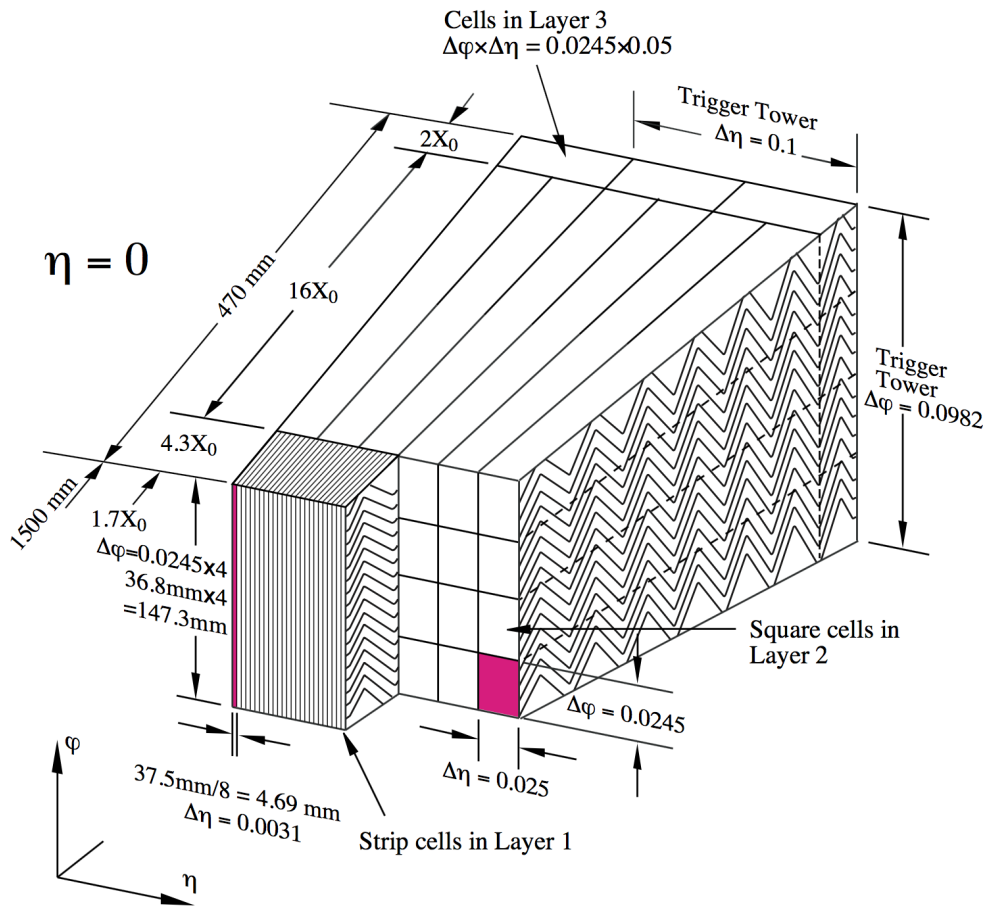


Figure 2.13: The granularity in η and ϕ of the cells of each of the three layers in the electromagnetic calorimeter. [11]

Layer	$ \eta $ range	Granularity $\Delta\eta \times \Delta\phi$
Presampler	$ \eta < 1.52$	0.025×0.1
Layer 1	$ \eta < 1.4$	0.003×0.1
	$1.4 < \eta < 1.475$	0.025×0.025
Layer 2	$ \eta < 1.4$	0.025×0.025
	$1.4 < \eta < 1.475$	0.075×0.025
Layer 3	$ \eta < 1.35$	0.050×0.025

Table 2.1: The granularity in η and ϕ for different layers in the barrel region. [11]

Layer	$ \eta $ range	Granularity $\Delta\eta \times \Delta\phi$
Presampler	$1.5 < \eta < 1.8$	0.025×0.1
Layer 1	$1.375 < \eta < 1.425$	0.050×0.1
	$1.425 < \eta < 1.5$	0.025×0.1
	$1.5 < \eta < 1.8$	0.003×0.1
	$1.8 < \eta < 2.0$	0.004×0.1
	$2.0 < \eta < 2.4$	0.006×0.1
	$2.4 < \eta < 2.5$	0.025×0.1
	$2.5 < \eta < 3.2$	0.1×0.1
Layer 2	$1.375 < \eta < 1.425$	0.050×0.025
	$1.425 < \eta < 2.5$	0.025×0.025
	$2.5 < \eta < 3.2$	0.1×0.1
Layer 3	$1.5 < \eta < 2.5$	0.050×0.025

Table 2.2: The granularity in η and ϕ for different layers in the end-cap region. [11]

2.3.4.2 Hadronic calorimeter

For the barrel region, tile calorimeter is used for measuring the energy of the hadrons in $|\eta| < 1.7$. The central barrel covers $|\eta| < 1.0$, while the extended region covers $0.8 < |\eta| < 1.7$. As shown in figure 2.14, the tile calorimeter is alternately interleaved with sheets of steel and scintillator, called tile, like a sandwich. The steel acts as the absorber material, while the scintillator acts as the active material. When the high energy hadron passes through the sheets of steel, it will have nuclear interaction with the atomic nuclei of the steel, and produce a shower of lower energy charged particles, which then trigger the scintillators to produce photons. These photons are collected by the wavelength-shifting fibres on the edges of the tile. The photomultiplier tubes (PMT) then convert the optical signal to the electronic signal. By measuring the intensity of the photons, the energy of the hadron can be measured. There are 3 layers in the tile calorimeter. The granularity of the first 2 layers is $\Delta\eta \times \Delta\phi = 0.1 \times 0.1$, while the third layer is $\Delta\eta \times \Delta\phi = 0.2 \times 0.1$.

For the end-cap region $1.5 < |\eta| < 3.2$, there are two independent wheels of LAr hadronic calorimeters (HEC) for each end-cap, i.e. the front wheel and the back wheel as shown in figure 2.12. For each wheel, it consists of 32 identical

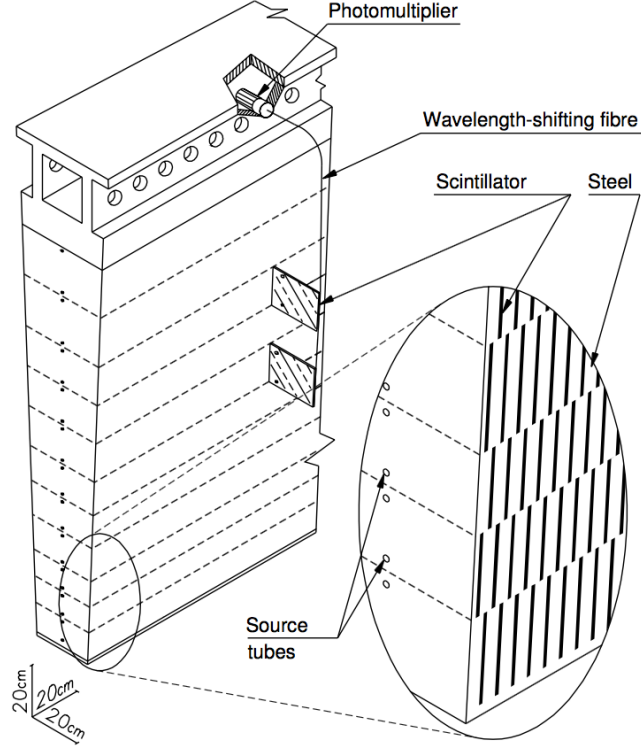


Figure 2.14: Schematic view of one module of the tile calorimeter. [11]

wedge-shaped modules and each module has two layers. Hence, in total, there are 4 layers for each end-cap. Similar to the electromagnetic calorimeter, it uses the liquid argon as the active material, but it uses flat parallel copper plates as the absorber material. For the front wheel, there are 24 copper plates with 25 mm thick. For the back wheel, there are 16 copper plates with 50 mm thick. The thickness of the gap between the copper plates is 8.5 mm. As shown in figure 2.15, the gap is separated by three electrodes and is filled with liquid argon. The granularity is $\Delta\eta \times \Delta\phi = 0.1 \times 0.1$ for $1.5 < |\eta| < 2.5$, and $\Delta\eta \times \Delta\phi = 0.2 \times 0.2$ for $2.5 < |\eta| < 3.2$.

2.3.4.3 Forward calorimeter

The LAr Forward calorimeter (FCal) covers $3.1 < \eta < 4.9$, with 3 wheels: FCal 1, FCal 2 and FCal 3. FCal 1 is an electromagnetic calorimeter and use copper as the absorber material. FCal 2 and FCal 3 are hadronic calorimeters and use tungsten as the absorber material. It uses the liquid argon as the active material.

Due to the high $|\eta|$ and the close distance to the interaction point (4.7 m),

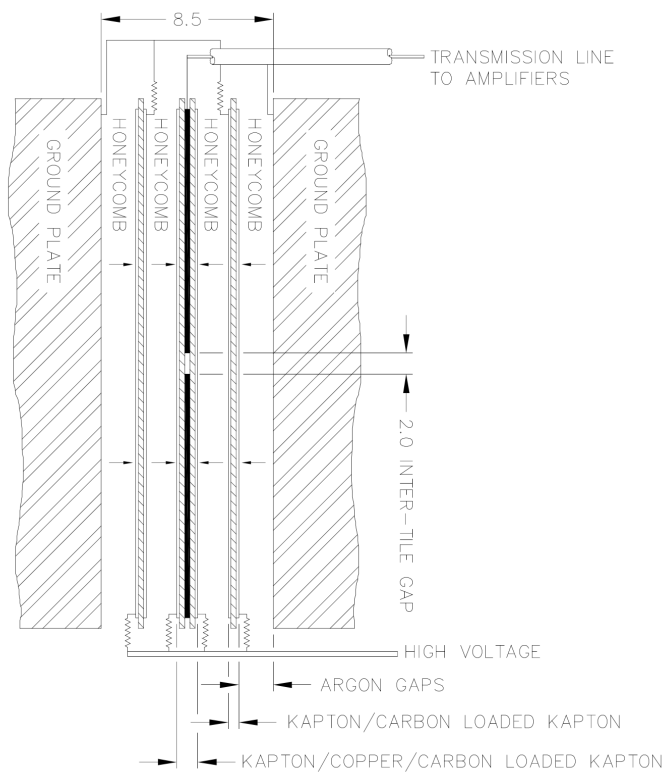


Figure 2.15: Schematic view of the arrangement of the HEC readout structure in the 8.5 mm inter-plate gap. All dimensions are in mm. [11]

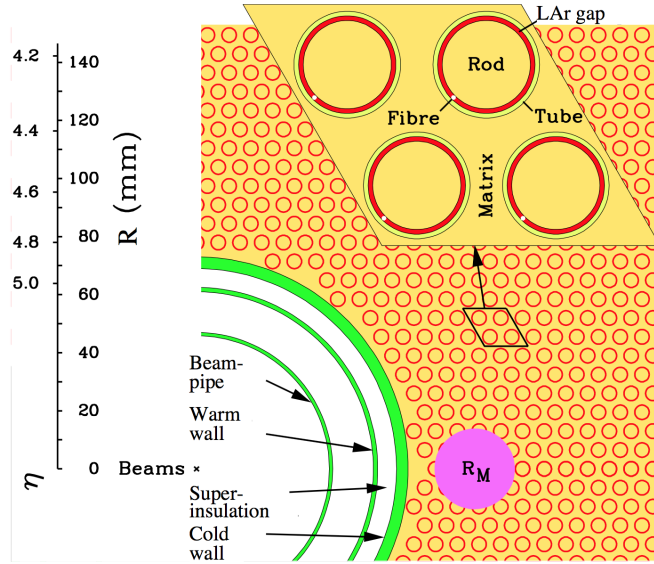


Figure 2.16: Electrode structure of FCal 1 with the matrix of copper plates and the copper tubes and rods with the LAr gap for the electrodes. The Molière radius, R_M , is represented by the solid disk. [11]

the forward calorimeters are exposed to high particle fluxes. This results in a new design with a small gap of liquid argon to avoid the ion build-up problems. Figure 2.16 shows the structure of FCal 1. A matrix of copper plates is filled inside the forward calorimeter, with 12260 regularly spaced electrodes parallel to the beam direction. In the electrodes, there are concentric copper rods and copper tubes. The gap between rod and tube is filled with a thin layer of liquid argon with thickness 0.269 mm.

For FCal 2 and FCal 3, there are 10200 and 8224 electrodes respectively. The structure is similar to FCal, but the copper rods are replaced by the tungsten rods, and the matrix of copper plates is replaced by a matrix of tungsten alloy. The tungsten rod is surrounded by a copper tube, with the gap filled with liquid argon. The thickness of the liquid argon of FCal 2 and FCal 3 are 0.376 mm and 0.508 mm respectively. The granularity of the forward calorimeter in the x-y plane is shown in 2.3.

A shielding plug made of a copper alloy has been mounted behind the FCal 3 to further reduce the backgrounds that reach the muon spectrometer.

Layer	$ \eta $ range	Granularity $\Delta x \times \Delta y$ (cm)
FCal 1	$3.15 < \eta < 4.30$	3.0×2.6
	$3.10 < \eta < 3.15$	\sim four times finer
	$4.30 < \eta < 4.83$	\sim four times finer
FCal 2	$3.24 < \eta < 4.50$	3.3×4.2
	$3.20 < \eta < 3.24$	\sim four times finer
	$4.50 < \eta < 4.81$	\sim four times finer
FCal 3	$3.32 < \eta < 4.60$	5.4×4.7
	$3.29 < \eta < 3.32$	\sim four times finer
	$4.60 < \eta < 4.75$	\sim four times finer

Table 2.3: The granularity in the x-y plane in the forward calorimeter. [11]

2.3.5 Muon Spectrometer

The muon spectrometer is a tracker for muons. In the barrel region ($|\eta| < 1.4$), the magnetic field is provided by the barrel toroid, described in section 2.3.2. In the end-cap region ($1.6 < |\eta| < 2.7$), the magnetic field is provided by the end-cap toroid. In the transition region ($1.4 < |\eta| < 1.6$), the magnetic field is provided by the combined field from the two toroids.

Figure 2.17 shows all the components in the muon spectrometer. The tracking detector is mainly provided by the Monitored Drift Tube chambers (MDT), in the range of $|\eta| < 2.7$. In the barrel region, the track of the muon is measured by three cylindrical layers of MDT, located at $R = 5$ m, 7.5 m and 10 m, as shown in figure 2.18. Each layer has 8 large chambers and 8 small chambers. In the end-cap and the transition region, there are four wheels of MDT, located at $|z| = 7.4$ m, 10.8 m, 14 m and 21.5 m, as shown in figure 2.19. For the naming scheme of MDT chambers, the first letter (B and E) refers to the barrel and end-cap chambers respectively. The second letter (I, E, M and O) refers to the inner, extra, middle and outer layers respectively. The third letter (L and S) refers to the large and small chambers respectively.

The total number of drift tubes in each MDT chamber is about 200 to 500, depending on the type of the chamber. The lengths of the drift tubes vary from 0.85 m to 6.24 m. The tube is made of aluminium with a diameter of 29.970 mm, as shown in figure 2.20. It is filled with a gas mixture of 93% argon and 7% CO₂,

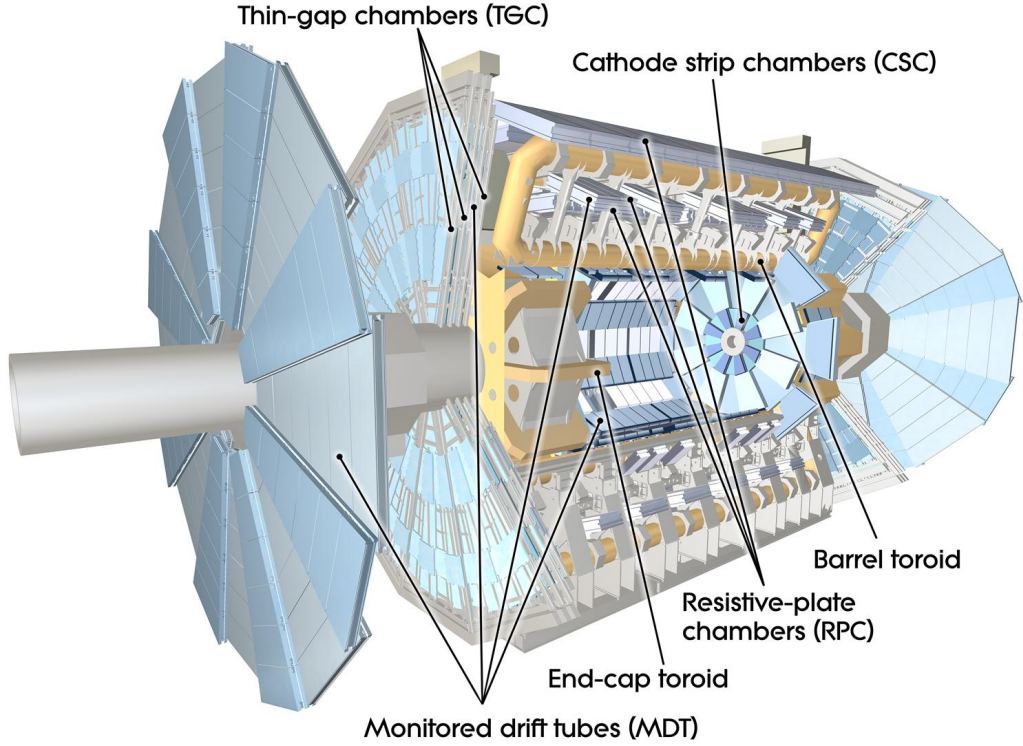


Figure 2.17: Cut-away view of the muon spectrometer. [19]

operated at a pressure of 3 bar. The anode wire is made of tungsten-rhenium with a diameter of $50 \mu\text{m}$, at a potential of 3080 V. When the muon passes through the tube, the gas mixture is ionized and free electrons are produced. The free electrons are attracted and drifted to the anode wire. By measuring the drift time the free electrons take from the position of the muon to the anode wire, the position of the muon can be measured. The average resolution of the MDT is $80 \mu\text{m}$ per tube, or about $35 \mu\text{m}$ per chamber.

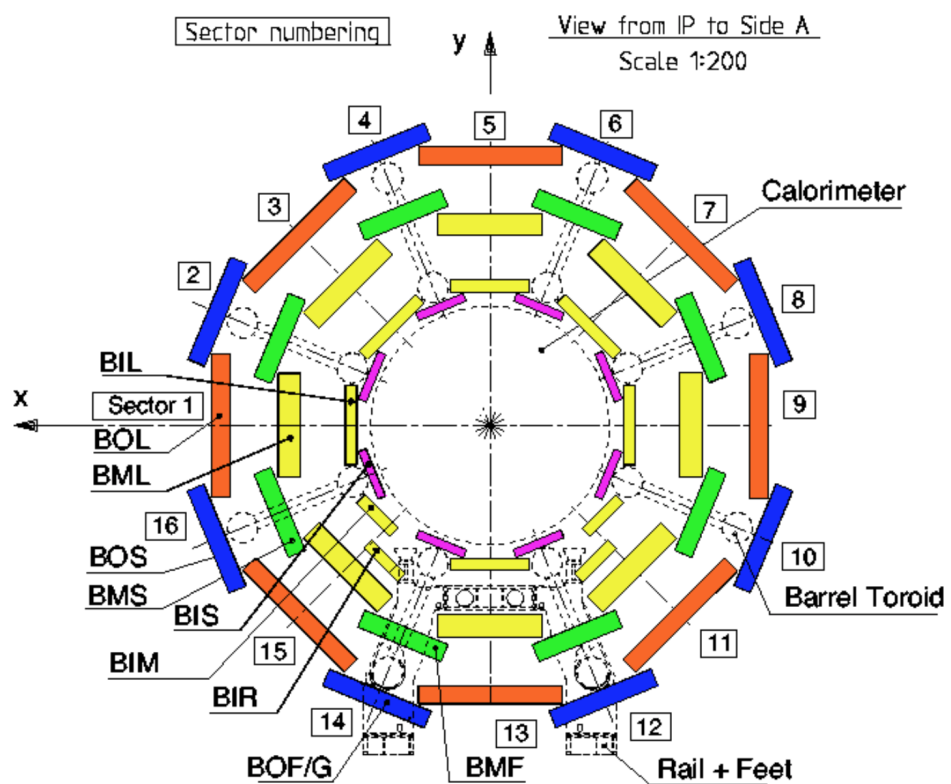


Figure 2.18: The cross section of the barrel region for the muon spectrometer. Three concentric cylindrical layers of barrel MDT are shown. [11]

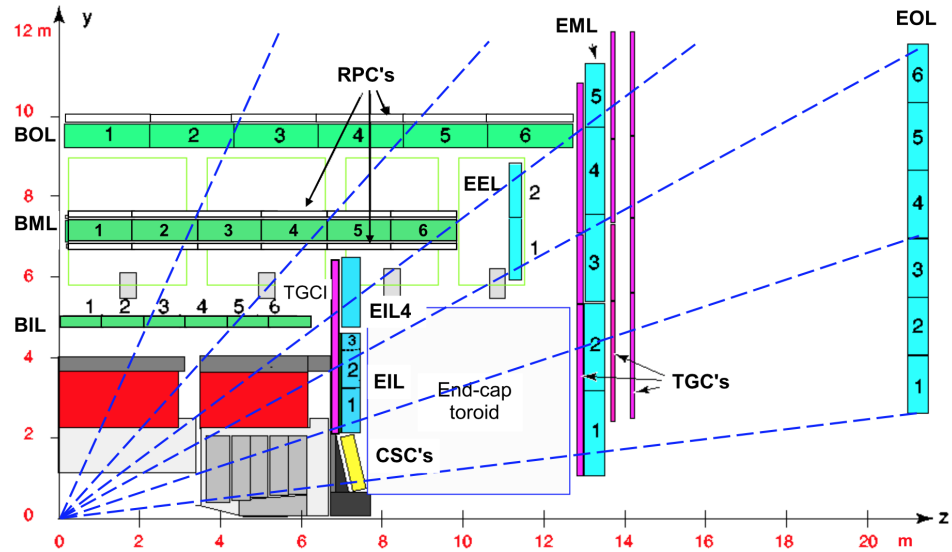


Figure 2.19: The cross section of the end-cap region for the muon spectrometer. Four layers of end-cap MDT are shown in blue colour. Three layers of barrel MDT are also shown in green colour. [11]

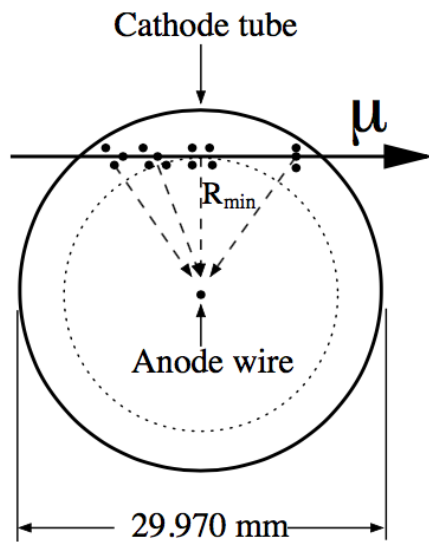


Figure 2.20: The cross-section of a MDT tube. When the muon passes through the tube, free electrons are produced along the track. The free electrons are drifted to the anode wire. [11]

Chapter 3

Dataset inputs and event selection

3.1 Dataset inputs

This chapter describes the dataset used in this analysis. The dataset contains the data samples and Monte-Carlo(MC) simulated sample. All dataset are SUSY2 DxAOD derivations, which aim for 2 or 3 leptons search.

3.1.1 Data samples

We use 2015 (periods D-H and J) and 2016 (periods A-L, I, K and L) pp -collisions data samples, at $\sqrt{s} = 13$ TeV. Only events in good condition are used, where LHC beams were stable and all ATLAS detectors were in good state. These good events are summarised in the Good Run Lists. The two Good Run Lists (GRL) in 2015 and 2016 data are shown the section [A.1](#). The integrated luminosities in 2015 and 2106 are 3.21 fb^{-1} and 32.86 fb^{-1} respectively, with relative error 2.1%. The list of data samples used in this analysis is shown the section [A.1](#).

3.1.2 MC samples

3.1.2.1 SM background

All MC samples are mc15c samples with offline release 20.7. All the background MC samples used in this analysis for each process are shown in the section [A.2](#) in appendix. Each sample has its cross section, k-factor, generator efficiency and its equivalent integrated luminosity. Some samples may overlap with each other.

t \bar{t} and single top The simulated events are generated by the POWHEG generator, and the CT10 PDF set is used. PYTHIA6 is also used for the parton shower model, with the PERUGIA 2012 tune. The mass of the top quark is assumed to be 172.5 GeV. The $t\bar{t}$ samples are normalized to the next-to-next-to-leading order of cross section, while the single top samples are normalized to the next-to-leading order of cross section.

W+jets and Z+jets The simulated events are generated by the SHERPA v2.2.1. The matrix elements are calculated at the next-to-leading order for up to two partons, and at the leading order for up to four partons, by using the COMIX and OPENLOOPS generators. The samples are normalized to the next-to-next-to-leading order QCD cross section. The files are separated according to the p_T of the vector boson and the presence of b -jet and c -jets.

Diboson The processes with four charged leptons ($\ell\ell\ell\ell$), three charged leptons and one neutrino ($\ell\ell\ell\nu$), and two charged leptons and two neutrinos ($\ell\ell\nu\nu$) are simulated by the SHERPA v2.2.1 generator. Diboson WW , WZ and ZZ processes with four or six electroweak vertices are also used.

Triboson The triboson processes WWW , WWZ , WZZ and ZZZ with up to six charged leptons are simulated by the SHERPA v2.2.1 generator.

ttV The processes ttW , ttZ , $ttWW$ and $ttWZ$ are simulated by MADGRAPH v2.2.2 at the leading-order, with PYTHIA for the parton shower model.

Higgs The WH and ZH processes are generated by using PYTHIA 8 generator, and the A14 set of tuned parameters is used together with the NNPDF23LO PDF set. The ttH processes are generated by using MCATNLO generator, interfaced with HERWIGPP. The CT10 PDF tuning is used along with the CTEQ6L1-UE-EE-5 tuning of parton shower.

3.1.2.2 Signal

The signal MC samples simulate the signal process $\tilde{\chi}_1^\pm \tilde{\chi}_2^0 \rightarrow W(\ell\nu)h$. They are generated by the MADGRAPH v2.2.3, calculated at the leading-order matrix elements with up to two extra partons. PYTHIA version 8.186 and the A14 tune

are also used for the modelling of the SUSY decay chain, parton showering and hadronization. Parton luminosities are provided by the NNPDF23LO PDF set. Table A.12 shows the list of signal samples used in this analysis, with different hypothesized masses point ($m_{\tilde{\chi}_1^\pm, \tilde{\chi}_2^0}$, $m_{\tilde{\chi}_1^0}$). These signal samples have been applied a selection that at least 2 leptons with $p_T > 7$ GeV is required. The efficiencies due to this selection are applied and also shown in the table.

3.2 Pre-selection and event cleaning

The following pre-selections on the events are applied to reject background which did not come from the proton-proton collision and to ensure that the detector was working properly.

- **Good Run List** The events need to pass the good run list. (For data only)
- **LAr/Tile/SCT error** Events with data integrity errors in the SCT detector and the LAr and Tile calorimeter are removed. (For data only)
- **Primary Vertex** The events need to have a primary vertex, which is defined as the one with the largest $\sum p_T^2$ of tracks, and has at least two tracks.
- **Cosmic Muon Veto** The events with cosmic muons need to be removed. The track of cosmic muon is identified by large impact parameters with respect to the primary vertex, with the condition that $|z_0^{PV}| > 1$ mm or $|d_0^{PV}| > 0.2$ mm.
- **Bad Muon Veto** The events with bad muons that does not come from the proton-proton collision need to be removed. The bad muon is identified by a large relative error in the ratio of electric charge to momentum (q/p), with the condition that $\sigma(q/p)/|q/p| > 0.2$, or by the “Bad” quality by the recommendation of the Muon CP group.
- **Bad Jet Veto** The events with bad jets that does not come from the proton-proton collision need to be removed. A jet with $p_T < 20$ GeV or with the “LooseBad” quality by the recommendation of the Jet/ E_T^{miss} group is identified as a bad jet.
- **Trigger Selection** The events need to pass at least one trigger in the trigger list, described in section 3.3.

- **Exactly 2 baseline leptons** The events which have exactly 2 baseline leptons are selected. The definition of baseline electron and muon are described in section 3.4. “The two leptons” mentioned in the later chapters refer to these 2 baseline leptons. These two leptons are indexed in the descending order by their p_T . The lepton with larger p_T is called the leading lepton (ℓ_1), and the lepton with smaller p_T is called the sub-leading lepton(ℓ_2).

3.3 Trigger strategy

The time-spacing between two adjacent bunches is 25 ns, and equivalently the frequency is 40 MHz. Because not all the collisions will be our interested events, and it is also infeasible to store all the events generated by the LHC to the permanent storage, the trigger strategy is used. The trigger system accepts and rejects the events immediately after the data is taken. The Level 1 trigger system filters the event from 40 MHz to 100 kHz. The High Level trigger (HLT) system uses the output from the Level 1 trigger system, and further filters the event from 100 kHz to 1 kHz

In our analysis, the single lepton trigger and di-lepton trigger was used. Table 3.1 and 3.2 show the list of triggers used in this analysis.

	Single electron	Single muon
2015	HLT_e24_lhmedium_L1EM20VH HLT_e60_lhmedium HLT_e120_lhloose	HLT_mu20_iloose_L1MU15 HLT_mu40
2016	HLT_e26_lhtight_nod0_ivarloose HLT_e60_lhmedium_nod0 HLT_e140_lhloose_nod0	HLT_mu26_imedium HLT_mu50

Table 3.1: List of the single lepton triggers used in this analysis.

3.4 Object definitions

The object definitions are based on `SUSYTools-00-08-60` and analysis release `Base,2.4.31`, and their associated performance packages.

	Di-electron	Di-muon	Electron-muon
2015	HLT_2e12_lhloose_L12EM10VH	HLT_mu18_mu8noL1	HLT_e17_lhloose_mu14 HLT_e7_lhmedium_mu24
2016	HLT_2e17_lhvloose_nod0	HLT_mu22_mu8noL1	HLT_e17_lhloose_nod0_mu14 HLT_e7_lhmedium_nod0_mu24

Table 3.2: List of the di-lepton triggers used in this analysis.

3.4.1 Elections

Electrons are reconstructed by using the recommendations from the egamma group and need to be inside the region $|\eta^{\text{cluster}}| < 2.47$. The baseline electrons are identified by the `LooseAndBLayerLLH` quality criterion and have $p_T > 10$ GeV. The signal electrons must be baseline electrons and satisfy additional criteria. At the signal level, the electron must satisfy the `MediumLLH` quality criterion and has $p_T > 25$ GeV. The working point for the isolation cut is `FixedCutTight`. The requirement for the impact parameter is $|z_0 \cdot \sin(\theta)| < 0.5$ mm and $|d_0/\sigma(d_0)| < 5$, recommended by the Tracking CP group. To reduce the charge flip background, `ChargeIDSelector` is used with the working point `Medium` at 97% efficiency. The selections for baseline and signal electrons are summarised in table 3.3.

3.4.2 Muons

Muons are reconstructed by using the recommendation from the MCP group and requiring $|\eta| < 2.4$. The baseline muons are identified by the `Medium` quality criterion and have $p_T > 10$ GeV. The signal muons must be baseline muons and satisfy additional criteria. The additional criteria are $p_T > 25$ GeV and isolation cut with the working point `GradientLoose`. The requirement for the impact parameter is $|z_0 \cdot \sin(\theta)| < 0.5$ mm and $|d_0/\sigma(d_0)| < 3$, recommended by the Tracking CP group. The selections for baseline and signal muons are summarised in table 3.3.

3.4.3 Jets

The baseline jets are reconstructed by the anti- k_t jet algorithm with the distance parameter $D = 0.4$. The baseline must has $p_T > 20$ GeV and $|\eta| < 2.8$. The signal jets are selected on top of the baseline jet, with additional criteria. The signal

	Baseline Electron	Baseline Muon
Acceptance	$p_T > 10 \text{ GeV}$, $ \eta^{\text{cluster}} < 2.47$	$p_T > 10 \text{ GeV}$, $ \eta < 2.4$
Quality	LooseAndBLayerLLH	Medium
	Signal Electron	Signal Muon
Acceptance	$p_T > 25 \text{ GeV}$	$p_T > 25 \text{ GeV}$
Quality	MediumLLH	Medium
Isolation Cut	FixedCutTight	GradientLoose
Impact parameter	$ z_0 \cdot \sin(\theta) < 0.5 \text{ mm}$ $ d_0/\sigma(d_0) < 5$	$ z_0 \cdot \sin(\theta) < 0.5 \text{ mm}$ $ d_0/\sigma(d_0) < 3$
ChargeIDSelector	Medium at 97% efficiency	-

Table 3.3: Summary of the electron and muon selection criteria. The signal selection requirements are applied on top of the baseline criteria.

jets need to further satisfy the Jet Vertex Tagger (JVT) cut that $\text{JVT} > 0.59$ if the jets have $p_T < 60 \text{ GeV}$ and $|\eta| < 2.4$. The b-jets are signal jets with b-tag, by using the MV2c10 b-tagging algorithm with `FixedCut` working point which has b-jet efficiency 77%. The selections of jets are summarised in table 3.4.

3.4.4 Missing transverse momentum

Based on the conservation of transverse momentum, the total transverse momentum of the missing particles, which were not detected by the detector, can be estimated by the total transverse momentum of particles which can be detected. The missing transverse momentum ($\mathbf{p}_T^{\text{miss}}$) is defined by the negative of the sum of transverse momentum of all electrons, muons, photons, jets and all other tracks associated with the primary vertex. The calibrated electrons, muons, photons and jet objects are used as the inputs. This missing transverse momentum can estimate the total transverse momentum of the missing neutrinos and hypothetical neutralinos. The Missing transverse energy (E_T^{miss}) is defined by the magnitude of the missing transverse momentum $\mathbf{p}_T^{\text{miss}}$.

3.4.5 Overlap Removal

The overlap removal (OR) is performed with the baseline objects (electrons, muons and jets) and follows the default prescription provided in the `SUSYTools`. The

	Baseline Jet
Collection	AntiKt4EMTopo
Acceptance	$p_T > 20 \text{ GeV}$, $ \eta < 2.8$
	Signal Jet
Acceptance	$p_T > 20 \text{ GeV}$, $ \eta < 2.8$
Jet vertex tagger	Medium working point $\text{JVT} > 0.59$ for $p_T < 60 \text{ GeV}$ and $ \eta < 2.4$
	B-Jet
Acceptance	$p_T > 20 \text{ GeV}$, $ \eta < 2.4$
b -tagging algorithm	MV2c10 algorithm
Working point	FixedCut with efficiency 77%

Table 3.4: Summary of the jet selection criteria.

objects are removed in the following order.

1. If a jet is within $\Delta R = \sqrt{(\Delta\eta)^2 + (\Delta\phi)^2} = 0.2$ of an electron:
 - If the jet is not b -tagged, then the jet is removed. It mostly originates from the calorimeter energy deposits by the electron shower.
 - If the jet is b -tagged, then the electron is removed. It is more likely that it results from the semi-leptonic decays of b -quarks.
2. Electrons within $\Delta R = 0.4$ of a jet are removed, in order to suppress electrons from semi-leptonic decays of c - and b -hadrons.
3. Muons within $\Delta R = 0.4$ of a jet are removed, in order to suppress muons from semi-leptonic decays of c - and b -hadrons.
4. Any calo-tagged muons sharing the same ID track with an electron are removed.
5. Any electrons sharing the same ID track with the remaining muons are removed.

Chapter 4

Signal Region

The signal region (SR) is a set of selections of events, such that the signal is rich and the background is small. It is designed to discover the new particles, or set a limit on the masses of the hypothetical particles. In the analysis, two signal regions are defined, SRjet1 and SRjet23. Number of signal jets for SRjet1 is 1, while number of signal jets for SRjet23 is 2 or 3. The details of the definition of these two signal regions will be described in section 4.2.

4.1 Discriminant variables

The discriminant variables are designed to define the signal regions. The discriminant variables need to have the ability to distinguish the signal events from the background events, by applying a cut on the discriminant variable. The following are the discriminant variables used in this analysis.

- n_{jets} : Number of signal jets:
- $n_{b\text{-jets}}$: Number of b -jets.
- p_T^1 : Transverse momentum of the leading lepton.
- p_T^2 : Transverse momentum of the sub-leading lepton.
- $\Delta\eta_{ll}$: The difference in pseudorapidity between the two leptons.

$$\Delta\eta_{ll} = |\eta_1 - \eta_2| \quad (4.1)$$

- m_{ll} : It is the invariant mass of the two leptons (i.e. the invariant mass of

the 4-momentum sum of the two leptons).

$$(m_{ll})^2 = (p_1 + p_2)^2 \quad (4.2)$$

- E_T^{miss} : The magnitude of the missing transverse momentum.

$$E_T^{\text{miss}} = |\mathbf{p}_T^{\text{miss}}| \quad (4.3)$$

- m_T : It is designed to reconstruct the mass of the W-boson. It is calculated by using the transverse momentum of the leading lepton and the missing transverse momentum, defined by equation 4.4. By using the approximation $|\mathbf{p}_T^1| > 10 \text{ GeV} \gg m_1$ (0.511 MeV or 106 MeV) and hence $E_T^1 = \sqrt{(m_1)^2 + |\mathbf{p}_T^1|^2} \approx |\mathbf{p}_T^1|$, it can be approximated by $m_T = \sqrt{2p_T^1 E_T^{\text{miss}} (1 - \cos \Delta\phi)}$, where $\Delta\phi$ is the azimuthal angle between the leading lepton and the missing transverse momentum.

$$(m_T)^2 = (E_T^1 + E_T^{\text{miss}})^2 - |\mathbf{p}_T^1 + \mathbf{p}_T^{\text{miss}}|^2 \quad (4.4)$$

$$\approx (|\mathbf{p}_T^1| + |\mathbf{p}_T^{\text{miss}}|)^2 - |\mathbf{p}_T^1 + \mathbf{p}_T^{\text{miss}}|^2 \quad (4.5)$$

$$= (p_T^1 + p_T^{\text{miss}})^2 - (\mathbf{p}_T^1 + \mathbf{p}_T^{\text{miss}}) \cdot (\mathbf{p}_T^1 + \mathbf{p}_T^{\text{miss}}) \quad (4.6)$$

$$= (p_T^1)^2 + (p_T^{\text{miss}})^2 + 2p_T^1 p_T^{\text{miss}} - (p_T^1)^2 - (p_T^{\text{miss}})^2 - 2\mathbf{p}_T^1 \cdot \mathbf{p}_T^{\text{miss}} \quad (4.7)$$

$$= 2p_T^1 p_T^{\text{miss}} - 2\mathbf{p}_T^1 \cdot \mathbf{p}_T^{\text{miss}} \quad (4.8)$$

$$= 2p_T^1 p_T^{\text{miss}} - 2p_T^1 p_T^{\text{miss}} \cos \Delta\phi \quad (4.9)$$

$$= 2p_T^1 p_T^{\text{miss}} (1 - \cos \Delta\phi) \quad (4.10)$$

$$m_T = \sqrt{2p_T^1 E_T^{\text{miss}} (1 - \cos \Delta\phi)} \quad (4.11)$$

- m_{eff} : Effective mass is defined as the sum of the transverse momenta of the two leptons, signal jets and the missing transverse energy.

$$m_{\text{eff}} = p_T^1 + p_T^2 + E_T^{\text{miss}} + \sum_{\text{signal jets}} p_T \quad (4.12)$$

- m_{lj} or m_{ljj} : m_{lj} is for the case that $n_{\text{jets}} = 1$ (i.e. SRjet1), while m_{ljj} is for the case that $n_{\text{jets}} = 2$ or 3 (i.e. SRjet23). It attempts to reconstruct the mass of the Higgs boson. It is defined as the invariant mass of the leading jet (i.e. the jet with the highest p_T) for SRjet1 or the di-jet system (i.e. the sum of the two leading jets) for SRjet23, and the closest lepton to the jet system, where the measure of distance is $\Delta R = \sqrt{(\Delta\phi)^2 + (\Delta\eta)^2}$. The details of the definition are shown below.

The 4-momentum of the jet system is defined as

$$p_{\text{jet-system}} = \begin{cases} p_{\text{jet1}} & \text{for SRjet1} \\ p_{\text{jet1}} + p_{\text{jet2}} & \text{for SRjet23} \end{cases} \quad (4.13)$$

The 4-momentum of the closest lepton is defined as

$$p_{\text{closest-lepton}} = \begin{cases} p_{\text{lepton1}} & \text{if } \Delta R(p_{\text{lepton1}}, p_{\text{jet-system}}) \leq \Delta R(p_{\text{lepton2}}, p_{\text{jet-system}}) \\ p_{\text{lepton2}} & \text{if } \Delta R(p_{\text{lepton1}}, p_{\text{jet-system}}) > \Delta R(p_{\text{lepton2}}, p_{\text{jet-system}}) \end{cases} \quad (4.14)$$

m_{lj} or m_{ljj} is defined as the invariant mass of the 4-momentum sum of the closest lepton and the jet system.

$$(m_{lj(j)})^2 = (p_{\text{closest-lepton}} + p_{\text{jet-system}})^2 \quad (4.15)$$

- m_{T2} : The “stransverse mass” (m_{T2}) is designed to set a lower bound on the masses of the unseen pair of charginos $\tilde{\chi}_1^\pm$ and neutralinos $\tilde{\chi}_2^0$. One side is for charginos $\tilde{\chi}_1^\pm$ and another side is for neutralinos $\tilde{\chi}_2^0$, as shown in figure 1.6. They are both assumed to decay into one lepton that can be detected, and into neutralinos $\tilde{\chi}_1^0$ and neutrino that cannot be detected and hence they contribute to the missing transverse momentum. The calculation of m_{T2} uses the transverse momentum of the two leptons (i.e. \mathbf{p}_T^1 and \mathbf{p}_T^2) and the missing transverse momentum $\mathbf{p}_T^{\text{miss}}$ as the inputs. It is defined by finding the minimum value over all possible transverse vectors \mathbf{q}_T , which is the trial missing transverse momentum on one side [20].

$$m_{T2} = \min_{\mathbf{q}_T} \left[\max \left(m_T(\mathbf{p}_T^1, \mathbf{q}_T), m_T(\mathbf{p}_T^2, \mathbf{p}_T^{\text{miss}} - \mathbf{q}_T) \right) \right] \quad (4.16)$$

Similar to equation 4.11, the transverse mass of two transverse momenta $m_T(\mathbf{p}_T, \mathbf{q}_T)$ is defined as follows.

$$m_T(\mathbf{p}_T, \mathbf{q}_T) = \sqrt{2p_T q_T (1 - \cos \Delta\phi)} \quad (4.17)$$

where $\Delta\phi$ is the azimuthal angle between the two transverse momenta.

4.2 Signal region optimization

This section describes how the signal region is found and optimized. The goal of the optimization is to increase the number of signal events N_s and decrease the

number of background event N_b . This study was done, before we look at the real data, and hence the MC samples were used for signal and background. The signal significance Z for large N_s and N_b is defined by

$$Z = \frac{N_s}{\sqrt{N_b + N_s}} \quad (4.18)$$

It measures how well the signal region is. The process of the signal region optimization is to increase the signal significance Z. The signal significance Z can be interpreted as the variable $z = \frac{x-\mu}{\sigma}$ in the standard normal distribution. The corresponding p-value can be interpreted as the probability that the excess in the number of signal events from the background event is just due to the statistical fluctuation. By changing the cuts on different discriminant variables, the maximum signal significance can be obtained, and the corresponding optimal cuts are the definition of the signal region.

Equation 4.18 is only valid for large N_s and N_b . Because N_s and N_b are often small, another sophisticated formula for the signal significance was used. Also, the systematic error and statistical error of N_b need to be taken account. A fixed systematic error 25% is used, and the total relative error σ_b is the sum of systematic and statistical error in quadrature.

$$\sigma_b = \sqrt{(25\%)^2 + \left(\frac{\Delta N_b}{N_b}\right)^2} \quad (4.19)$$

where ΔN_b is the statistical error of N_b . The signal significance is calculated by using the function `NumberCountingUtils::BinomialExpZ` provided in `RooStats`.

$$Z = \text{BinomialExpZ}(N_s, N_b, \sigma_b) \quad (4.20)$$

This method basically calculates the signal significance Z with the corresponding p-value and probability for the following case. A series of Bernoulli experiments is conducted with the number of trials $n = N_b + N_s + \frac{1}{\sigma_b^2}$ and the probability of success of each trial $p = 1/(1 + 1/(N_b\sigma_b^2))$ [21]. The corresponding p-value is the probability that the number of success is at least $N_b + N_s$. The connection between these Bernoulli experiments and our analysis will not be explained here, but what is important is that the signal significance Z calculated by the equation 4.20 is an approximation to our analysis. It is useful because it has the following properties.

- It is a continuous function. N_b and N_s can be non-integer. (cf. Poisson distribution)

- It is a smooth function. It is convenient for finding the maximum value.
- For large N_b and N_s , it reduces to equation 4.18.
- It is fast to compute.

By using the equation 4.20, an approximately optimal signal region can be found.

4.2.1 Pre-selection

Before the optimization, the following pre-selection is applied, on top of the selections in section 3.2.

- **Exactly 2 signal leptons** The events which have exactly 2 signal leptons are selected. This means that the two leptons must be signal leptons.
- **Same sign** The electric charges of the two leptons have the same sign. This is what we are looking for, described in section 1.5.
- **B-jet veto** To suppress the top background, the number of b-jets is 0.
- **Number of jet** Similar to the Run 1 analysis, two signal regions are defined according to the number of signal jets. One signal region has 1 signal jet, called “SRjet1”, and another has 2 or 3 signal jets, called “SRjet23”.

4.2.2 Samples

As mentioned before, MC samples were used for estimating the expected N_s and N_b in the process of optimization. For signal, the mass point $(m_{\tilde{\chi}_1^\pm, \tilde{\chi}_2^0}, m_{\tilde{\chi}_1^0}) = (225, 75)$ was used for SRjet1, while the mass point $(m_{\tilde{\chi}_1^\pm, \tilde{\chi}_2^0}, m_{\tilde{\chi}_1^0}) = (187.5, 37.5)$ was used for SRjet23. For the background, MC samples were used for diboson, triboson, ttV and Higgs. The fake lepton background estimated by the matrix method in section 5.2 was used, instead of using the corresponding MC samples, because the fake lepton background are the major background and the corresponding MC sample is not reliable. The data sample was also used when calculating the fake lepton background estimation. The plots after the pre-selection in section 4.2.1 (except the b-jet veto), but before the optimization, are shown in figure 4.1 and 4.2. The lower plots in the figures are the signal significance, after the corresponding cuts for that variables.

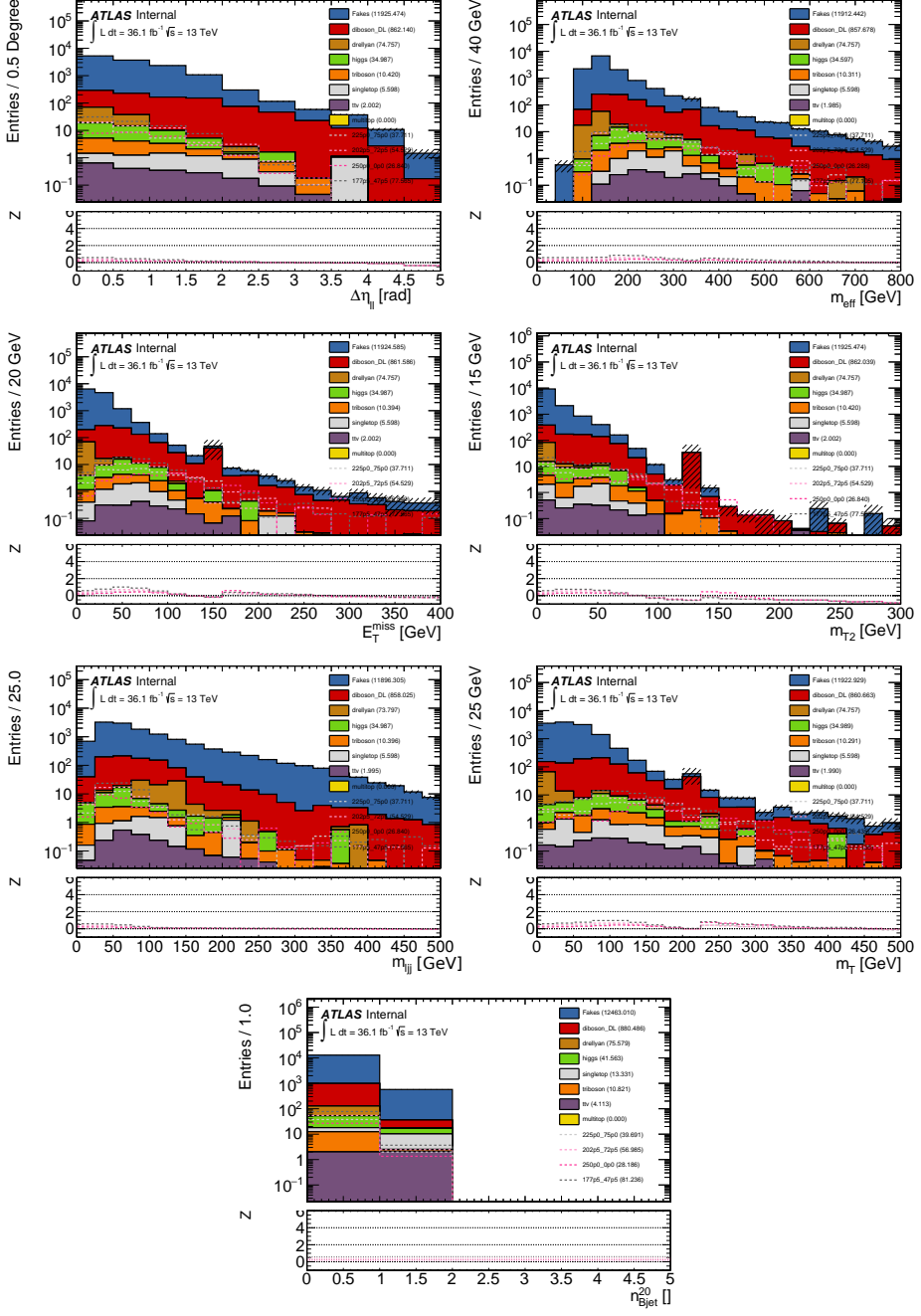


Figure 4.1: Distribution of the kinematic variables used for the optimization in SRjet1. The pre-selection, except the b-jet veto, has been applied. Only the statistical uncertainty is considered in the significance calculation.

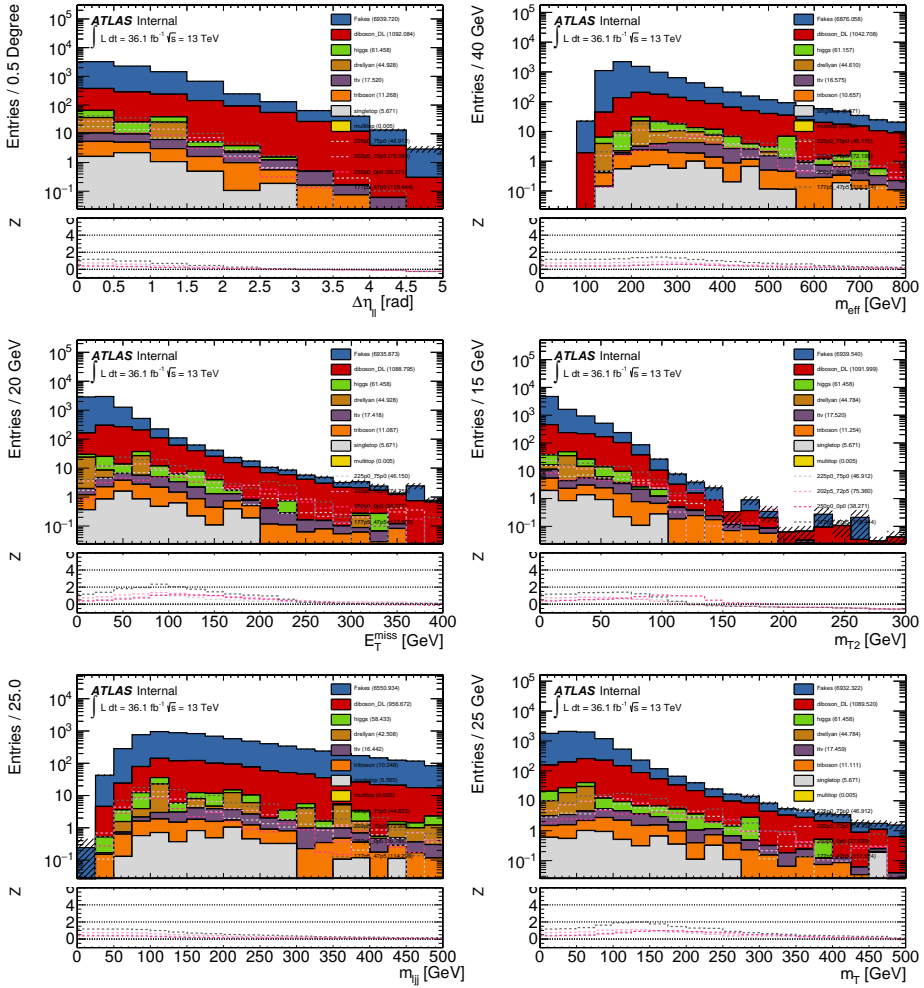


Figure 4.2: Distribution of the kinematic variables used for the optimization in SRjet23. The pre-selection, except the b-jet veto, has been applied. Only the statistical uncertainty is considered in the significance calculation.

4.2.3 Running for optimization

Some constraints were applied during the process of optimization, in order to have enough statistics to have reliable estimation of N_s and N_b .

- The yields (i.e. the sum of weighted events) for each process of background need to be positive, to have a reasonable and stable modelling of the background shape. Also, the HistFitter requires the background need to have positive yields.
- The diboson and ttV background have at least 10 unweighted events respectively, to have a reliable estimation for the main background processes from prompt leptons (i.e. not fake leptons).
- For E_T^{miss} , m_T , m_{eff} and m_{T2} , only lower cuts are applied.
- For $\Delta\eta_{ll}$ and $m_{lj(j)}$, only upper cuts are applied.

The list of variables used is shown in the table 4.1.

Variable	direction of cut
$\Delta\eta_{ll}$	upper cut
E_T^{miss}	lower cut
m_T	lower cut
m_{eff}	lower cut
$m_{lj(j)}$	upper cut
m_{T2}	lower cut

Table 4.1: Kinematic variables used in the optimization.

4.2.4 Results for optimization

The final results for the definitions of the two signal regions are shown in table 4.2. The yields for different background processes are shown in table 4.3. The N-1 plots for the discriminant variables are shown in figures 4.3 and 4.4. The N-1 plot means that the cut for that variable is removed, and the lower plot shows the signal significance after applying the cut at that value of that variable. Only statistical uncertainties are considered in the significance calculation in the lower plot.

Variable	SRjet1	SRjet23
$\Delta\eta_{ll}$	≤ 1.5	—
E_T^{miss}	$\geq 100 \text{ GeV}$	$\geq 100 \text{ GeV}$
m_T	$\geq 140 \text{ GeV}$	$\geq 120 \text{ GeV}$
m_{eff}	$\geq 260 \text{ GeV}$	$\geq 240 \text{ GeV}$
$m_{lj(j)}$	$< 180 \text{ GeV}$	$< 130 \text{ GeV}$
m_{T2}	$\geq 80 \text{ GeV}$	$\geq 70 \text{ GeV}$

Table 4.2: Final SR definitions

Background	SRjet1	SRjet23
Fake leptons	3.061	1.542
Total diboson	2.670 (396)	2.792 (596)
WW	0.4061	0.6472
ZZ	0.0157	0.0664
WZ	2.2481	2.0779
ttV	0.099 (34)	0.140 (66)
Triboson	0.446 (49)	0.204 (21)
Higgs	0.010 (5)	0.229 (21)
Wt	0.0	0.277 (1)
multitop	0.00	0.00
Drellyan	0.0	0.00

Table 4.3: The background yields in the two signal regions. The unweighed event are also shown in parentheses.

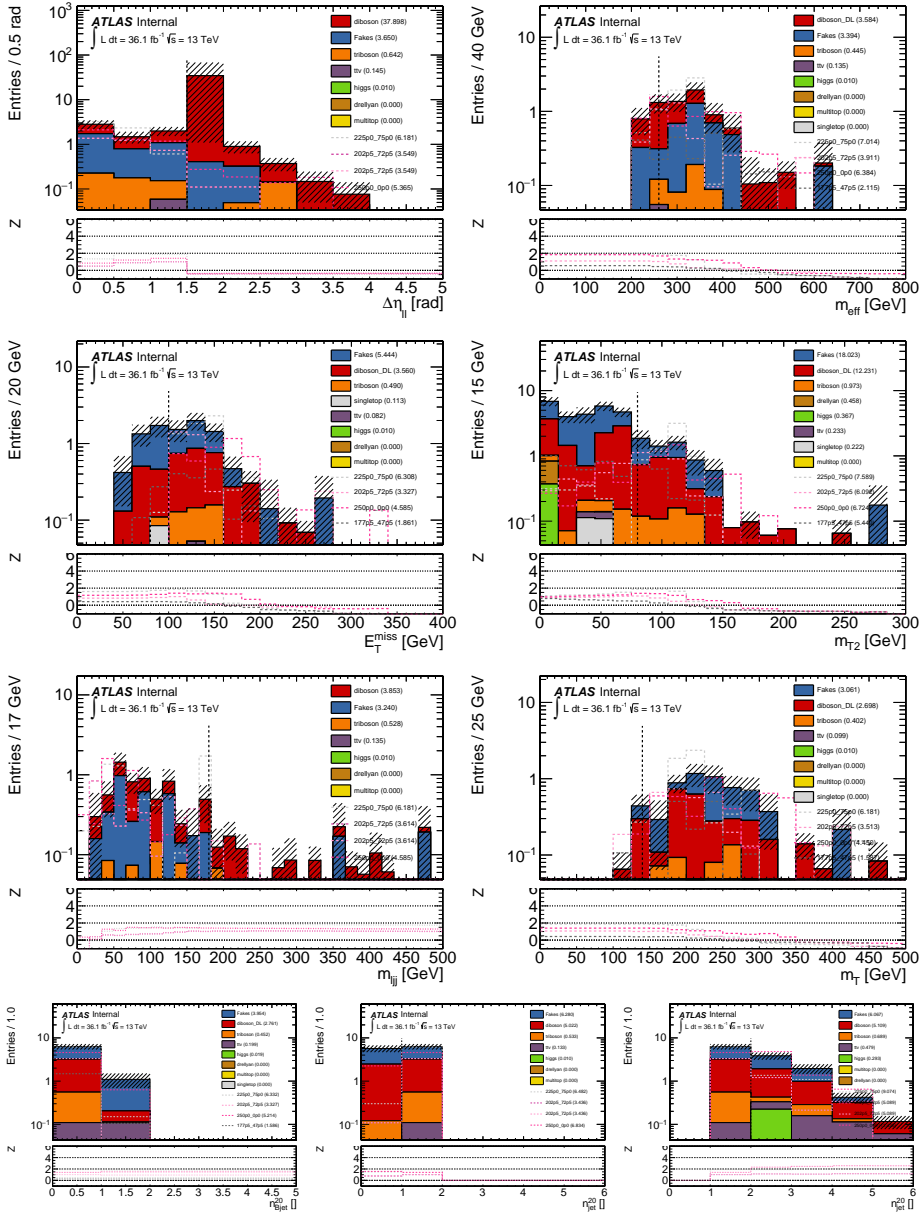


Figure 4.3: The N-1 plots for SRjet1. Only statistical uncertainties are considered in the significance calculation in the lower plot.

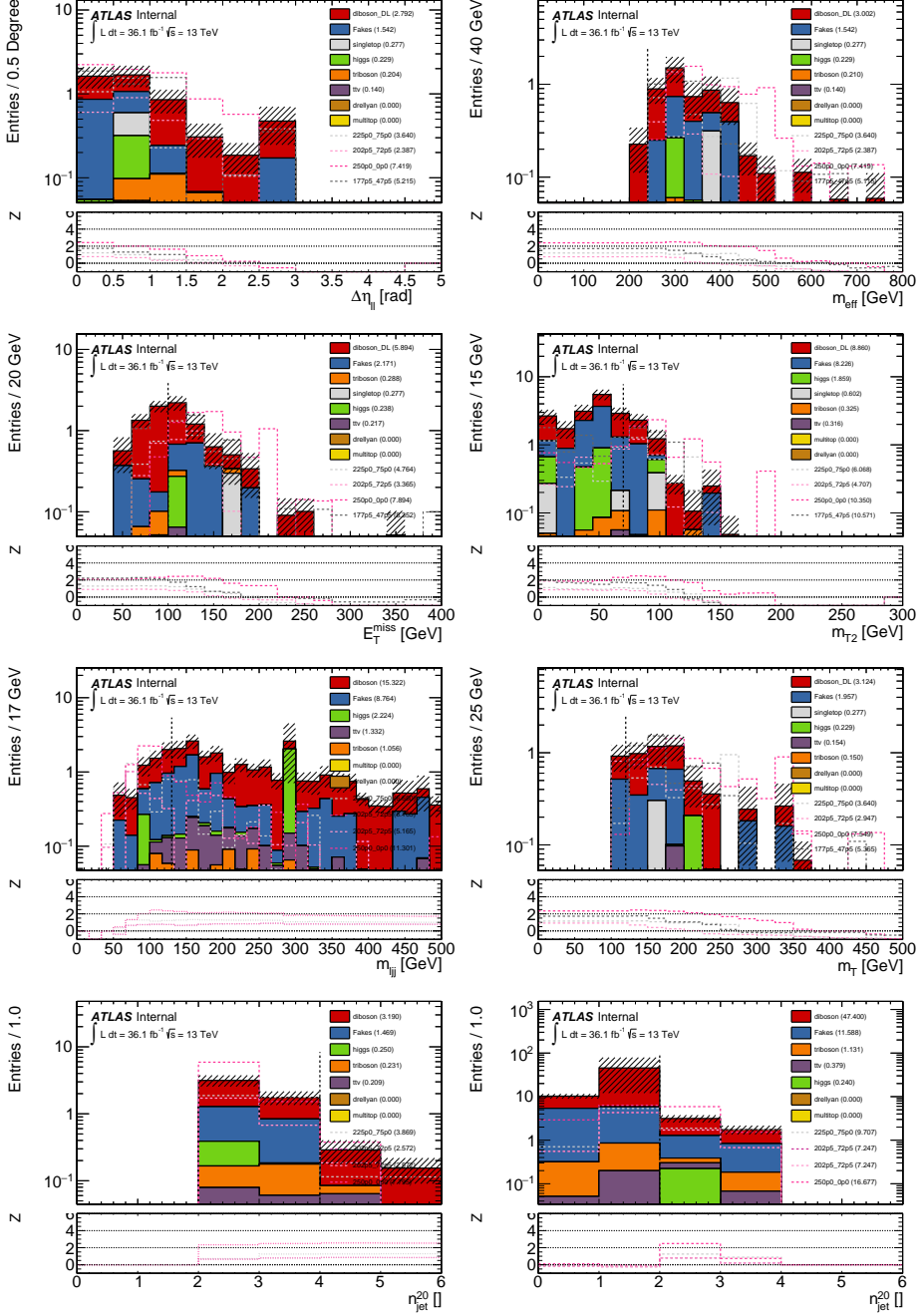


Figure 4.4: The N-1 plots for SRjet23. Only statistical uncertainties are considered in the significance calculation in the lower plot.

The expected combined signal significances for different mass points are shown in Figure 4.5. A flat 25 % systematic uncertainty are included. The combined signal significances are calculated by adding the signal significances of the two signal regions in quadrature. The figure shows considerable signal significances, in particular for the compressed region, where $m_{\tilde{\chi}_1^\pm, \tilde{\chi}_2^0} - m_{\tilde{\chi}_1^0}$ are close to the mass of Higgs boson (~ 125 GeV).

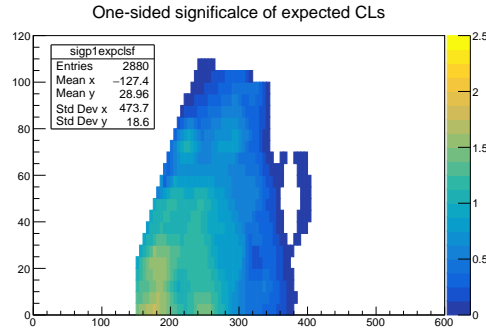


Figure 4.5: The expected combined signal significances for different mass points.

Chapter 5

Background estimation

The charge flip background and the fake lepton background are the two dominant backgrounds that their original particles in the final state come from the SM, but not the SUSY signal. Because of the mis-reconstruction, they pass the selections of the SRs. This type of background will be estimated by using the data-driven method.

5.1 charge flip background

5.1.1 Sources for charge flip background

The charge flip background is due to the mis-identification of the sign of the charge of a lepton, after the reconstruction. The sign of the charge is determined by the direction of the curvature of the track. There are two main sources for the mis-identification for the direction of the curvature.

The first source is described by the figure 5.1. It is the case that the lepton interacts with the material of the detector, and a photon is emitted by the process of bremsstrahlung. The emitted photon further produces a pair of electron and positron, namely the γ conversion. As shown in figure 5.1, if the most of the energy is carried by the positron e^+ (the purple track), the direction of the curvature of the reconstructed track (the orange track) will be reversed. Thus, the charge of the lepton is flipped. Because the amount of this mis-identification depends on the number of hits with the detector, and hence depends on $|\eta|$ of the original track.

The second source is described by the figure 5.2. When the p_T of the lepton

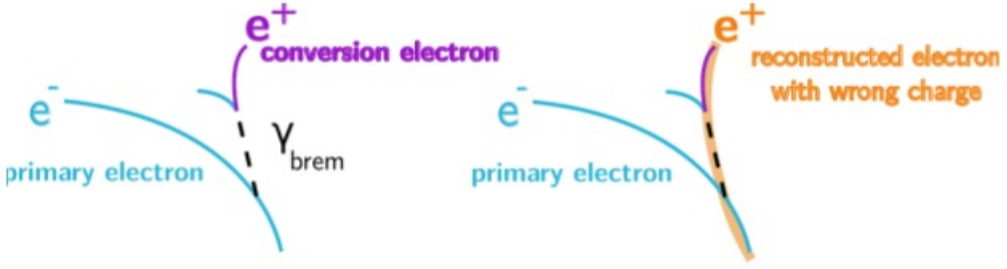


Figure 5.1: This shows how the track of the electron is incorrectly reconstructed (the orange track), due to the process of bremsstrahlung and γ conversion.

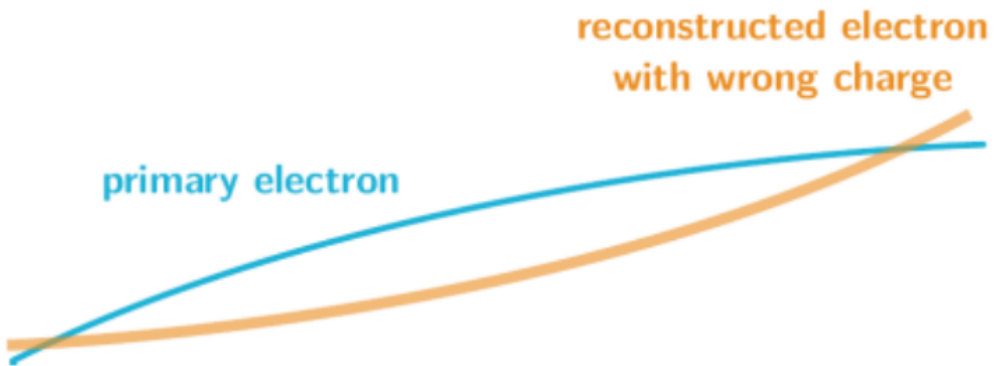


Figure 5.2: This shows how the track of the electron is incorrectly reconstructed (the orange track), due to very high p_T of the electron.

is very high, the track of the lepton will be almost a straight line. The curvature of the track will be close to zero, and the sign of the curvature will be difficult to distinguish. As a result, the sign of the charge of the lepton will be incorrectly assigned. The chance to have this problem obviously depends on p_T of the lepton.

Compared to an electron, the charge of a reconstructed muon will be less often to be mis-identified. The first reason is that a muon is heavier than an electron. This will reduce the chance of the process of bremsstrahlung. The second reason is that muons can reach to the muon spectrometer, which is the outer part of the detector, while most electrons cannot. This means that the length of the track of a muon, which can be detected by the tracker, is longer than that of an electron. Hence, the reconstructed curvature of the track for muons can be more accurate, and it reduces the chance of the mis-identification due to the high p_T . Because most of the charge flip background comes from electrons, we only estimate the

charge flip background for electrons.

5.1.2 Likelihood method

The probability that the charge of an electron is mis-identified is denoted by the charge-flip rate ϵ_i , where the index i represents the dependency on the p_T and η of the electron. The value of index i is found by splitting the variables p_T and $|\eta|$ into different 2-dimensional bins, and the binning for the p_T and $|\eta|$ is described by the table 5.1. The index i of ϵ_i is defined by the index of the bin.

Variable	Boundary of the bins
p_T (GeV)	25, 60, 90, 130, 150, 1000
$ \eta $	0, 0.50, 1.00, 1.37, 1.52, 1.80, 2.00, 2.47

Table 5.1: Binning in p_T and $|\eta|$ for the charge-flip rate ϵ_i .

Suppose that, before the reconstruction, there are m_{OS}^{ij} opposite-sign events with the leading lepton in bin i and the sub-leading lepton in bin j , and similarly there are m_{SS}^{ij} same-sign events. After the reconstruction, due to the charge flip, there are M_{OS}^{ij} opposite-sign events and M_{SS}^{ij} same-sign events. The number of events after the reconstruction is given by

$$M_{OS}^{ij} = (1 - \epsilon_i)(1 - \epsilon_j)m_{OS}^{ij} + \epsilon_i(1 - \epsilon_j)m_{SS}^{ij} + (1 - \epsilon_i)\epsilon_j m_{SS}^{ij} + \epsilon_i\epsilon_j m_{OS}^{ij} \quad (5.1)$$

$$M_{SS}^{ij} = (1 - \epsilon_i)(1 - \epsilon_j)m_{SS}^{ij} + \epsilon_i(1 - \epsilon_j)m_{OS}^{ij} + (1 - \epsilon_i)\epsilon_j m_{OS}^{ij} + \epsilon_i\epsilon_j m_{SS}^{ij} \quad (5.2)$$

From equation 5.2, the number of reconstructed same-sign events due to the real opposite-sign events, i.e. the charge flip BG , denoted by N_{SS}^{ij} , is

$$N_{SS}^{ij} = \epsilon_i(1 - \epsilon_j)m_{OS}^{ij} + (1 - \epsilon_i)\epsilon_j m_{OS}^{ij} \quad (5.3)$$

In the SRs, m_{OS}^{ij} is the number of OS events before the reconstruction, but finally pass all selections in SRs. M_{OS}^{ij} is the total number of events that pass all selections in SRs, but replace SS requirement by OS. Because m_{OS}^{ij} is much larger than m_{SS}^{ij} and the measured charge-flip rate ϵ_i is about 10^{-3} , m_{OS}^{ij} can be estimated by

$$M_{OS}^{ij} \approx (1 - \epsilon_i)(1 - \epsilon_j)m_{OS}^{ij} \quad (5.4)$$

$$m_{OS}^{ij} \approx \frac{M_{OS}^{ij}}{(1 - \epsilon_i)(1 - \epsilon_j)} \quad (5.5)$$

$$m_{OS}^{ij} \approx M_{OS}^{ij} \quad (5.6)$$

$$m_{OS}^{ij} \approx M_{OS}^{ij} + M_{SS}^{ij} \quad (5.7)$$

By substituting equation 5.7 into 5.3, the charge flip BG can be estimated by M_{OS}^{ij} , M_{SS}^{ij} and the charge-flip rate ϵ_i ,

$$N_{SS}^{ij} = \epsilon_i(1 - \epsilon_j)m_{OS}^{ij} + (1 - \epsilon_i)\epsilon_jm_{OS}^{ij} \quad (5.8)$$

$$= [\epsilon_i(1 - \epsilon_j) + (1 - \epsilon_i)\epsilon_j]m_{OS}^{ij} \quad (5.9)$$

$$\approx p_{ij}(M_{OS}^{ij} + M_{SS}^{ij}) \quad (5.10)$$

$$= p_{ij}N^{ij} \quad (5.11)$$

where p_{ij} and N^{ij} are

$$\begin{aligned} p_{ij} &= \epsilon_i(1 - \epsilon_j) + (1 - \epsilon_i)\epsilon_j \\ N^{ij} &= M_{OS}^{ij} + M_{SS}^{ij} \end{aligned} \quad (5.12)$$

The probability density function of N_{SS}^{ij} , with the given values of N^{ij} and ϵ_i , can be described by the Poisson distribution with the mean value $\lambda = p_{ij}N^{ij}$.

$$P(N_{SS}^{ij}|N^{ij}, \epsilon_i, \epsilon_j) = \frac{\lambda^{N_{SS}^{ij}}e^{-\lambda}}{N_{SS}^{ij}!} \quad (5.13)$$

$$= \frac{(p_{ij}N^{ij})^{N_{SS}^{ij}}e^{-p_{ij}N^{ij}}}{N_{SS}^{ij}!} \quad (5.14)$$

In order to estimate the charge flip BG, we need to measure the charge-flip rate ϵ_i . The charge-flip rate is measured as a function of p_T and $|\eta|$ by using a likelihood method, based on the 2015 and 2016 data. A control region is used to select $Z \rightarrow ee$ processes. Inside the control region, exactly 2 signal electrons are required. Also, a Z mass window of $80 \text{ GeV} < m_{ll} < 100 \text{ GeV}$ is used. In this control region, the total number of events N^{ij} and the SS events N_{SS}^{ij} in each bin can be measured. By using the equation 5.14, the charge-flip rate ϵ_i can be measured by using the following likelihood method.

The likelihood function L is defined by

$$L(\epsilon_i, \epsilon_j|N^{ij}, N_{SS}^{ij}) = \prod_{ij} P(N_{SS}^{ij}|N^{ij}, \epsilon_i, \epsilon_j) \quad (5.15)$$

$$= \prod_{ij} \frac{(p_{ij}N^{ij})^{N_{SS}^{ij}}e^{-p_{ij}N^{ij}}}{N_{SS}^{ij}!} \quad (5.16)$$

$$(5.17)$$

Given the measured values of N^{ij} and N_{SS}^{ij} in each bin, by maximizing the likelihood function over all possible values of ϵ_i , the value of ϵ_i can be estimated. By

taking the negative logarithm, it is equivalent to minimize $-\ln L$.

$$-\ln L = -\ln \prod_{ij} \frac{(p_{ij} N_{SS}^{ij})^{N_{SS}^{ij}} e^{-p_{ij} N_{SS}^{ij}}}{N_{SS}^{ij}!} \quad (5.18)$$

$$= -\sum_{ij} \ln \frac{(p_{ij} N_{SS}^{ij})^{N_{SS}^{ij}} e^{-p_{ij} N_{SS}^{ij}}}{N_{SS}^{ij}!} \quad (5.19)$$

$$= -\sum_{ij} \left[N_{SS}^{ij} \ln(p_{ij} N_{SS}^{ij}) - p_{ij} N_{SS}^{ij} - \ln(N_{SS}^{ij}!) \right] \quad (5.20)$$

$$= -\sum_{ij} \left[N_{SS}^{ij} \ln(p_{ij} N_{SS}^{ij}) - p_{ij} N_{SS}^{ij} \right] + \text{constant} \quad (5.21)$$

$$= -\sum_{ij} \left[N_{SS}^{ij} \ln(N^{ij}[\epsilon_i(1-\epsilon_j) + (1-\epsilon_i)\epsilon_j]) - N^{ij}[\epsilon_i(1-\epsilon_j) + (1-\epsilon_i)\epsilon_j] \right] + \text{constant} \quad (5.22)$$

5.1.3 Background subtraction

By minimizing $-\ln L$ described in the previous section, the value of the charge-flip rate ϵ_i can be measured by using the data in the control region. In order to have better input values of N^{ij} and N_{SS}^{ij} , the number of events should mainly come from $Z \rightarrow ee$ processes, and other processes should be subtracted. The number of events from other processes can be estimated by the sideband region: $60 \text{ GeV} < m_{ll} < 80 \text{ GeV}$ and $100 \text{ GeV} < m_{ll} < 120 \text{ GeV}$. The corrected values of N^{ij} and N_{SS}^{ij} are given by

$$N_{80,100;\text{corrected}} = N_{80,100} - 20 \left(\frac{N_{60,80} + N_{80,100}}{20 + 20} \right) \quad (5.23)$$

In the sideband subtraction, the number of events in the sideband region should be normalized to the width of the central region. In general, given the number of events in the central region N_{central} , the left sideband region N_{left} and the right sideband region N_{right} , and their corresponding width w_{central} , w_{left} and w_{right} , the corrected values $N_{\text{central},\text{corrected}}$ are given by

$$N_{\text{central},\text{corrected}} = N_{\text{central}} - w_{\text{central}} \left(\frac{N_{\text{left}} + N_{\text{right}}}{w_{\text{left}} + w_{\text{right}}} \right) \quad (5.24)$$

5.1.4 Results without systematic uncertainty

Figure 5.3 shows the measured values of the charge-flip rate ϵ_i by using the data. The errors only include the uncertainties in the likelihood method due to the statistics, denoted by $\epsilon_{\text{lik,data}}$.

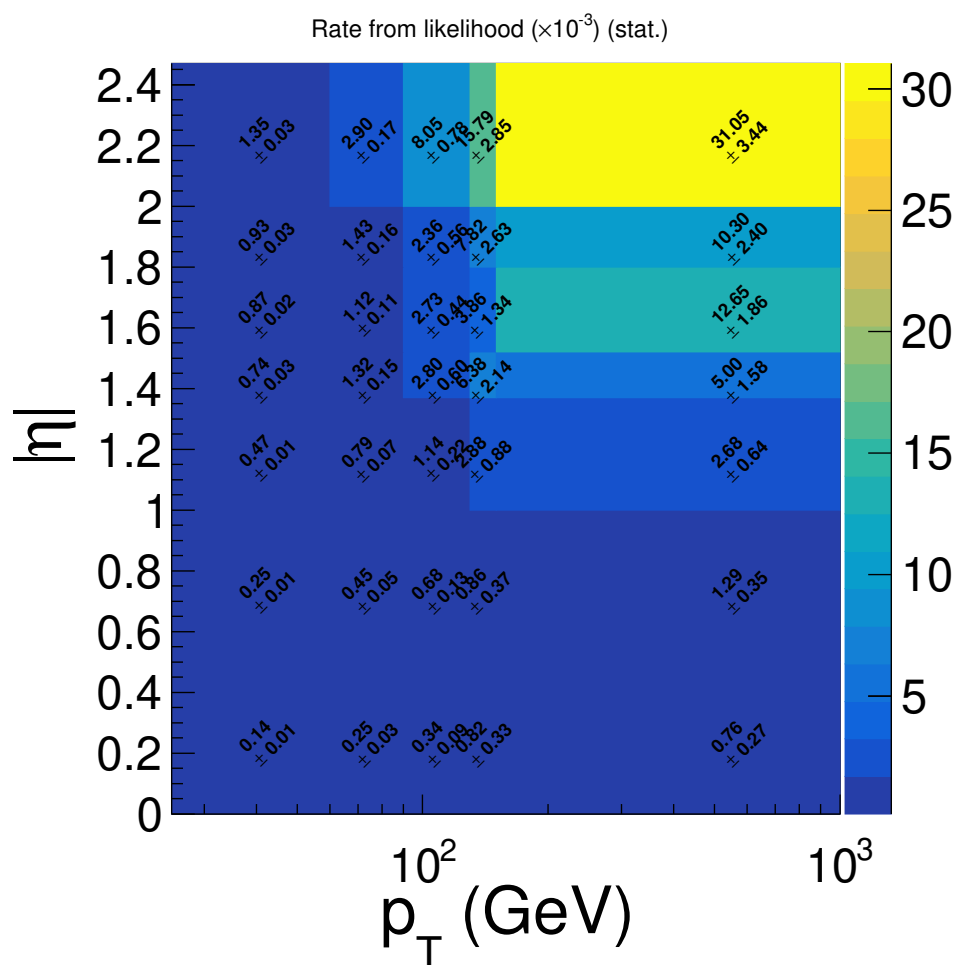


Figure 5.3: The measured values of the charge-flip rate ϵ_i in data. Only uncertainties due to the likelihood method are included.

5.1.5 Systematic uncertainties due to background subtraction

The systematic uncertainties due to background subtraction is estimated by the variations of different central widths and sideband widths. The following are the nominal central region and sideband region, and their 4 variations.

The nominal background subtraction:

- Central region: 80 - 100 GeV; Sideband width: 20 GeV

The 4 variations for background subtraction:

- Central region: 80 - 100 GeV; Sideband width: 15 GeV
- Central region: 80 - 100 GeV; Sideband width: 25 GeV
- Central region: 75 - 105 GeV; Sideband width: 20 GeV
- Central region: 80 - 100 GeV; no background subtraction

For each bin, the largest deviation from the nominal among these variations is the systematic uncertainty due to background subtraction.

$$\sigma_{\text{bgk}} = \max\{|\sigma_{\text{nominal}} - \sigma_{\text{variation}}|\} \quad (5.25)$$

Figure 5.4 shows the variations of the resulting charge flip rate, due to these 4 variations.

5.1.6 Systematic uncertainties due to likelihood method

The systematic uncertainties due to likelihood method are estimated by the difference between the likelihood method and the MC truth method. In the MC truth method, the charge-flip rate is estimated by using the truth information in $Z \rightarrow ee$ MC samples inside the control region. The control region requires exactly 2 signal electrons. The following are the procedures to match the reconstructed electron to the original electron, and hence the original electric charge can be found. Figure 5.5 shows how the original electron is found in the decay process described in figure 5.1. In this procedure, some reconstructed electrons will be ignored.

1. The reconstructed electron will be matched to the truth particle with the smallest ΔR within the cone $\Delta R < 0.1$. If no any truth particles can be found inside the cone, the reconstructed electron will be ignored.

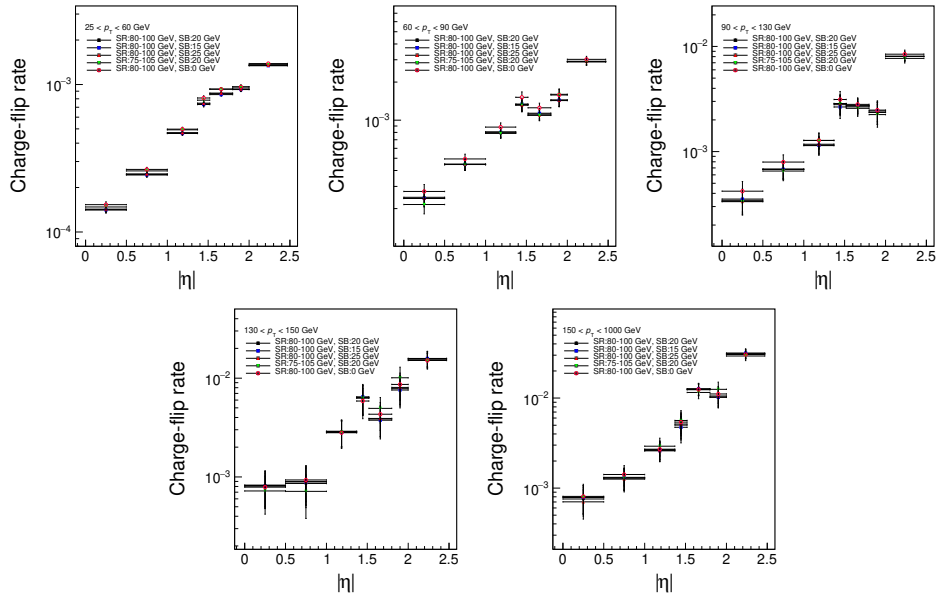


Figure 5.4: The systematic variations of the charge-flip rate ϵ_i in data, due to the background subtraction.

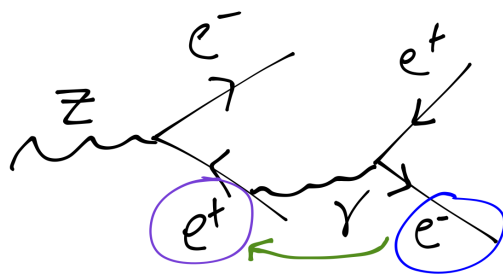


Figure 5.5: This diagram shows how the original electron is found through the decay chain.

2. If the truth particle is not an electron, it will be ignored.
3. If the origin of the truth electron is not a Z boson, it will be ignored.
4. If the daughter particle of the Z boson is not an electron, it will be ignored.
5. The charge of the daughter electron from the Z boson is the original charge of the reconstructed electron.

Only the events with two reconstructed electrons that are not ignored in the above procedure are considered. N_{total} is the total number of electrons in these events, and N_{flipped} is the number of electrons that the original charge and the reconstructed charge are different. By calculating the ratio in each bin, the charge flip rate can be estimated by using the MC truth information.

$$\epsilon_{\text{MC truth}} = \frac{N_{\text{flipped}}}{N_{\text{total}}} \quad (5.26)$$

The systematic uncertainties due to likelihood method σ_{truth} is then given by for MC,

$$\sigma_{\text{truth,MC}} = |\epsilon_{\text{lik,MC}} - \epsilon_{\text{MC truth}}| \quad (5.27)$$

for data,

$$\sigma_{\text{truth,data}} = \epsilon_{\text{lik,data}} \times \frac{\sigma_{\text{truth,MC}}}{\epsilon_{\text{lik,MC}}} \quad (5.28)$$

Figure 5.6 shows the comparison of the resulting charge flip rate, between the likelihood method and the MC truth method, by using the $Z \rightarrow ee$ MC samples.

5.1.7 Results with total uncertainties

The total systematic uncertainties is the quadratic sum of systematic uncertainties due to the background subtraction and the likelihood method, described in section 5.1.5 and 5.1.6 respectively.

$$\sigma_{\text{sys}} = \sqrt{\sigma_{\text{bgk}}^2 + \sigma_{\text{truth}}^2} \quad (5.29)$$

The total uncertainties is the quadratic sum of the total systematic uncertainties and the statistical uncertainties in the likelihood method.

$$\sigma_{\text{tot}} = \sqrt{\sigma_{\text{sys}}^2 + \sigma_{\text{lik}}^2} \quad (5.30)$$

Figure 5.7 shows the measured values of the charge-flip rate ϵ_i by using the data, with total uncertainties described in equation 5.30.

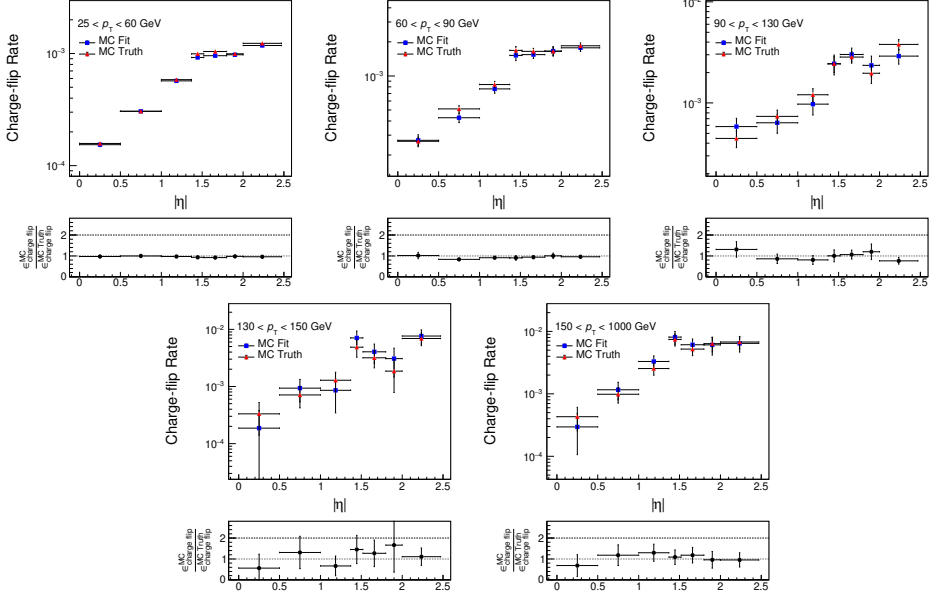


Figure 5.6: The comparison between the likelihood method and the MC truth method, by using the $Z \rightarrow ee$ MC samples. Hence, the systematic uncertainties due to likelihood method can be estimated.

5.1.8 MC validation

The charge flip rate can be validated by using the $Z \rightarrow ee$ MC samples. By using the equation 5.5 and 5.9, N_{SS}^{ij} can be approximated by

$$N_{SS}^{ij} = [\epsilon_i(1 - \epsilon_j) + (1 - \epsilon_i)\epsilon_j]m_{OS}^{ij} \quad (5.31)$$

$$\approx [\epsilon_i(1 - \epsilon_j) + (1 - \epsilon_i)\epsilon_j] \frac{M_{OS}^{ij}}{(1 - \epsilon_i)(1 - \epsilon_j)} \quad (5.32)$$

$$= \frac{\epsilon_i(1 - \epsilon_j) + (1 - \epsilon_i)\epsilon_j}{(1 - \epsilon_i)(1 - \epsilon_j)} M_{OS}^{ij} \quad (5.33)$$

Also, in the equation 5.2, m_{SS}^{ij} is zero for the $Z \rightarrow ee$ MC samples, we have

$$M_{SS}^{ij} = \epsilon_i(1 - \epsilon_j)m_{OS}^{ij} + (1 - \epsilon_i)\epsilon_j m_{OS}^{ij} \quad (5.34)$$

$$= N_{SS}^{ij} \quad (5.35)$$

Hence, it is expected that

$$M_{SS}^{ij} \approx \frac{\epsilon_i(1 - \epsilon_j) + (1 - \epsilon_i)\epsilon_j}{(1 - \epsilon_i)(1 - \epsilon_j)} M_{OS}^{ij} \quad (5.36)$$

By weighting the OS events in MC with the weight,

$$\text{weight} = \frac{\epsilon_i(1 - \epsilon_j) + (1 - \epsilon_i)\epsilon_j}{(1 - \epsilon_i)(1 - \epsilon_j)} \quad (5.37)$$

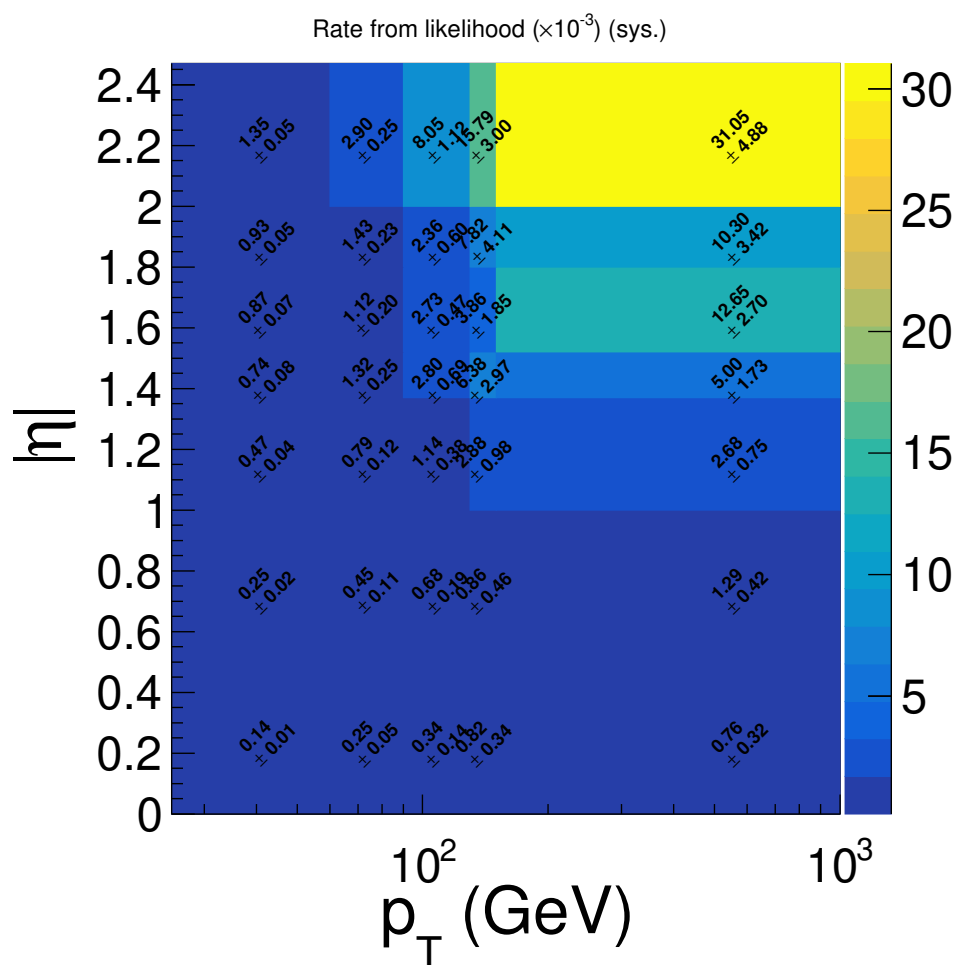


Figure 5.7: The measured values of the charge-flip rate ϵ_i in data, with total uncertainties.

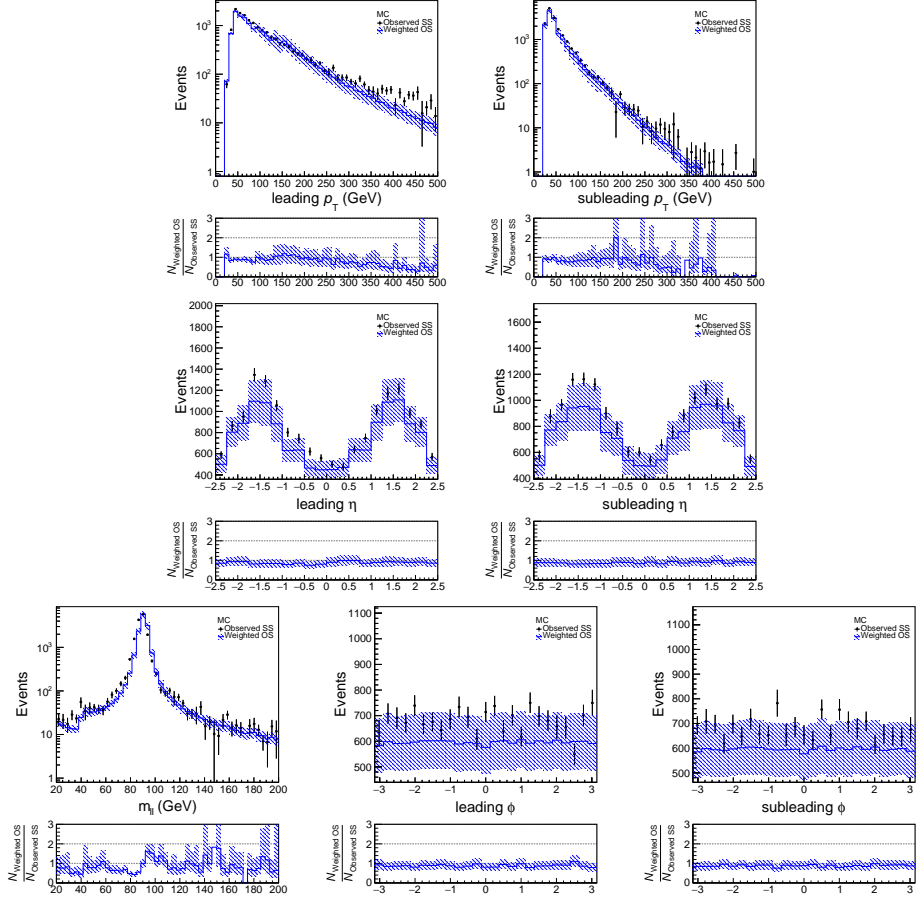


Figure 5.8: The comparison between the weighted OS events and the SS events, with different variables.

the weighted OS events and the SS events will be close to each other. This can be used to validate the charge flip rate. Figure shows the comparison between the weighted OS events and the SS events, with different variables. All event weights are applied, except the charge flip scale factor. The weighted OS events and the SS events agree within the uncertainties.

5.2 Fake lepton background

5.2.1 Sources for fake lepton background

The fake lepton background is ascribed to the case that other particle like meson, hadron and photon is mis-identified as a lepton, after the reconstruction. Three types of fake lepton background are described as follows.

- Heavy-flavor fakes:

- It comes from semi-leptonic decays of heavy-quark (b or c) hadrons in jets
- Light-flavor fakes:
 - It comes from semi-leptonic decays of light-quark hadrons in jets
 - or is due to mis-reconstructions of jets with light-quark hadrons
- photon conversion:
 - It comes from the pair production from a photon

These leptons do not often pass the lepton identification cuts and have large impact parameters. They are also not well-isolated.

5.2.2 Matrix method

The fake lepton background is estimated by the matrix method. The input of this method is the real and fake efficiencies of electron and muon, in different bins of p_T and $|\eta|$, which is measured in the following sections. This method will estimate the amount of fake lepton background, by counting the number of loose and tight leptons in data. The tight leptons in our analysis are the signal leptons, and the loose leptons are baseline leptons but not signal leptons.

The probability that a real electron (or muon) passes the signal selection (i.e. tight lepton) is denoted by the real efficiency ϵ . The probability that a real electron (or muon) does not pass the signal selection (i.e. loose lepton) is denoted by $\bar{\epsilon} = 1 - \epsilon$. Similarly, the probability that a fake electron (or muon) passes the signal selection (i.e. tight lepton) is denoted by the fake efficiency f . The probability that a fake electron (or muon) does not pass the signal selection (i.e. loose lepton) is denoted by $\bar{f} = 1 - f$. Although there is no subscripts and superscripts for the efficiencies e and f , these efficiencies are different for different flavours of the leptons (electron or muon), and also in different p_T - $|\eta|$ bins.

For simplicity, we first consider the case with only one leptons. We will then generalize to the case with two leptons. By the definition of the efficiencies, the relation between the number of real/fake leptons and the number of tight/loose leptons is given by the following matrix.

$$\begin{pmatrix} N_T \\ N_L \end{pmatrix} = \begin{pmatrix} \epsilon & f \\ \bar{\epsilon} & \bar{f} \end{pmatrix} \begin{pmatrix} N_R \\ N_F \end{pmatrix} \quad (5.38)$$

Because the number of tight/loose leptons can be counted in data, $\begin{pmatrix} N_T \\ N_L \end{pmatrix}$ is known. By inverting the matrix, the original number of fake leptons can be calculated.

$$\begin{pmatrix} 0 \\ N_F \end{pmatrix} = \begin{pmatrix} 0 & 0 \\ 0 & 1 \end{pmatrix} \begin{pmatrix} N_R \\ N_F \end{pmatrix} \quad (5.39)$$

$$= \begin{pmatrix} 0 & 0 \\ 0 & 1 \end{pmatrix} \begin{pmatrix} \epsilon & f \\ \bar{\epsilon} & \bar{f} \end{pmatrix}^{-1} \begin{pmatrix} N_T \\ N_L \end{pmatrix}$$

The fake lepton background, which is the number of tight lepton due to the fake lepton, N'_T , can then be found, by re-apply the matrix in equation 5.38.

$$\begin{pmatrix} N'_T \\ N'_L \end{pmatrix} = \begin{pmatrix} \epsilon & f \\ \bar{\epsilon} & \bar{f} \end{pmatrix} \begin{pmatrix} 0 \\ N_F \end{pmatrix} \quad (5.40)$$

$$= \begin{pmatrix} \epsilon & f \\ \bar{\epsilon} & \bar{f} \end{pmatrix} \begin{pmatrix} 0 & 0 \\ 0 & 1 \end{pmatrix} \begin{pmatrix} \epsilon & f \\ \bar{\epsilon} & \bar{f} \end{pmatrix}^{-1} \begin{pmatrix} N_T \\ N_L \end{pmatrix}$$

$$N'_T = \begin{pmatrix} \epsilon & f \end{pmatrix} \begin{pmatrix} 0 & 0 \\ 0 & 1 \end{pmatrix} \begin{pmatrix} \epsilon & f \\ \bar{\epsilon} & \bar{f} \end{pmatrix}^{-1} \begin{pmatrix} N_T \\ N_L \end{pmatrix}$$

To generalize to the case with two leptons, equation 5.38 becomes

$$\begin{pmatrix} N_{TT} \\ N_{TL} \\ N_{LT} \\ N_{LL} \end{pmatrix} = \begin{pmatrix} \epsilon_1 \epsilon_2 & \epsilon_1 f_2 & f_1 \epsilon_2 & f_1 f_2 \\ \epsilon_1 \bar{\epsilon}_2 & \epsilon_1 \bar{f}_2 & f_1 \bar{\epsilon}_2 & f_1 \bar{f}_2 \\ \bar{\epsilon}_1 \epsilon_2 & \bar{\epsilon}_1 f_2 & \bar{f}_1 \epsilon_2 & \bar{f}_1 f_2 \\ \bar{\epsilon}_1 \bar{\epsilon}_2 & \bar{\epsilon}_1 \bar{f}_2 & \bar{f}_1 \bar{\epsilon}_2 & \bar{f}_1 \bar{f}_2 \end{pmatrix} \begin{pmatrix} N_{RR} \\ N_{RF} \\ N_{FR} \\ N_{FF} \end{pmatrix} \quad (5.41)$$

where the subscripts 1 and 2 of the efficiencies denote the leading lepton and sub-leading lepton respectively. The two letters in the subscript of N describe the types of the leading and sub-leading lepton respectively. N_{RF} , N_{FR} , N_{FF} can be

found by inverting the matrix.

$$\begin{aligned}
\begin{pmatrix} 0 \\ N_{RF} \\ N_{FR} \\ N_{FF} \end{pmatrix} &= \begin{pmatrix} 0 & 0 & 0 & 0 \\ 0 & 1 & 0 & 0 \\ 0 & 0 & 1 & 0 \\ 0 & 0 & 0 & 1 \end{pmatrix} \begin{pmatrix} N_{RR} \\ N_{RF} \\ N_{FR} \\ N_{FF} \end{pmatrix} \\
&= \begin{pmatrix} 0 & 0 & 0 & 0 \\ 0 & 1 & 0 & 0 \\ 0 & 0 & 1 & 0 \\ 0 & 0 & 0 & 1 \end{pmatrix} \begin{pmatrix} \epsilon_1\epsilon_2 & \epsilon_1f_2 & f_1\epsilon_2 & f_1f_2 \\ \epsilon_1\bar{\epsilon}_2 & \epsilon_1\bar{f}_2 & f_1\bar{\epsilon}_2 & f_1\bar{f}_2 \\ \bar{\epsilon}_1\epsilon_2 & \bar{\epsilon}_1f_2 & \bar{f}_1\epsilon_2 & \bar{f}_1f_2 \\ \bar{\epsilon}_1\bar{\epsilon}_2 & \bar{\epsilon}_1\bar{f}_2 & \bar{f}_1\bar{\epsilon}_2 & \bar{f}_1\bar{f}_2 \end{pmatrix}^{-1} \begin{pmatrix} N_{TT} \\ N_{TL} \\ N_{LT} \\ N_{LL} \end{pmatrix}
\end{aligned} \tag{5.42}$$

The fake lepton background, which is the number of tight-tight lepton due to the fake lepton, N'_{TT} , can then be found.

$$\begin{aligned}
\begin{pmatrix} N'_{TT} \\ N'_{TL} \\ N'_{LT} \\ N'_{LL} \end{pmatrix} &= \begin{pmatrix} \epsilon_1\epsilon_2 & \epsilon_1f_2 & f_1\epsilon_2 & f_1f_2 \\ \epsilon_1\bar{\epsilon}_2 & \epsilon_1\bar{f}_2 & f_1\bar{\epsilon}_2 & f_1\bar{f}_2 \\ \bar{\epsilon}_1\epsilon_2 & \bar{\epsilon}_1f_2 & \bar{f}_1\epsilon_2 & \bar{f}_1f_2 \\ \bar{\epsilon}_1\bar{\epsilon}_2 & \bar{\epsilon}_1\bar{f}_2 & \bar{f}_1\bar{\epsilon}_2 & \bar{f}_1\bar{f}_2 \end{pmatrix} \begin{pmatrix} 0 \\ N_{RF} \\ N_{FR} \\ N_{FF} \end{pmatrix} \\
&= \begin{pmatrix} \epsilon_1\epsilon_2 & \epsilon_1f_2 & f_1\epsilon_2 & f_1f_2 \\ \epsilon_1\bar{\epsilon}_2 & \epsilon_1\bar{f}_2 & f_1\bar{\epsilon}_2 & f_1\bar{f}_2 \\ \bar{\epsilon}_1\epsilon_2 & \bar{\epsilon}_1f_2 & \bar{f}_1\epsilon_2 & \bar{f}_1f_2 \\ \bar{\epsilon}_1\bar{\epsilon}_2 & \bar{\epsilon}_1\bar{f}_2 & \bar{f}_1\bar{\epsilon}_2 & \bar{f}_1\bar{f}_2 \end{pmatrix} \begin{pmatrix} 0 & 0 & 0 & 0 \\ 0 & 1 & 0 & 0 \\ 0 & 0 & 1 & 0 \\ 0 & 0 & 0 & 1 \end{pmatrix} \begin{pmatrix} \epsilon_1\epsilon_2 & \epsilon_1f_2 & f_1\epsilon_2 & f_1f_2 \\ \epsilon_1\bar{\epsilon}_2 & \epsilon_1\bar{f}_2 & f_1\bar{\epsilon}_2 & f_1\bar{f}_2 \\ \bar{\epsilon}_1\epsilon_2 & \bar{\epsilon}_1f_2 & \bar{f}_1\epsilon_2 & \bar{f}_1f_2 \\ \bar{\epsilon}_1\bar{\epsilon}_2 & \bar{\epsilon}_1\bar{f}_2 & \bar{f}_1\bar{\epsilon}_2 & \bar{f}_1\bar{f}_2 \end{pmatrix}^{-1} \begin{pmatrix} N_{TT} \\ N_{TL} \\ N_{LT} \\ N_{LL} \end{pmatrix} \\
N'_{TT} &= \left(\begin{matrix} \epsilon_1\epsilon_2 & \epsilon_1f_2 & f_1\epsilon_2 & f_1f_2 \end{matrix} \right) \begin{pmatrix} 0 & 0 & 0 & 0 \\ 0 & 1 & 0 & 0 \\ 0 & 0 & 1 & 0 \\ 0 & 0 & 0 & 1 \end{pmatrix} \begin{pmatrix} \epsilon_1\epsilon_2 & \epsilon_1f_2 & f_1\epsilon_2 & f_1f_2 \\ \epsilon_1\bar{\epsilon}_2 & \epsilon_1\bar{f}_2 & f_1\bar{\epsilon}_2 & f_1\bar{f}_2 \\ \bar{\epsilon}_1\epsilon_2 & \bar{\epsilon}_1f_2 & \bar{f}_1\epsilon_2 & \bar{f}_1f_2 \\ \bar{\epsilon}_1\bar{\epsilon}_2 & \bar{\epsilon}_1\bar{f}_2 & \bar{f}_1\bar{\epsilon}_2 & \bar{f}_1\bar{f}_2 \end{pmatrix}^{-1} \begin{pmatrix} N_{TT} \\ N_{TL} \\ N_{LT} \\ N_{LL} \end{pmatrix}
\end{aligned} \tag{5.43}$$

Equation 5.43 can be applied to any combination of the flavour, p_T and $|\eta|$ of the leading and sub-leading lepton. In principle, the total amount of fake lepton background should be the summation of all combination of the flavour, p_T and $|\eta|$. For a particular combination, the counting result of the tight/loose leptons in

data $\begin{pmatrix} N_{TT} \\ N_{TL} \\ N_{LT} \\ N_{LL} \end{pmatrix}$ can be split into “one”, which is the contribution by one event.

$$\begin{pmatrix} N_{TT} \\ N_{TL} \\ N_{LT} \\ N_{LL} \end{pmatrix} = \sum_{i=1}^{N_{TT}} \begin{pmatrix} 1 \\ 0 \\ 0 \\ 0 \end{pmatrix} + \sum_{i=1}^{N_{TL}} \begin{pmatrix} 0 \\ 1 \\ 0 \\ 0 \end{pmatrix} + \sum_{i=1}^{N_{LT}} \begin{pmatrix} 0 \\ 0 \\ 1 \\ 0 \end{pmatrix} + \sum_{i=1}^{N_{LL}} \begin{pmatrix} 0 \\ 0 \\ 0 \\ 1 \end{pmatrix} \quad (5.44)$$

Because equation 5.43 is a linear function, we can first calculate the small contribution of N'_{TT} from one event, and assign this value as a weight to the event. This weight is called the fake weight of the event. The total fake lepton background is then the sum of the fake weight of all events in data. For example, if the pair of the two leptons is a tight-tight pair, the fake weight of this event is N'_{TT} in the following equation.

$$N'_{TT} = \begin{pmatrix} \epsilon_1\epsilon_2 & \epsilon_1f_2 & f_1\epsilon_2 & f_1f_2 \end{pmatrix} \begin{pmatrix} 0 & 0 & 0 & 0 \\ 0 & 1 & 0 & 0 \\ 0 & 0 & 1 & 0 \\ 0 & 0 & 0 & 1 \end{pmatrix} \begin{pmatrix} \epsilon_1\epsilon_2 & \epsilon_1f_2 & f_1\epsilon_2 & f_1f_2 \\ \epsilon_1\bar{\epsilon}_2 & \epsilon_1\bar{f}_2 & f_1\bar{\epsilon}_2 & f_1\bar{f}_2 \\ \bar{\epsilon}_1\epsilon_2 & \bar{\epsilon}_1f_2 & \bar{f}_1\epsilon_2 & \bar{f}_1f_2 \\ \bar{\epsilon}_1\bar{\epsilon}_2 & \bar{\epsilon}_1\bar{f}_2 & \bar{f}_1\bar{\epsilon}_2 & \bar{f}_1\bar{f}_2 \end{pmatrix}^{-1} \begin{pmatrix} 1 \\ 0 \\ 0 \\ 0 \end{pmatrix} \quad (5.45)$$

where the flavours, p_T and $|\eta|$ of the efficiencies is simply the flavours, p_T and $|\eta|$ of the leading and sub-leading lepton in this event.

By calculating the inverse of the matrix, equation 5.43 can be simplified. First, we define a variable d .

$$d = (\epsilon_1 - f_1)(\epsilon_2 - f_2) \quad (5.46)$$

The inverse of the matrix is given by

$$\begin{pmatrix} \epsilon_1\epsilon_2 & \epsilon_1f_2 & f_1\epsilon_2 & f_1f_2 \\ \epsilon_1\bar{\epsilon}_2 & \epsilon_1\bar{f}_2 & f_1\bar{\epsilon}_2 & f_1\bar{f}_2 \\ \bar{\epsilon}_1\epsilon_2 & \bar{\epsilon}_1f_2 & \bar{f}_1\epsilon_2 & \bar{f}_1f_2 \\ \bar{\epsilon}_1\bar{\epsilon}_2 & \bar{\epsilon}_1\bar{f}_2 & \bar{f}_1\bar{\epsilon}_2 & \bar{f}_1\bar{f}_2 \end{pmatrix}^{-1} = \frac{1}{d} \begin{pmatrix} \bar{f}_1\bar{f}_2 & -\bar{f}_1f_2 & -f_1\bar{f}_2 & f_1f_2 \\ -\bar{f}_1\bar{\epsilon}_2 & \bar{f}_1\epsilon_2 & f_1\bar{\epsilon}_2 & -f_1\epsilon_2 \\ -\bar{\epsilon}_1\bar{f}_2 & \bar{\epsilon}_1f_2 & \epsilon_1\bar{f}_2 & -\epsilon_1f_2 \\ \bar{\epsilon}_1\bar{\epsilon}_2 & -\bar{\epsilon}_1\epsilon_2 & -\epsilon_1\bar{\epsilon}_2 & \epsilon_1\epsilon_2 \end{pmatrix} \quad (5.47)$$

Equation 5.43 becomes

$$\begin{aligned}
N'_{TT} &= \left(\begin{array}{cccc} \epsilon_1 \epsilon_2 & \epsilon_1 f_2 & f_1 \epsilon_2 & f_1 f_2 \end{array} \right) \left(\begin{array}{cccc} 0 & 0 & 0 & 0 \\ 0 & 1 & 0 & 0 \\ 0 & 0 & 1 & 0 \\ 0 & 0 & 0 & 1 \end{array} \right) \frac{1}{d} \left(\begin{array}{cccc} \bar{f}_1 \bar{f}_2 & -\bar{f}_1 f_2 & -f_1 \bar{f}_2 & f_1 f_2 \\ -\bar{f}_1 \bar{\epsilon}_2 & \bar{f}_1 \epsilon_2 & f_1 \bar{\epsilon}_2 & -f_1 \epsilon_2 \\ -\bar{\epsilon}_1 \bar{f}_2 & \bar{\epsilon}_1 f_2 & \epsilon_1 \bar{f}_2 & -\epsilon_1 f_2 \\ \bar{\epsilon}_1 \bar{\epsilon}_2 & -\bar{\epsilon}_1 \epsilon_2 & -\epsilon_1 \bar{\epsilon}_2 & \epsilon_1 \epsilon_2 \end{array} \right) \left(\begin{array}{c} N_{TT} \\ N_{TL} \\ N_{LT} \\ N_{LL} \end{array} \right) \\
&= \frac{1}{d} \left(\begin{array}{cccc} \epsilon_1 \epsilon_2 & \epsilon_1 f_2 & f_1 \epsilon_2 & f_1 f_2 \end{array} \right) \left(\begin{array}{cccc} 0 & 0 & 0 & 0 \\ -\bar{f}_1 \bar{\epsilon}_2 & \bar{f}_1 \epsilon_2 & f_1 \bar{\epsilon}_2 & -f_1 \epsilon_2 \\ -\bar{\epsilon}_1 \bar{f}_2 & \bar{\epsilon}_1 f_2 & \epsilon_1 \bar{f}_2 & -\epsilon_1 f_2 \\ \bar{\epsilon}_1 \bar{\epsilon}_2 & -\bar{\epsilon}_1 \epsilon_2 & -\epsilon_1 \bar{\epsilon}_2 & \epsilon_1 \epsilon_2 \end{array} \right) \left(\begin{array}{c} N_{TT} \\ N_{TL} \\ N_{LT} \\ N_{LL} \end{array} \right)
\end{aligned} \tag{5.48}$$

For a tight-tight pair,

$$\text{fake weight} = \frac{1}{d}(-\epsilon_1 \bar{f}_1 \bar{\epsilon}_2 f_2 - \bar{\epsilon}_1 f_1 \epsilon_2 \bar{f}_2 + \bar{\epsilon}_1 f_1 \bar{\epsilon}_2 f_2) \tag{5.49}$$

For a tight-loose pair,

$$\begin{aligned}
\text{fake weight} &= \frac{1}{d}(\epsilon_1 \bar{f}_1 \epsilon_2 f_2 + \bar{\epsilon}_1 f_1 \epsilon_2 f_2 - \bar{\epsilon}_1 f_1 \epsilon_2 f_2) \\
&= \frac{\epsilon_1 \bar{f}_1 \epsilon_2 f_2}{d}
\end{aligned} \tag{5.50}$$

For a loose-tight pair,

$$\begin{aligned}
\text{fake weight} &= \frac{1}{d}(\epsilon_1 f_1 \bar{\epsilon}_2 f_2 + \epsilon_1 f_1 \epsilon_2 \bar{f}_2 - \epsilon_1 f_1 \bar{\epsilon}_2 f_2) \\
&= \frac{\epsilon_1 f_1 \epsilon_2 \bar{f}_2}{d}
\end{aligned} \tag{5.51}$$

For a loose-loose pair,

$$\begin{aligned}
\text{fake weight} &= \frac{1}{d}(-\epsilon_1 f_1 \epsilon_2 f_2 - \epsilon_1 f_1 \epsilon_2 f_2 + \epsilon_1 f_1 \epsilon_2 f_2) \\
&= -\frac{\epsilon_1 f_1 \epsilon_2 f_2}{d}
\end{aligned} \tag{5.52}$$

5.2.3 Measurement of real efficiencies

The real efficiencies ϵ_i are measured by the Z boson tag-and-probe method. This method is based on the fact that the Z boson will decay into two opposite-sign electrons or two muons, and the invariant mass of the two leptons is close to the mass of the Z boson (~ 91 GeV). By selecting two opposite-sign same-flavour leptons with the invariant mass $80 \text{ GeV} < m_{ll} < 100 \text{ GeV}$, these two leptons are likely to be real leptons. If one of the leptons is a signal lepton, which is called the tag lepton, another lepton, which is called the probe lepton, is very likely to be a

real lepton. By counting the total number of baseline leptons and signal leptons for the probe lepton, the real efficiencies ϵ can be measured. The counting was done on the data sample, and hence this a data-driven method.

$$\epsilon = \frac{N_{\text{signal}}^{\text{data}}}{N_{\text{baseline}}^{\text{data}}} \quad (5.53)$$

The selections for the control region used in the measurement of real efficiencies is, on top of the selections in section 3.2, as follows.

- The two leptons are two electrons or two muons.
- The electric charges of the two leptons are opposite sign.
- $80 \text{ GeV} < m_{ll} < 100 \text{ GeV}$

To increase the statistics, if the two leptons are both signal leptons, both leptons can be tag leptons. Hence, both leptons will be probe leptons, and it will be double-counted.

The binning for p_T and $|\eta|$ is shown in table 5.2.

Variable	Boundary of the bins
p_T (GeV)	20, 30, 40, 50, 60, 70, 80, 90, 100, 200
$ \eta $ (For electrons)	0, 0.8, 1.37, 1.52, 2.01, 2.47
$ \eta $ (For muons)	0, 0.6, 1.2, 1.8, 2.5

Table 5.2: Binning in p_T and $|\eta|$ for real efficiencies.

The results for the real efficiencies are shown in figure 5.9.

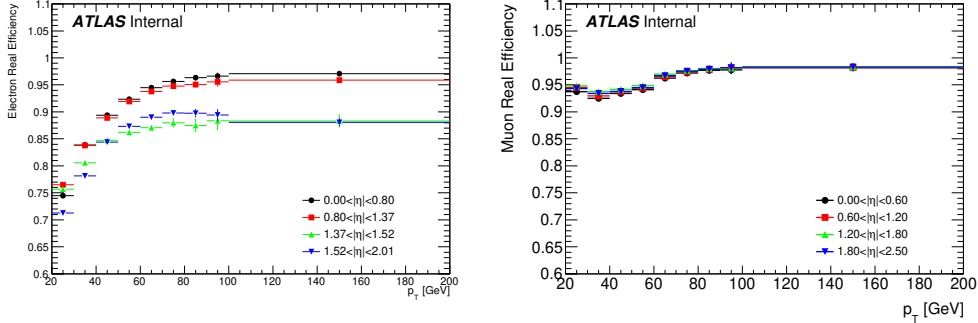


Figure 5.9: The real efficiencies for electrons (left) and muons (right). Only statistical uncertainties are considered.

5.2.4 Measurement of fake efficiencies

The fake efficiencies are measured by the tag-and-probe method, similar to the real efficiencies. On top of the selections in section 3.2, two different control regions are defined for electron and muon respectively. The control regions are needed to have rich heavy-flavor fakes, by the requiring at least one b-jet. The selections for the control regions are summarized as follows:

- For electron fake efficiencies, one lepton is a muon and another is an electron.
For muons fake efficiencies, the two leptons are both muons.
- The electric charges of the two leptons are same sign.
- There is at least 1 b-jet.

In both control regions, the tag leptons must be a signal muon with $p_T > 40$ GeV, and hence it is very likely to be a real lepton. The probe lepton is very likely to a fake lepton from heavy-flavor jets, because the two leptons are same-sign and one of the leptons is real lepton. By counting the number of the baseline and signal probe leptons, the fake efficiencies can be estimated. This counting was done on the data samples. In order to have a better estimation and ensure that the probe leptons are coming from fake leptons, the number of the baseline and signal probe leptons from data need to be subtracted by the number of real leptons, estimated by the MC sample.

$$f = \frac{N_{\text{signal}}}{N_{\text{baseline}}} \quad (5.4)$$

$$= \frac{N_{\text{signal}}^{\text{data}} - N_{\text{signal}}^{\text{MC, real}}}{N_{\text{baseline}}^{\text{data}} - N_{\text{baseline}}^{\text{MC, real}}} \quad (5.5)$$

The identification of the real leptons in the MC samples is using the truth information (ParticleType = IsoElectron/IsoMuon) by using the package `MCTruthClassifier`. It will classify the reconstructed lepton into different types of truth particle. The origin of the reconstructed lepton can then be known.

The binning for p_T and $|\eta|$ is shown in table 5.3.

The results for the fake efficiencies are shown in figure 5.10.

5.2.5 Validation for the fake lepton background

In order to validate the fake lepton background, the fake lepton background, together with other backgrounds, are compared with the data in a validation

Variable	Boundary of the bins
	Electrons
p_T (GeV)	25, 35, 45, 120, 200
$ \eta $	0, 1.37, 1.52, 2.47
	Muons
p_T (GeV)	25, 30, 45, 120, 200
$ \eta $	0, 1.37, 1.52, 2.4

Table 5.3: Binning in p_T and $|\eta|$ for fake efficiencies.

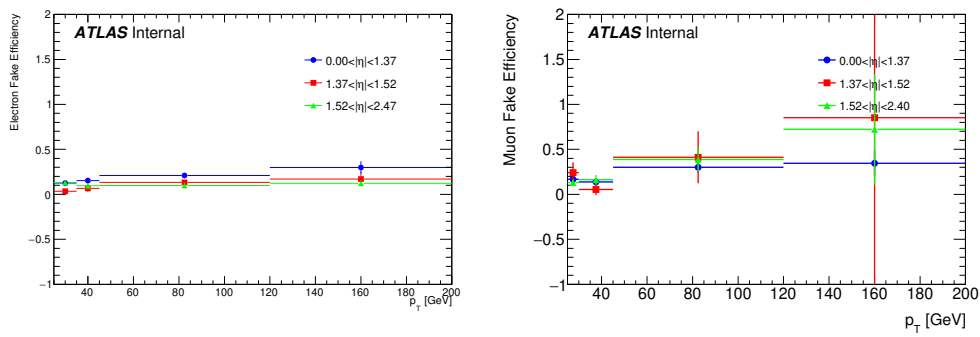


Figure 5.10: The fake efficiencies for electrons (left) and muons (right). Only statistical uncertainties are considered.

region. The validation region is expected to have small contribution from signal. The validation region is defined as follows, on top of the selections in section 3.2.

- The two leptons are signal leptons.
- The two leptons are same-sign.
- b-jets veto: $n_{\text{b-jets}} = 0$, to suppress top background.
- At least one signal jet: $n_{\text{jets}} \geq 1$
- Z veto: $|m_{ll} - m_Z| > 10 \text{ GeV}$, to suppress Z+jets background.
- $E_T^{\text{miss}} > 30 \text{ GeV}$
- $m_{\text{eff}} > 200 \text{ GeV}$

To ensure that the contribution from signal is small, the percentages of the signal contribution are checked in figure 5.11, and they are below 3%. Also, in order to make sure that there is a substantial contribution from fake lepton background, the percentages of different backgrounds are checked in table 5.4. The validation region is split into 3 channels: electron-electron, muon-muon and electron-muon channel. Their fake contributions are 66%, 24% and 49% respectively.

The backgrounds and the data are compared for several variables in the 3 channels, shown in figure 5.12, 5.13 and 5.14 respectively. The agreements between the backgrounds and the data are good within the uncertainties.

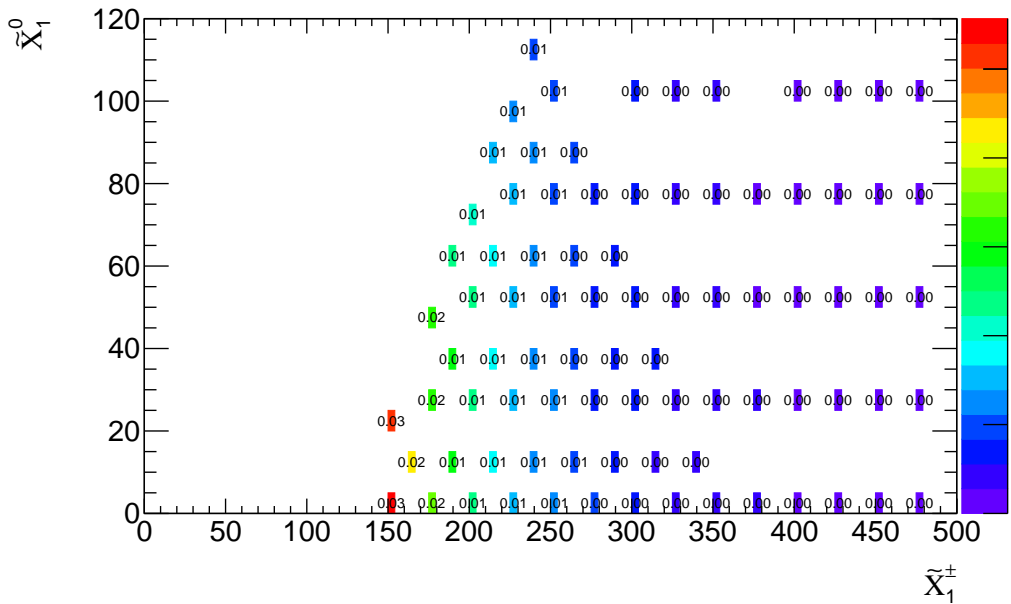


Figure 5.11: Signal contributions in the validation region are shown for different mass points.

	ee channel	$\mu\mu$ channel	e μ channel
Fakes	65.8% (710.3)	23.8% (85.7)	49.4% (576.4)
Charge-flip	10.3% (111.6)	0.0% (0.0)	1.1% (13.6)
WZ	17.4% (188.5)	54.0% (194.5)	36.2% (422.0)
ZZ	0.7% (1.6)	0.5% (1.8)	0.3% (3.5)
WW	3.9% (42.3)	13.8% (50.0)	7.9% (92.4)
Rare	1.5% (16.9)	4.5% (16.3)	2.0% (23.5)
ttV	0.6% (8.0)	2.4% (8.8)	1.5% (17.3)
Total BG	1079	357.1	1149
Data	936	360	1166

Table 5.4: Percentages of different backgrounds in the Validation region. The numbers in brackets are the yields.

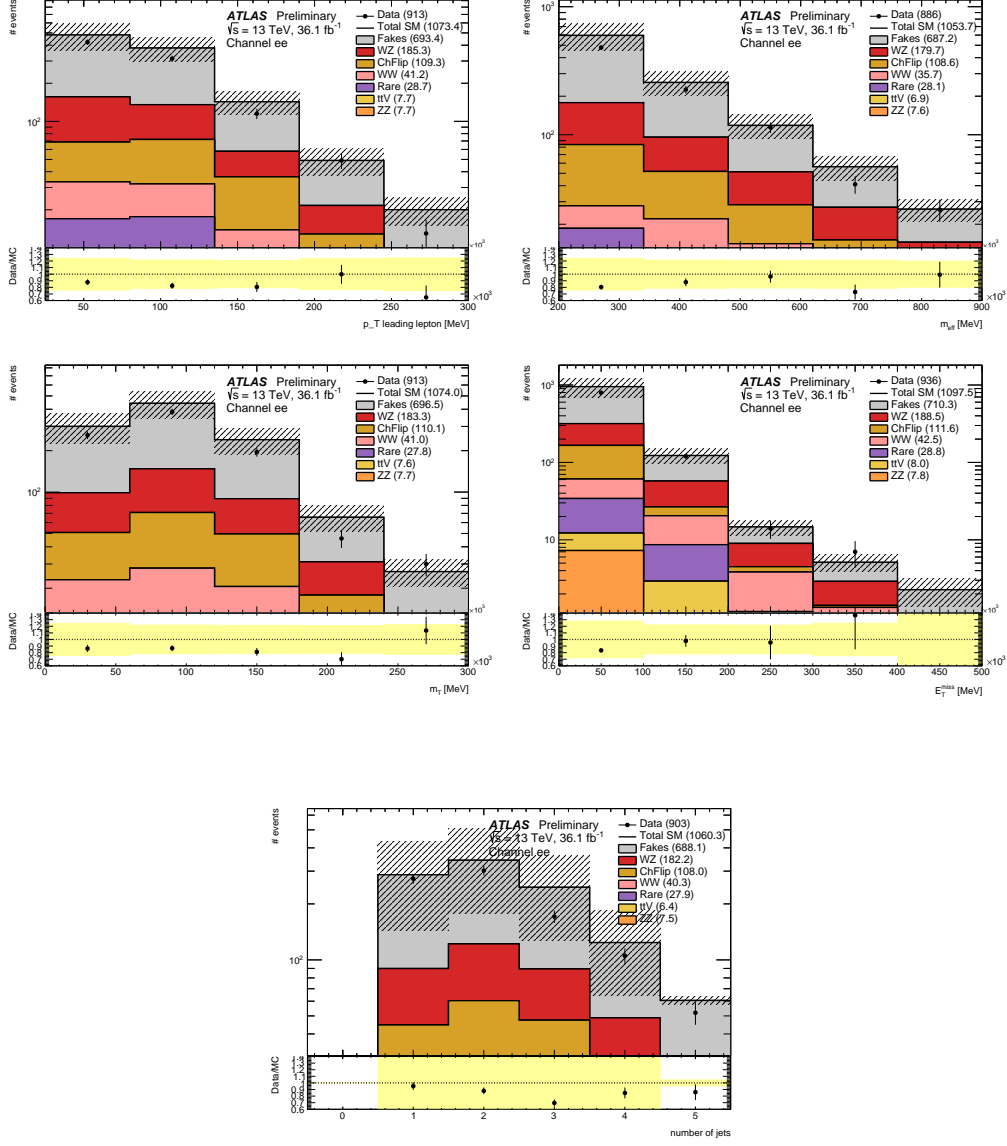


Figure 5.12: Distribution of the leading lepton p_T , m_{eff} , m_T , E_T^{miss} and n_{jets} in the electron-electron channel. The ratio of data to background is shown in the lower plot. The error bar includes all the systematic uncertainties except for the theoretical uncertainties.

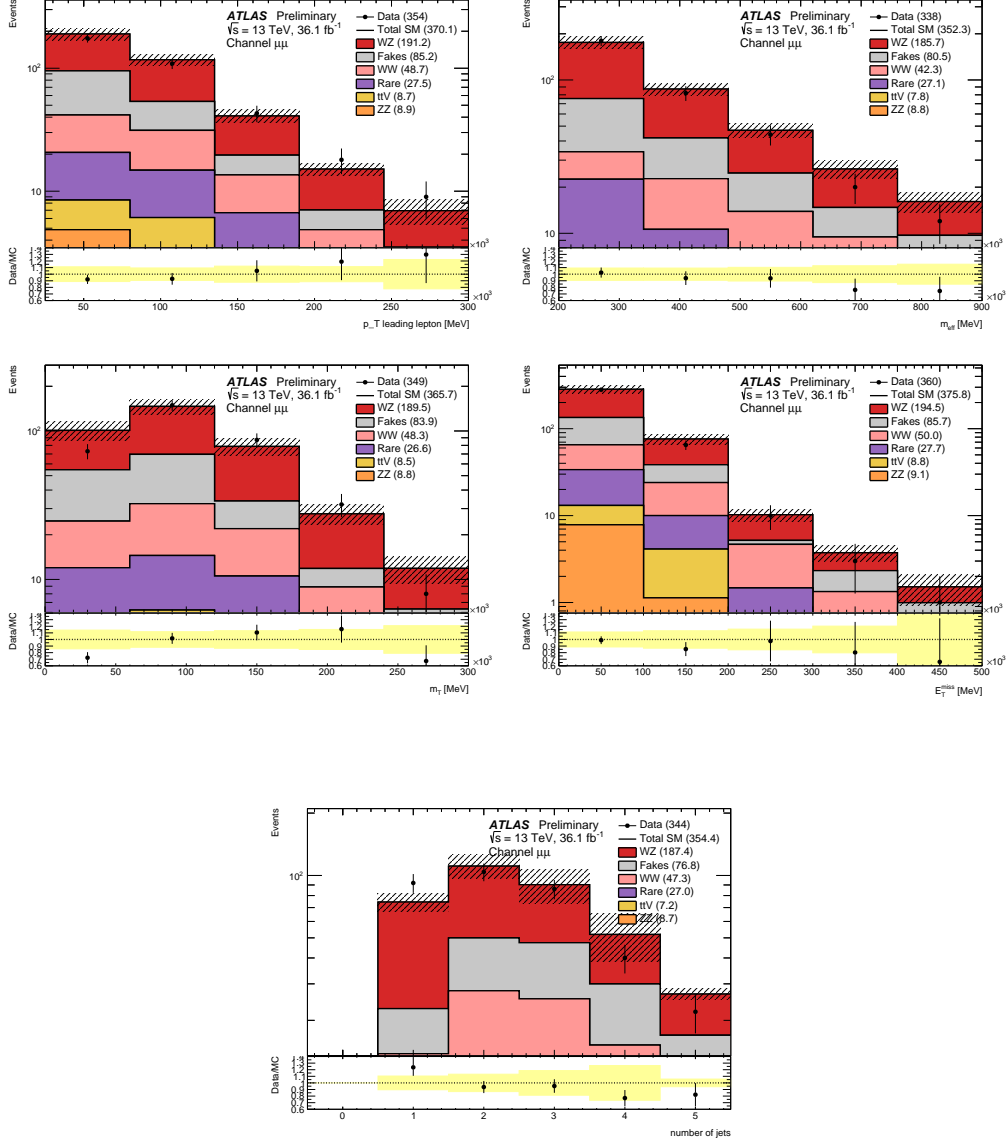


Figure 5.13: Distribution of the leading lepton p_T , m_{eff} , m_T , E_T^{miss} and n_{jets} in the muon-muon channel. The ratio of data to background is shown in the lower plot. The error bar includes all the systematic uncertainties except for the theoretical uncertainties.

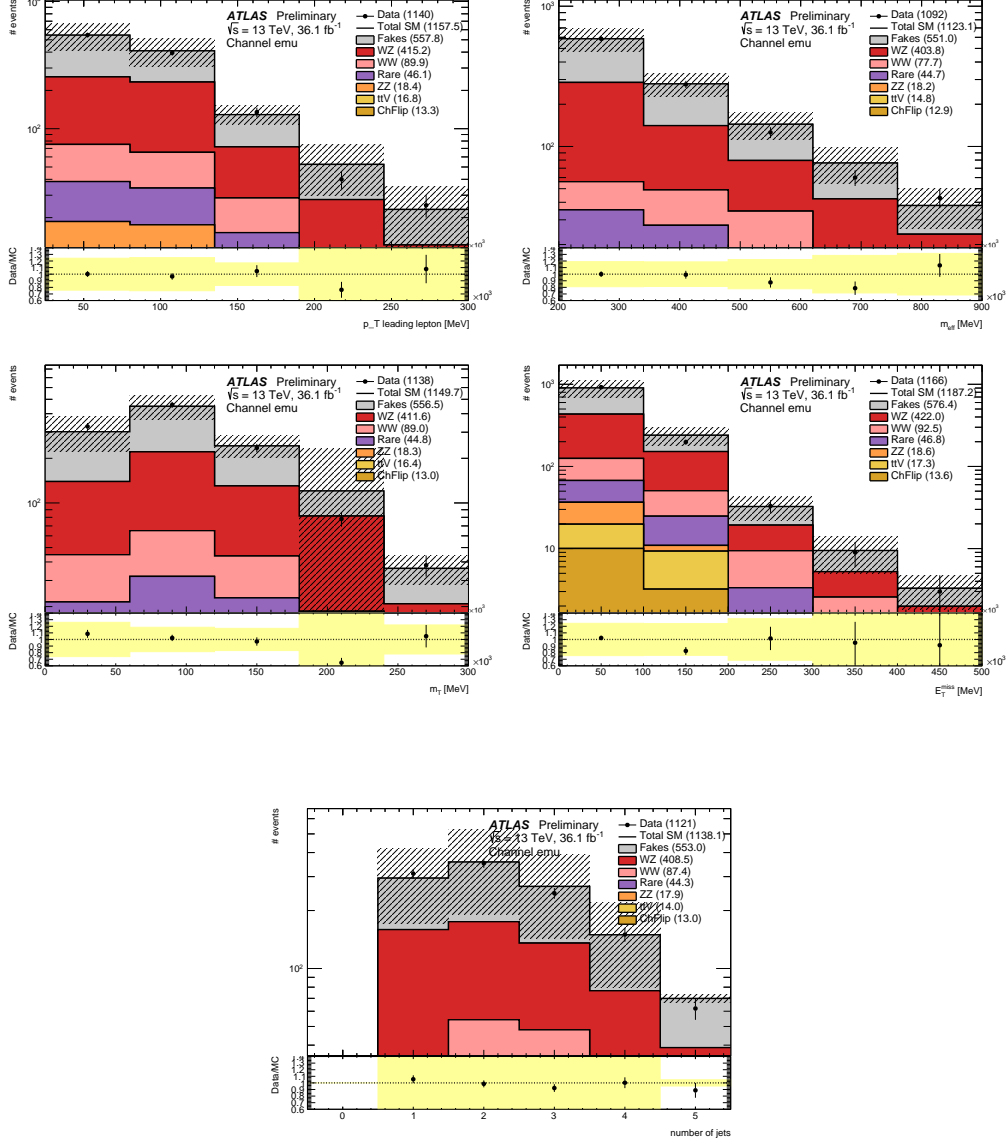


Figure 5.14: Distribution of the leading lepton p_T , m_{eff} , m_T , E_T^{miss} and n_{jets} in the electron-muon channel. The ratio of data to background is shown in the lower plot. The error bar includes all the systematic uncertainties except for the theoretical uncertainties.

Chapter 6

Validation regions

In order to ensure the estimations of the backgrounds have good modelling, two validation regions (VRjet1 and VRjet23) are defined for the corresponding two signal regions (SRjet1 and SRjet23), to compare the backgrounds and the data. There are three requirements for the validation regions:

- The signal contribution is small.
- The validation region is orthogonal to the corresponding signal region.
- The background composition is similar to the corresponding signal region.

The definitions of the two validation regions are summarized in table 6.1.

Cut	VRjet1	VRjet23
n_{jets}	1	[2, 3]
$\Delta\eta_{ll}$	< 1.5	—
E_T^{miss} [GeV]	[70, 100]	> 100
m_T [GeV]	> 140	[65, 120]
m_{eff} [GeV]	—	> 240
$m_{l(j)}$ [GeV]	> 130	> 130
m_{T2} [GeV]	—	—

Table 6.1: The definition of the two validation regions, on top of the pre-selections in section 4.2.1. The values in red colour represent the changes with respect to the cuts in the signal regions.

For the VRjet1, the validation region is obtained by reversing the E_T^{miss} cut and applying a lower cut on it. This can ensure that the validation region is

orthogonal to SRjet1. The lower cut of E_T^{miss} is optimized to 70 GeV, to have a similar background composition with SRjet1. The direction of the m_{lj} is reversed and relaxed, in order to reduce the signal contribution and increase the statistics. The cuts of m_{eff} and m_{T2} are also removed to increase the statistics.

For the VRjet23, the validation region is obtained by reversing the m_T cut and applying a lower cut on it. Similar to VRjet1, this can ensure that the validation region is orthogonal to SRjet23, and the lower cut can be optimized to have a similar background composition. The lower cut of m_T is optimized to 65 GeV. The direction of the m_{jjj} is reversed to reduce the signal contribution. To increase the statistics, the m_{T2} cut is removed.

The percentages of signal contribution for different mass points are shown in figure 6.1. The signal contribution is below 12% and 10% for VRjet1 and VRjet23 respectively. Figure 6.2 and 6.3 show the background composition for the validation regions and their corresponding signal regions. The background compositions of the validation regions are similar, compared with their corresponding signal regions. Table 6.2 shows the expected number of events in each background and the observed number of events in data. The comparisons of some variable distributions between the background and the data are also shown in figure 6.4 and 6.5 for VRjet1 and VRjet23 respectively. The estimated background and the data agree with each other within the uncertainties.

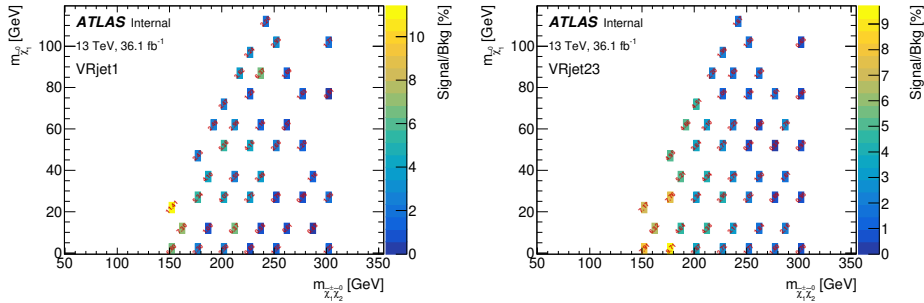


Figure 6.1: Percentages of signal contribution are shown for the VRjet1 (left) and VRjet23 (right).

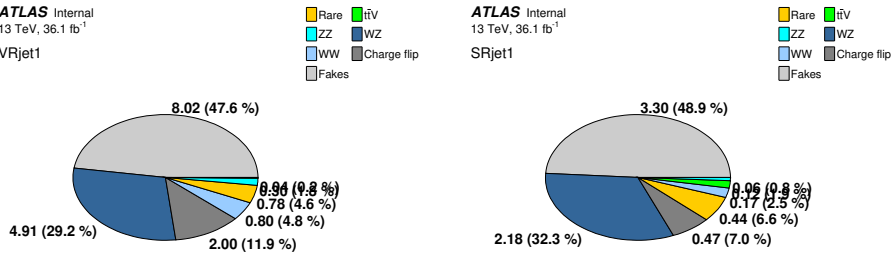


Figure 6.2: Background composition for the VRjet1 (left) and SRjet1 (right).

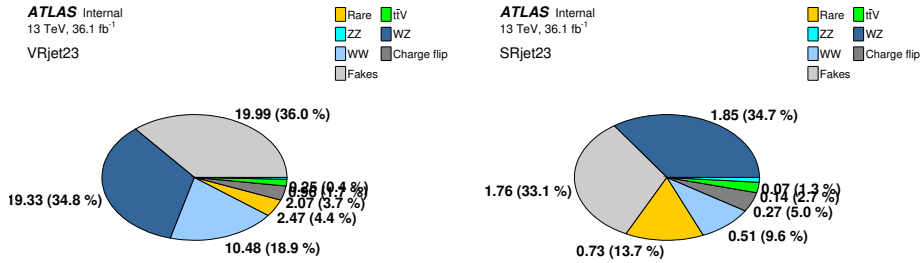


Figure 6.3: Background composition for the VRjet23 (left) and SRjet23 (right).

Process	VRjet1	VRjet23
Rare	$0.775 \pm 0.389^{+0.661}_{-0.362}$	$2.469 \pm 0.674^{+0.998}_{-0.899}$
$t\bar{t}V$	$0.039 \pm 0.013^{+0.018}_{-0.012}$	$0.959 \pm 0.082^{+0.152}_{-0.146}$
ZZ	$0.298 \pm 0.060^{+0.089}_{-0.063}$	$0.247 \pm 0.045^{+0.113}_{-0.047}$
WZ	$4.909 \pm 0.530^{+0.960}_{-0.899}$	$19.325 \pm 0.643^{+4.393}_{-4.346}$
WW	$0.801 \pm 0.051^{+0.123}_{-0.060}$	$10.477 \pm 0.176^{+0.796}_{-0.726}$
Charge flip	$1.997 \pm 0.128^{+0.260}_{-0.260}$	$2.065 \pm 0.085^{+0.166}_{-0.166}$
Fakes	$8.021 \pm 1.390^{+5.806}_{-5.806}$	$19.990 \pm 2.013^{+13.461}_{-13.461}$
Total BG	$16.839 \pm 1.545^{+5.915}_{-5.912}$	$55.534 \pm 2.228^{+14.396}_{-14.332}$
Data	17	54

Table 6.2: The expected number of background events and the observed number of data events for the VRjet1 (the second column) and VRjet23 (the third column). The uncertainties include the statistical and systematic uncertainties.

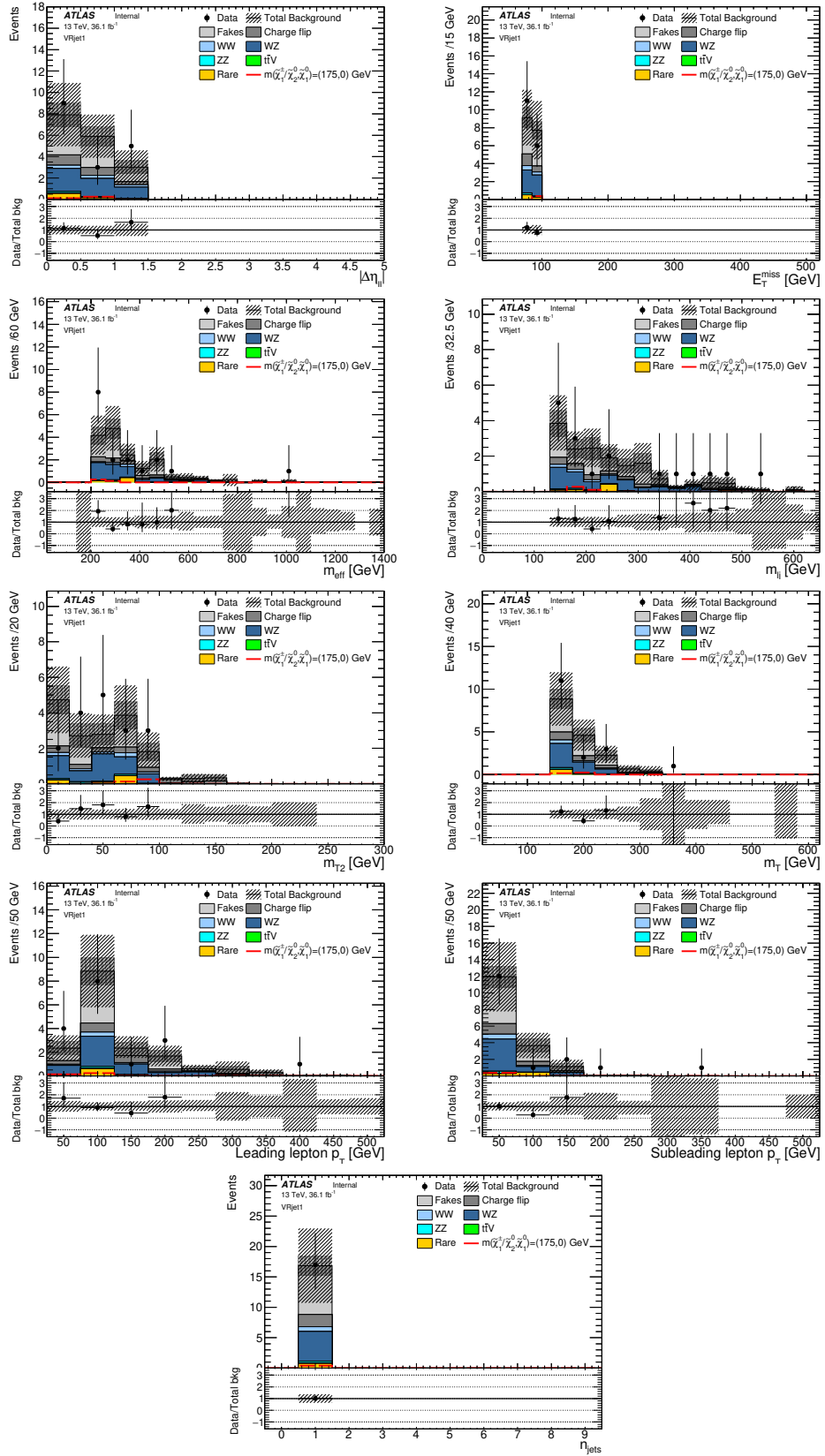


Figure 6.4: Distributions of some variables in the VRjet1 for the background estimation and the data are shown. A signal of a mass point $(m_{\tilde{\chi}_1^\pm, \tilde{\chi}_2^0}, m_{\tilde{\chi}_1^0}) = (175,0)$ GeV is also shown. The internal shaded area refers to the statistical uncertainties, while the external shaded area refers to the total uncertainty.

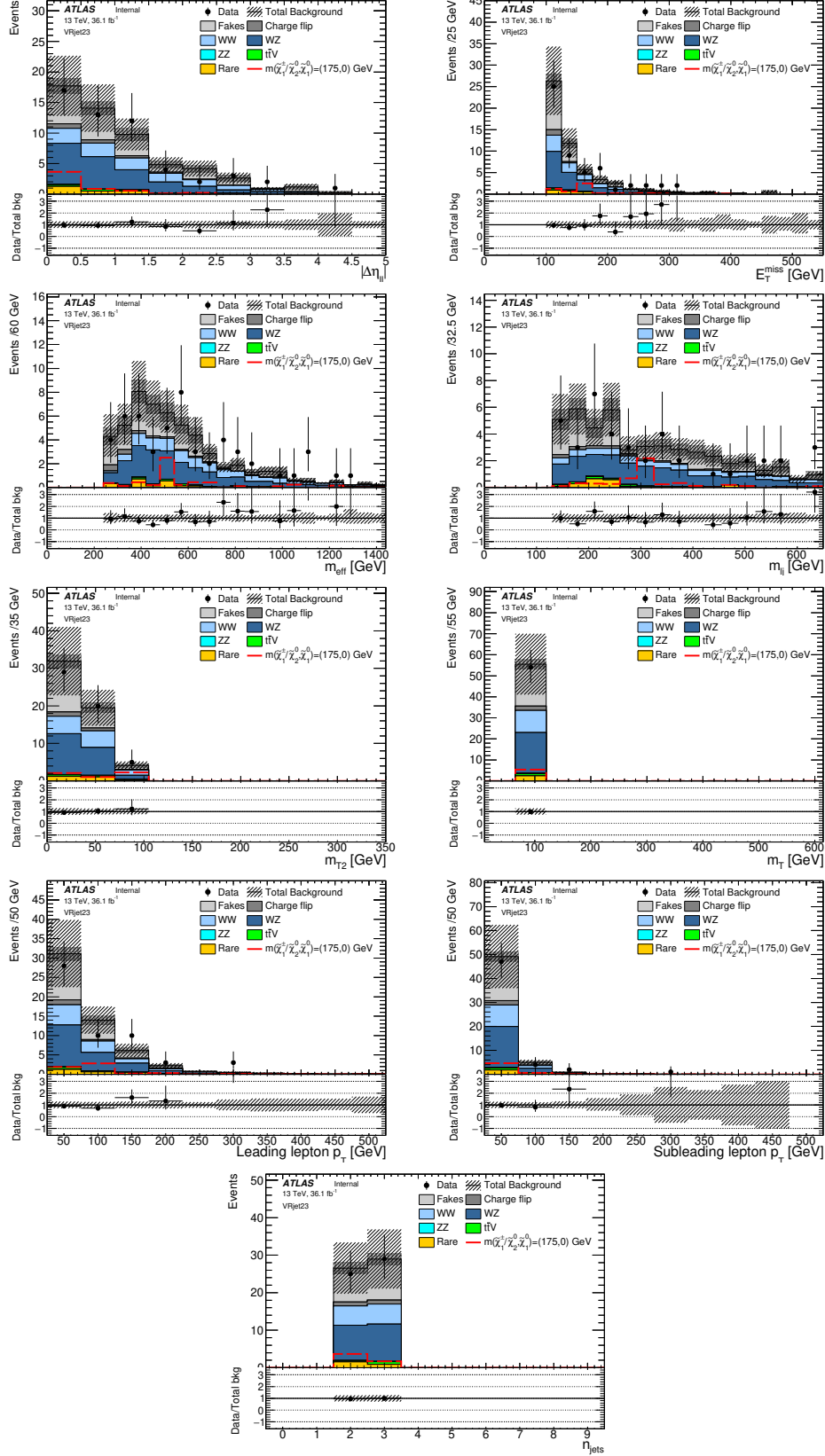


Figure 6.5: Distributions of some variables in the VRjet23 for the background estimation and the data are shown. A signal of a mass point $(m_{\tilde{\chi}_1^\pm, \tilde{\chi}_2^0}, m_{\tilde{\chi}_1^0}) = (175, 0)$ is also shown. The internal shaded area refers to the statistical uncertainties, while the external shaded area refers to the total uncertainty.

Chapter 7

Results

No any significant excess in signal is observed in the signal regions. Hence, the upper limit of the SUSY signal contribution is set and a exclusion limit on the masses of $m_{\tilde{\chi}_1^\pm, \tilde{\chi}_2^0}$ and $m_{\tilde{\chi}_1^0}$ is also set at the 95% confidence level, in a simplified supersymmetric model.

The observed events in data and the estimated background yields in the two signal regions are shown in table 7.1. The N-1 plots (i.e. all SR selections, but the variable on the x-asix, are applied) for the two signal regions are shown in figure 7.1 and 7.2. The observed data and the Standard Model expectations are agree with each other for all distributions within the uncertainties. No any significant excess in signal is observed.

	SRjet1	SRjet23
Observed events	2	8
Total background	6.7 ± 2.2	5.3 ± 1.6
Fakes events	3.3 ± 2.1	1.8 ± 1.5
MC exp. WZ events	2.2 ± 0.5	1.9 ± 0.6
MC exp. Rare events	0.44 ± 0.13	0.73 ± 0.17
MC exp. ttV events	0.12 ± 0.05	0.14 ± 0.05
MC exp. WW events	0.17 ± 0.03	0.51 ± 0.07
MC exp. ZZ events	0.06 ± 0.03	0.07 ± 0.04
Charge-flip events	0.47 ± 0.07	0.27 ± 0.03

Table 7.1: The observed events and the background yields in the signal regions are shown. The uncertainties include the statistical and systematic uncertainties.

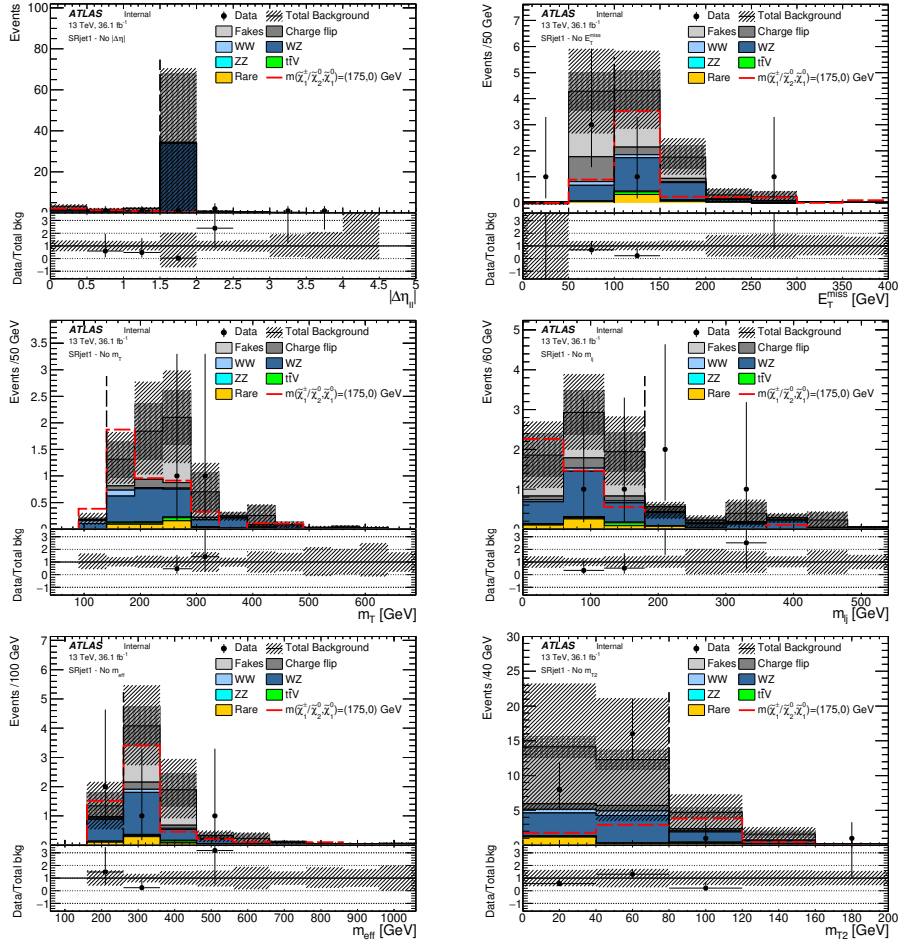


Figure 7.1: N-1 plots for different variable distributions in the SRjet1 for the background estimation and the data. The signal of the mass point with the highest significance ($m_{\tilde{\chi}_1^\pm, \tilde{\chi}_2^0, m_{\tilde{\chi}_1^0}} = (175,0)$) is shown by the red dashed line. The internal shaded area refers to the statistical uncertainties, while the external shaded area refers to the total uncertainty. The vertical dashed line shows the SR cut of that variable. The lower plot shows the ratio of data with respect to the total background.

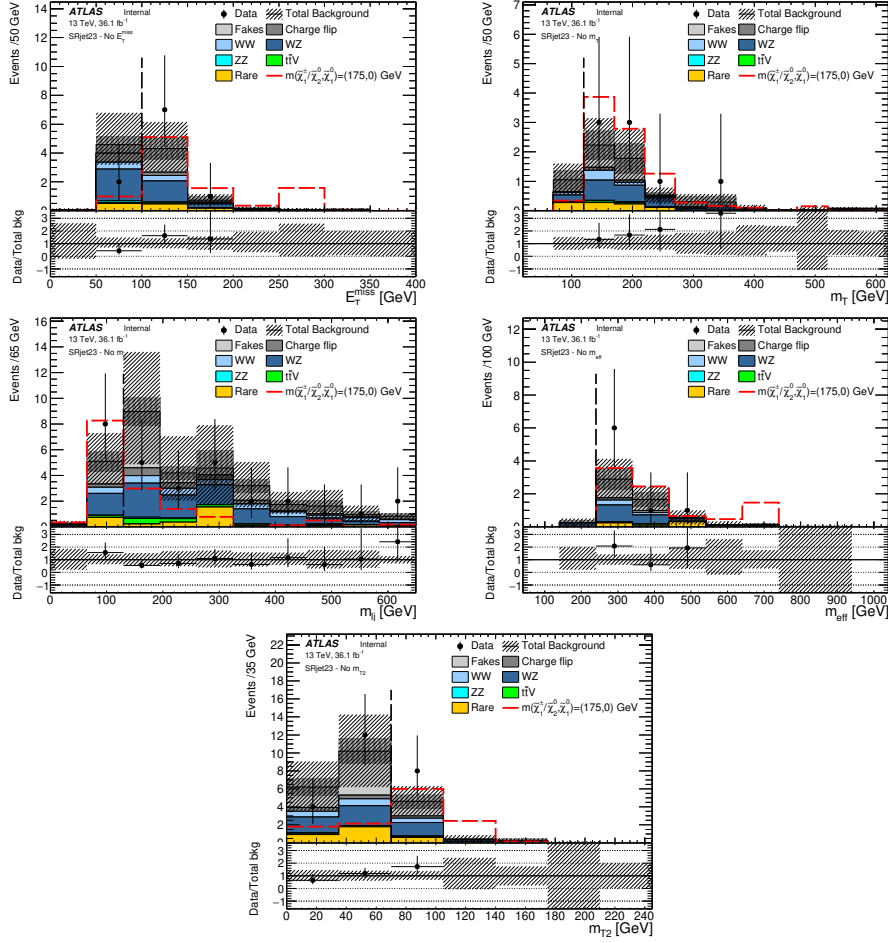


Figure 7.2: N-1 plots for different variable distributions in the SRjet23 for the background estimation and the data. The signal of the mass point with the highest significance ($m_{\tilde{\chi}_1^\pm, \tilde{\chi}_2^0, m_{\tilde{\chi}_1^0}} = (175,0)$) is shown by the red dashed line. The internal shaded area refers to the statistical uncertainties, while the external shaded area refers to the total uncertainty. The lower plot shows the ratio of data with respect to the total background.

Table 7.2 shows the results of the model-independent fit. This estimates the upper limits on the contributions from new physics, i.e. physics beyond the Standard Model (BSM). The second and third column show the upper limits on the observed (S_{obs}^{95}) and expected (S_{exp}^{95}) BSM events respectively, at 95% confidence level. The fluctuations of the upper limits of S_{exp}^{95} are also shown, with $\pm 1\sigma$ excursions on the expectation of the background events. The numbers in the first column are the upper limits on the observed visible cross-section σ_{vis} at 95% confidence level. With the normalization by the integrated luminosity of the data, the upper limit on the observed BSM events can be converted to a upper limit on a observed visible cross-section. The definition of the observed visible cross-section σ_{vis} is the product of a BSM cross-section, the acceptance and the selection efficiency of a BSM signal. The last column shows the discovery p -value (p_0). It is the probability that the Standard Model background by itself fluctuate to the observed number of events or higher.

	$\langle \sigma_{\text{vis}} \rangle_{\text{obs}}^{95} [\text{fb}]$	S_{obs}^{95}	S_{exp}^{95}	p_0
SRjet1	0.12	4.2	$6.1_{-1.5}^{+2.7}$	0.50
SRjet23	0.27	9.9	$6.6_{-1.1}^{+3.4}$	0.17

Table 7.2: From left to right: 95% confidence level upper limits on the visible cross section ($\langle \sigma_{\text{vis}} \rangle_{\text{obs}}^{95}$) and on the observed number of signal events (S_{obs}^{95}). The third column (S_{exp}^{95}) shows the 95% confidence level upper limit on the expected number of signal events, with $\pm 1\sigma$ excursions on the expectation of the background events. The last column shows the discovery p -value (p_0).

Figure 7.3 shows the expected and observed exclusion limits on the masses of $m_{\tilde{\chi}_1^\pm, \tilde{\chi}_2^0}$ and $m_{\tilde{\chi}_1^0}$ at the 95% confidence level. The exclusion limits means that the mass points inside the curve are excluded, but the mass points outside the curve are still possible. The exclusion limits are calculated by combining the two signal regions. Compared with other channels in Wh search, our same-sign channel is sensitive in the low $m_{\tilde{\chi}_1^\pm, \tilde{\chi}_2^0}$ region and the compressed region described in section 1.5. The exclusion limits for the masses of $\tilde{\chi}_1^\pm$ and $\tilde{\chi}_2^0$ are extended up to 245 GeV, while the exclusion limits for the mass of $\tilde{\chi}_1^0$ are extended up to 40 GeV.

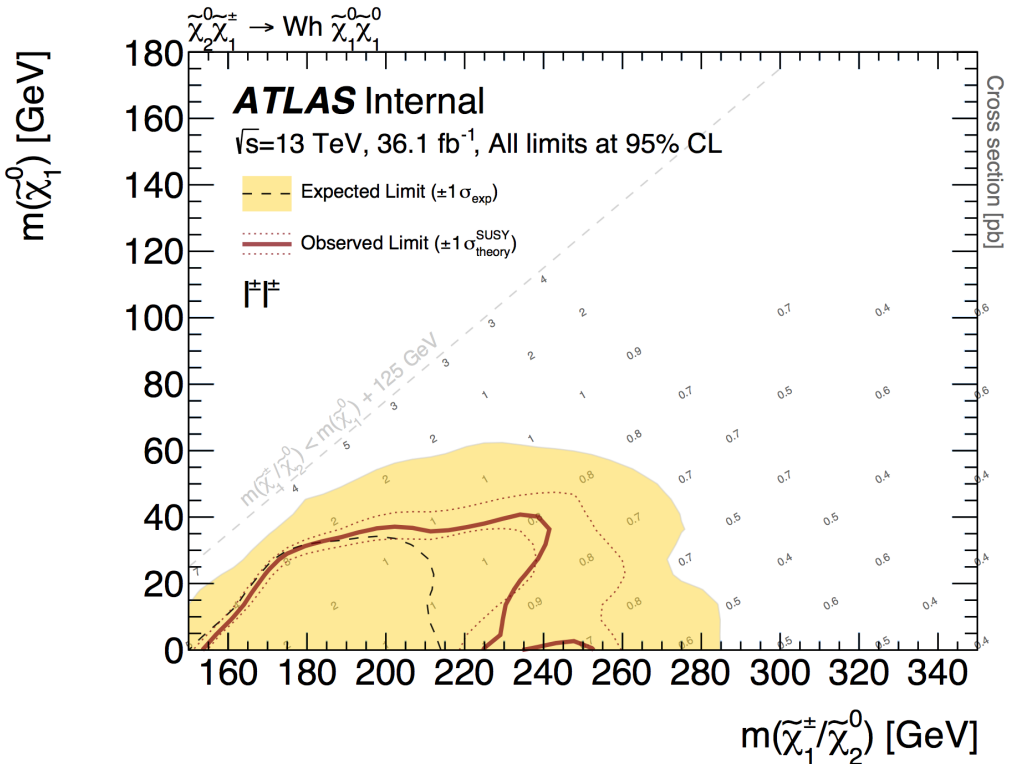


Figure 7.3: The expected and observed exclusion limits for the combined SRjet1 and SRjet23 are shown. Experimental and theoretical systematic uncertainties are applied to background and signal samples and illustrated by the yellow band and the red dotted contour lines respectively. The red dotted lines indicate the $\pm 1\sigma$ variation on the observed exclusion limit due to theoretical uncertainties on the signal cross-section.

Chapter 8

Conclusion

Results of a search for the electroweak pair production of a chargino and a neutralino ($p + p \rightarrow \tilde{\chi}_1^\pm + \tilde{\chi}_2^0$) are presented, with the Wh channel $\tilde{\chi}_1^\pm \rightarrow \tilde{\chi}_1^0 + W$ and $\tilde{\chi}_2^0 \rightarrow \tilde{\chi}_1^0 + h$, and the same-sign channel. The dominant background is the fake lepton background, and the dominant irreducible background is the diboson processes, especially the WZ processes. Two signal regions are defined and optimized for the compressed region where the mass difference between $\tilde{\chi}_1^\pm/\tilde{\chi}_2^0$ and $\tilde{\chi}_1^0$ is close to the Higgs mass 125 GeV. No significant deviations due to the signal are observed, but new exclusion limits for the masses $m_{\tilde{\chi}_1^\pm, \tilde{\chi}_2^0}$ and $m_{\tilde{\chi}_1^0}$ are set. The exclusion limits for the masses of $\tilde{\chi}_1^\pm$ and $\tilde{\chi}_2^0$ are extended up to 245 GeV, while the exclusion limits for the mass of $\tilde{\chi}_1^0$ are extended up to 40 GeV.

Appendix A

List of MC samples

A.1 List of data samples

The following Good Run Lists (GRL) are used.

- `data15_13TeV.periodAllYear_DetStatus-v79-repro20-02_DQDefects-00-02-02_PHYS_StandardGRL--All_Good_25ns.xml` for 2015 data.

- `data16_13TeV.periodAllYear_DetStatus-v89-pro21-01_DQDefects-00-02-04_PHYS_StandardGRL--All_Good_25ns.xml` for 2016 data.

The following is the list of data samples used.

```
data15_13TeV.periodD.physics_Main.PhysCont.DAOD_SUSY2.grp15_v02_p2950
data15_13TeV.periodE.physics_Main.PhysCont.DAOD_SUSY2.grp15_v02_p2950
data15_13TeV.periodF.physics_Main.PhysCont.DAOD_SUSY2.grp15_v02_p2950
data15_13TeV.periodG.physics_Main.PhysCont.DAOD_SUSY2.grp15_v02_p2950
data15_13TeV.periodH.physics_Main.PhysCont.DAOD_SUSY2.grp15_v02_p2950
data15_13TeV.periodJ.physics_Main.PhysCont.DAOD_SUSY2.grp15_v02_p2950
data16_13TeV.periodA.physics_Main.PhysCont.DAOD_SUSY2.grp16_v02_p2950
data16_13TeV.periodB.physics_Main.PhysCont.DAOD_SUSY2.grp16_v02_p2950
data16_13TeV.periodC.physics_Main.PhysCont.DAOD_SUSY2.grp16_v02_p2950
data16_13TeV.periodD.physics_Main.PhysCont.DAOD_SUSY2.grp16_v02_p2950
data16_13TeV.periodE.physics_Main.PhysCont.DAOD_SUSY2.grp16_v02_p2950
data16_13TeV.periodF.physics_Main.PhysCont.DAOD_SUSY2.grp16_v02_p2950
data16_13TeV.periodG.physics_Main.PhysCont.DAOD_SUSY2.grp16_v02_p2950
data16_13TeV.periodI.physics_Main.PhysCont.DAOD_SUSY2.grp16_v02_p2950
data16_13TeV.periodK.physics_Main.PhysCont.DAOD_SUSY2.grp16_v02_p2950
data16_13TeV.periodL.physics_Main.PhysCont.DAOD_SUSY2.grp16_v02_p2950
```

A.2 List of background MC samples

Dataset ID	Process	Tags	Cross section [pb]	k-factor	Generator efficiency	$\mathcal{L}_{\text{int}} [\text{fb}^{-1}]$
364156	Sherpa_221_NNPDF30NNLO_Wmmu_MAXHTPTV0_70_CVetoBVeto	e5340_s2726_r7772_r7676_p2949	19143.0000	0.97	0.824	1.616
364157	Sherpa_221_NNPDF30NNLO_Wmmu_MAXHTPTV0_70_CFilterBVeto	e5340_s2726_r7772_r7676_p2949	19121.0000	0.97	0.130	4.071
364158	Sherpa_221_NNPDF30NNLO_Wmmu_MAXHTPTV0_70_BFilter	e5340_s2726_r7772_r7676_p2949	19135.0000	0.97	0.044	21.032
364159	Sherpa_221_NNPDF30NNLO_Wmmu_MAXHTPTV0_70_CVetoBVeto	e5340_s2726_r7772_r7676_p2949	944.8500	0.97	0.675	23.912
364160	Sherpa_221_NNPDF30NNLO_Wmmu_MAXHTPTV70_140_CFilterBVeto	e5340_s2726_r7772_r7676_p2949	937.7800	0.97	0.235	46.173
364161	Sherpa_221_NNPDF30NNLO_Wmmu_MAXHTPTV70_140_BFilter	e5340_s2726_r7772_r7676_p2949	944.6300	0.97	0.076	283.269
364162	Sherpa_221_NNPDF30NNLO_Wmmu_MAXHTPTV140_280_CVetoBVeto	e5340_s2726_r7772_r7676_p2949	339.5400	0.97	0.626	47.919
364163	Sherpa_221_NNPDF30NNLO_Wmmu_MAXHTPTV140_280_CFilterBVeto	e5340_s2726_r7772_r7676_p2949	340.0600	0.97	0.289	77.568
364164	Sherpa_221_NNPDF30NNLO_Wmmu_MAXHTPTV140_280_BFilter	e5340_s2726_r7772_r7676_p2949	339.5400	0.97	0.109	686.449
364165	Sherpa_221_NNPDF30NNLO_Wmmu_MAXHTPTV280_500_CVetoBVeto	e5340_s2726_r7772_r7676_p2949	72.0670	0.97	0.546	129.289
364166	Sherpa_221_NNPDF30NNLO_Wmmu_MAXHTPTV280_500_CFilterBVeto	e5340_s2726_r7772_r7676_p2949	72.1980	0.97	0.317	133.034
364167	Sherpa_221_NNPDF30NNLO_Wmmu_MAXHTPTV280_500_BFilter	e5340_s2726_r7772_r7676_p2949	72.0450	0.97	0.133	317.464
364168	Sherpa_221_NNPDF30NNLO_Wmmu_MAXHTPTV500_1000	e5340_s2726_r7772_r7676_p2949	15.0100	0.97	1.000	405.866
364169	Sherpa_221_NNPDF30NNLO_Wmmu_MAXHTPTV1000_E_CMS	e5340_s2726_r7772_r7676_p2949	1.2344	0.97	1.000	3305.737
364170	Sherpa_221_NNPDF30NNLO_Wenu_MAXHTPTV0_70_CVetoBVeto	e5340_s2726_r7772_r7676_p2949	19127.0000	0.97	0.824	1.617
364171	Sherpa_221_NNPDF30NNLO_Wenu_MAXHTPTV0_70_CFilterBVeto	e5340_s2726_r7772_r7676_p2949	19130.0000	0.97	0.130	4.074
364172	Sherpa_221_NNPDF30NNLO_Wenu_MAXHTPTV0_70_BFilter	e5340_s2726_r7772_r7676_p2949	19135.0000	0.97	0.044	20.272
364173	Sherpa_221_NNPDF30NNLO_Wenu_MAXHTPTV70_140_CVetoBVeto	e5340_s2726_r7772_r7676_p2949	942.5800	0.97	0.669	23.973
364174	Sherpa_221_NNPDF30NNLO_Wenu_MAXHTPTV70_140_CFilterBVeto	e5340_s2726_r7772_r7676_p2949	945.6700	0.97	0.228	46.963
364175	Sherpa_221_NNPDF30NNLO_Wenu_MAXHTPTV70_140_BFilter	e5340_s2726_r7772_r7676_p2949	945.1500	0.97	0.103	103.368
364176	Sherpa_221_NNPDF30NNLO_Wenu_MAXHTPTV140_280_CVetoBVeto	e5340_s2726_r7772_r7676_p2949	339.8100	0.97	0.597	50.200
364177	Sherpa_221_NNPDF30NNLO_Wenu_MAXHTPTV140_280_CFilterBVeto	e5340_s2726_r7772_r7676_p2949	339.8700	0.97	0.290	77.584
364178	Sherpa_221_NNPDF30NNLO_Wenu_MAXHTPTV140_280_BFilter	e5340_s2726_r7772_r7676_p2949	339.4800	0.97	0.109	687.518
364179	Sherpa_221_NNPDF30NNLO_Wenu_MAXHTPTV280_500_CVetoBVeto	e5340_s2726_r7772_r7676_p2949	72.0840	0.97	0.544	129.323
364180	Sherpa_221_NNPDF30NNLO_Wenu_MAXHTPTV280_500_CFilterBVeto	e5340_s2726_r7772_r7676_p2949	72.1280	0.97	0.317	133.693
364181	Sherpa_221_NNPDF30NNLO_Wenu_MAXHTPTV280_500_BFilter	e5340_s2726_r7772_r7676_p2949	72.1130	0.97	0.134	315.726
364182	Sherpa_221_NNPDF30NNLO_Wenu_MAXHTPTV500_1000	e5340_s2726_r7772_r7676_p2949	15.2240	0.97	1.000	400.587
364183	Sherpa_221_NNPDF30NNLO_Wenu_MAXHTPTV1000_E_CMS	e5340_s2726_r7772_r7676_p2949	1.2334	0.97	1.000	3298.389
364184	Sherpa_221_NNPDF30NNLO_Wtaunu_MAXHTPTV0_70_CVetoBVeto	e5340_s2726_r7772_r7676_p2949	19152.0000	0.97	0.825	1.617
364185	Sherpa_221_NNPDF30NNLO_Wtaunu_MAXHTPTV0_70_CFilterBVeto	e5340_s2726_r7772_r7676_p2949	19153.0000	0.97	0.129	4.105
364186	Sherpa_221_NNPDF30NNLO_Wtaunu_MAXHTPTV0_70_BFilter	e5340_s2726_r7772_r7676_p2949	19163.0000	0.97	0.045	20.834
364187	Sherpa_221_NNPDF30NNLO_Wtaunu_MAXHTPTV70_140_CVetoBVeto	e5340_s2726_r7772_r7676_p2949	947.6500	0.97	0.674	23.903
364188	Sherpa_221_NNPDF30NNLO_Wtaunu_MAXHTPTV70_140_CFilterBVeto	e5340_s2726_r7772_r7676_p2949	946.7300	0.97	0.222	48.307
364189	Sherpa_221_NNPDF30NNLO_Wtaunu_MAXHTPTV70_140_BFilter	e5340_s2726_r7772_r7676_p2949	943.3000	0.97	0.104	103.602
364190	Sherpa_221_NNPDF30NNLO_Wtaunu_MAXHTPTV140_280_CVetoBVeto	e5340_s2726_r7772_r7676_p2949	339.3600	0.97	0.596	50.427
364191	Sherpa_221_NNPDF30NNLO_Wtaunu_MAXHTPTV140_280_CFilterBVeto	e5340_s2726_r7772_r7676_p2949	339.6300	0.97	0.290	76.903
364192	Sherpa_221_NNPDF30NNLO_Wtaunu_MAXHTPTV140_280_BFilter	e5340_s2726_r7772_r7676_p2949	339.5400	0.97	0.118	632.798
364193	Sherpa_221_NNPDF30NNLO_Wtaunu_MAXHTPTV280_500_CVetoBVeto	e5340_s2726_r7772_r7676_p2949	72.0650	0.92	0.546	136.270
364194	Sherpa_221_NNPDF30NNLO_Wtaunu_MAXHTPTV280_500_CFilterBVeto	e5340_s2726_r7772_r7676_p2949	71.9760	0.97	0.316	133.773
364195	Sherpa_221_NNPDF30NNLO_Wtaunu_MAXHTPTV280_500_BFilter	e5340_s2726_r7772_r7676_p2949	72.0260	0.97	0.134	314.868
364196	Sherpa_221_NNPDF30NNLO_Wtaunu_MAXHTPTV500_1000	e5340_s2726_r7772_r7676_p2949	15.0460	0.97	1.000	407.258
364197	Sherpa_221_NNPDF30NNLO_Wtaunu_MAXHTPTV1000_E_CMS	e5340_s2726_r7772_r7676_p2949	1.2339	0.97	1.000	3296.218

Table A.1: List of simulated W+jets processes

Dataset ID	Process	Tags	Cross section [pb]	k-factor	Generator efficiency	$\mathcal{L}_{int}[\text{fb}^{-1}]$
364100	Sherpa_221_NNPDF30NNLO_Zmumu_MAXHTPTV0_70_CVetoBVeto	e5271_s2726_r7772_r7676_p2949	1983.0000	0.98	0.822	4.964
364101	Sherpa_221_NNPDF30NNLO_Zmumu_MAXHTPTV0_70_CFilterBVeto	e5271_s2726_r7772_r7676_p2949	1978.4000	0.98	0.113	22.540
364102	Sherpa_221_NNPDF30NNLO_Zmumu_MAXHTPTV0_70_BFilter	e5271_s2726_r7772_r7676_p2949	1982.2000	0.98	0.064	63.719
364103	Sherpa_221_NNPDF30NNLO_Zmumu_MAXHTPTV70_140_CVetoBVeto	e5271_s2726_r7772_r7676_p2949	108.9200	0.98	0.689	80.890
364104	Sherpa_221_NNPDF30NNLO_Zmumu_MAXHTPTV70_140_CFilterBVeto	e5271_s2726_r7772_r7676_p2949	109.4200	0.98	0.186	99.279
364105	Sherpa_221_NNPDF30NNLO_Zmumu_MAXHTPTV70_140_BFilter	e5271_s2726_r7772_r7676_p2949	108.9100	0.98	0.114	488.459
364106	Sherpa_221_NNPDF30NNLO_Zmumu_MAXHTPTV140_280_CVetoBVeto	e5271_s2726_r7772_r7676_p2949	39.8780	0.98	0.609	208.736
364107	Sherpa_221_NNPDF30NNLO_Zmumu_MAXHTPTV140_280_CFilterBVeto	e5271_s2726_r7772_r7676_p2949	39.7950	0.98	0.233	326.653
364108	Sherpa_221_NNPDF30NNLO_Zmumu_MAXHTPTV140_280_BFilter	e5271_s2726_r7772_r7676_p2949	39.9080	0.98	0.146	2169.169
364109	Sherpa_221_NNPDF30NNLO_Zmumu_MAXHTPTV280_500_CVetoBVeto	e5271_s2726_r7772_r7676_p2949	8.5375	0.98	0.559	423.925
364110	Sherpa_221_NNPDF30NNLO_Zmumu_MAXHTPTV280_500_CFilterBVeto	e5271_s2726_r7772_r7676_p2949	8.5403	0.98	0.265	446.324
364111	Sherpa_221_NNPDF30NNLO_Zmumu_MAXHTPTV280_500_BFilter	e5271_s2726_r7772_r7676_p2949	8.4932	0.98	0.176	1355.672
364112	Sherpa_221_NNPDF30NNLO_Zmumu_MAXHTPTV500_1000	e5271_s2726_r7772_r7676_p2949	1.7881	0.98	1.000	1697.947
364113	Sherpa_221_NNPDF30NNLO_Zmumu_MAXHTPTV1000_E_CMS	e5271_s2726_r7772_r7676_p2949	0.1477	0.98	1.000	6860.515
364114	Sherpa_221_NNPDF30NNLO_Zee_MAXHTPTV70_140_CVetoBVeto	e5299_s2726_r7772_r7676_p2949	1981.8000	0.98	0.821	4.979
364115	Sherpa_221_NNPDF30NNLO_Zee_MAXHTPTV70_140_CFilterBVeto	e5299_s2726_r7772_r7676_p2949	1980.8000	0.98	0.113	22.646
364116	Sherpa_221_NNPDF30NNLO_Zee_MAXHTPTV70_BFilter	e5299_s2726_r7772_r7676_p2949	1981.7000	0.98	0.064	63.937
364117	Sherpa_221_NNPDF30NNLO_Zee_MAXHTPTV70_140_CVetoBVeto	e5299_s2726_r7772_r7676_p2949	110.5000	0.98	0.690	79.645
364118	Sherpa_221_NNPDF30NNLO_Zee_MAXHTPTV70_140_CFilterBVeto	e5299_s2726_r7772_r7676_p2949	110.6300	0.98	0.184	99.477
364119	Sherpa_221_NNPDF30NNLO_Zee_MAXHTPTV70_140_BFilter	e5299_s2726_r7772_r7676_p2949	110.3100	0.98	0.114	475.689
364120	Sherpa_221_NNPDF30NNLO_Zee_MAXHTPTV140_280_CVetoBVeto	e5299_s2726_r7772_r7676_p2949	40.7310	0.98	0.615	202.772
364121	Sherpa_221_NNPDF30NNLO_Zee_MAXHTPTV140_280_CFilterBVeto	e5299_s2726_r7772_r7676_p2949	40.6700	0.98	0.230	324.184
364122	Sherpa_221_NNPDF30NNLO_Zee_MAXHTPTV140_280_BFilter	e5299_s2726_r7772_r7676_p2949	40.6430	0.98	0.150	2078.998
364123	Sherpa_221_NNPDF30NNLO_Zee_MAXHTPTV280_500_CVetoBVeto	e5299_s2726_r7772_r7676_p2949	8.6743	0.98	0.561	407.078
364124	Sherpa_221_NNPDF30NNLO_Zee_MAXHTPTV280_500_CFilterBVeto	e5299_s2726_r7772_r7676_p2949	8.6711	0.98	0.263	444.808
364125	Sherpa_221_NNPDF30NNLO_Zee_MAXHTPTV280_500_BFilter	e5299_s2726_r7772_r7676_p2949	8.6766	0.98	0.172	1356.645
364126	Sherpa_221_NNPDF30NNLO_Zee_MAXHTPTV500_1000	e5299_s2726_r7772_r7676_p2949	1.8081	0.98	1.000	1686.255
364127	Sherpa_221_NNPDF30NNLO_Zee_MAXHTPTV1000_E_CMS	e5299_s2726_r7772_r7676_p2949	0.1486	0.98	1.000	6819.879
364128	Sherpa_221_NNPDF30NNLO_Ztautau_MAXHTPTV70_140_CVetoBVeto	e5307_s2726_r7772_r7676_p2949	1981.6000	0.98	0.821	4.982
364129	Sherpa_221_NNPDF30NNLO_Ztautau_MAXHTPTV70_CFilterBVeto	e5307_s2726_r7772_r7676_p2949	1978.8000	0.98	0.113	22.633
364130	Sherpa_221_NNPDF30NNLO_Ztautau_MAXHTPTV70_BFilter	e5307_s2726_r7772_r7676_p2949	1981.8000	0.98	0.064	63.352
364131	Sherpa_221_NNPDF30NNLO_Ztautau_MAXHTPTV70_140_CVetoBVeto	e5307_s2726_r7772_r7676_p2949	110.3700	0.98	0.689	80.065
364132	Sherpa_221_NNPDF30NNLO_Ztautau_MAXHTPTV70_140_CFilterBVeto	e5307_s2726_r7772_r7676_p2949	110.5100	0.98	0.183	99.508
364133	Sherpa_221_NNPDF30NNLO_Ztautau_MAXHTPTV70_140_BFilter	e5307_s2726_r7772_r7676_p2949	110.8700	0.98	0.111	493.213
364134	Sherpa_221_NNPDF30NNLO_Ztautau_MAXHTPTV140_280_CVetoBVeto	e5307_s2726_r7772_r7676_p2949	40.7810	0.98	0.608	204.914
364135	Sherpa_221_NNPDF30NNLO_Ztautau_MAXHTPTV140_280_CFilterBVeto	e5307_s2726_r7772_r7676_p2949	40.7400	0.98	0.229	326.848
364136	Sherpa_221_NNPDF30NNLO_Ztautau_MAXHTPTV140_280_BFilter	e5307_s2726_r7772_r7676_p2949	40.7610	0.98	0.134	923.313
364137	Sherpa_221_NNPDF30NNLO_Ztautau_MAXHTPTV280_500_CVetoBVeto	e5313_s2726_r7772_r7676_p2949	8.5502	0.98	0.560	422.313
364138	Sherpa_221_NNPDF30NNLO_Ztautau_MAXHTPTV280_500_CFilterBVeto	e5313_s2726_r7772_r7676_p2949	8.6707	0.98	0.262	444.352
364139	Sherpa_221_NNPDF30NNLO_Ztautau_MAXHTPTV280_500_BFilter	e5313_s2726_r7772_r7676_p2949	8.6804	0.98	0.173	1347.705
364140	Sherpa_221_NNPDF30NNLO_Ztautau_MAXHTPTV500_1000	e5307_s2726_r7772_r7676_p2949	1.8096	0.98	1.000	1668.876
364141	Sherpa_221_NNPDF30NNLO_Ztautau_MAXHTPTV1000_E_CMS	e5307_s2726_r7772_r7676_p2949	0.1483	0.98	1.000	6775.146

Table A.2: List of simulated Z+jets processes

Dataset ID	Process	Tags	Cross section [pb]	k-factor	Generator efficiency	$\mathcal{L}_{int}[\text{fb}^{-1}]$
410011	PowhegPythiaEvtGen_P2012_singletop_tchan_lept_top	e3824_s2608_s2183_r7725_r7676_p2949	43.7390	1.01	1.000	112.937
410012	PowhegPythiaEvtGen_P2012_singletop_tchan_lept_antitop	e3824_s2608_s2183_r7725_r7676_p2949	25.7780	1.02	1.000	189.903
410015	PowhegPythiaEvtGen_P2012_Wt_dilepton_top	e3753_s2608_s2183_r7725_r7676_p2949	3.5835	1.05	1.000	262.959
410016	PowhegPythiaEvtGen_P2012_Wt_dilepton_antitop	e3753_s2608_s2183_r7725_r7676_p2949	3.5814	1.05	1.000	262.690
410026	PowhegPythiaEvtGen_P2012_SingleTopSchan_noAllHad_antitop	e3998_s2608_s2183_r7725_r7676_p2949	1.2615	1.02	1.000	772.453
410025	PowhegPythiaEvtGen_P2012_SingleTopSchan_noAllHad_top	e3998_s2608_s2183_r7725_r7676_p2949	2.0517	1.00	1.000	484.101

Table A.3: List of simulated single-top processes

Dataset ID	Process	Tags	Cross section [pb]	k-factor	Generator efficiency	$\mathcal{L}_{int}[\text{fb}^{-1}]$
410000	PowhegPythiaEvtGen_P2012_ttbar_hdamp17p5_nonallhad	e3698_s2608_s2183_r7725_r7676_p2949	696.1100	1.19	0.543	109.345

Table A.4: List of the simulated $t\bar{t}$ sample

Dataset ID	Process	Tags	Cross section [pb]	k-factor	Generator efficiency	$\mathcal{L}_{int}[\text{fb}^{-1}]$
410218	aMcAtNloPythia8EvtGen_MEN30NNLO_A14N23LO_ttee	e5070_s2726_r7772_r7676_p2949	0.0369	1.12	1.000	34099.359
410219	aMcAtNloPythia8EvtGen_MEN30NNLO_A14N23LO_tmmumu	e5070_s2726_r7772_r7676_p2949	0.0369	1.12	1.000	34112.250
410220	aMcAtNloPythia8EvtGen_MEN30NNLO_A14N23LO_tttautau	e5070_s2726_r7772_r7676_p2949	0.0366	1.12	1.000	22792.877
410155	aMcAtNloPythia8EvtGen_MEN30NNLO_A14N23LO_twW	e5070_s2726_r7772_r7676_p2949	0.5483	1.10	1.000	12423.357
410081	MadGraphPythia8EvtGen_A14NNPDF23_ttbarWW	e4111_s2608_s2183_r7725_r7676_p2949	0.0081	1.22	1.000	5048.439
407321	MadGraphPythia8EvtGen_A14NNPDF23LO_ttbarWll	e5536_s2726_r7772_r7676_p2949	0.0003	1.34	1.000	84165.641

Table A.5: List of simulated $t\bar{t}$ plus vector boson processes

Dataset ID	Process	Tags	Cross section [pb]	k-factor	Generator efficiency	$\mathcal{L}_{int} [\text{fb}^{-1}]$
341079	PowhegPythia8EvtGen_CTI10_AZNLOCTEQ6L1_ggH125_WWlVv_EF_15_5	e3871_s2608_s2183_r7772_r7676_p2949	0.9902	1.00	0.491	983.382
341122	PowhegPythia8EvtGen_CTI10_AZNLOCTEQ6L1_ggH125_tautauall	e3935_s2608_s2183_r7772_r7676_p2949	1.9081	1.45	0.123	4467.140
341195	PowhegPythia8EvtGen_CTI10_AZNLOCTEQ6L1_ggH125_mumu	e3945_s2608_s2183_r7772_r7676_p2949	0.0066	1.45	1.000	99495.922
342178	PowhegPythia8EvtGen_CTI10_AZNLOCTEQ6L1_ggH125_ee	e4158_s2608_s2183_r7772_r7676_p2949	0.0000	1.45	1.000	293359648.000
341080	PowhegPythia8EvtGen_CTI10_AZNLOCTEQ6L1_VBFH125_WWlVv_EF_15_5	e3871_s2608_s2183_r7772_r7676_p2949	0.0848	1.00	0.510	5774.853
341155	PowhegPythia8EvtGen_CTI10_AZNLOCTEQ6L1_VBFH125_tautauall	e3888_s2608_s2183_r7772_r7676_p2949	0.2420	0.98	0.123	71518.055
341206	PowhegPythia8EvtGen_CTI10_AZNLOCTEQ6L1_VBFH125_mumu	e3945_s2608_s2183_r7772_r7676_p2949	0.0009	0.96	1.000	998280.062
342189	PowhegPythia8EvtGen_CTI10_AZNLOCTEQ6L1_VBFH125_ee	e4158_s2608_s2183_r7772_r7676_p2949	0.0000	0.98	1.000	5208568320.000
342284	Pythia8EvtGen_A14NNPDF23LO_WH125_inc	e4246_s2608_s2183_r7772_r7676_p2949	1.1021	1.25	1.000	72.029
342285	Pythia8EvtGen_A14NNPDF23LO_ZH125_inc	e4246_s2608_s2183_r7772_r7676_p2949	0.6007	1.45	1.000	114.075
341270	aMcAtNloHerwigppEvtGen_UEEE5_CTEQ6L1_CT10ME_ttH125_semilep	e4277_s2608_s2183_r7772_r7676_p2949	0.5085	1.00	0.439	4269.874
341271	aMcAtNloHerwigppEvtGen_UEEE5_CTEQ6L1_CT10ME_ttH125_allhad	e4277_s2608_s2183_r7772_r7676_p2949	0.5085	1.00	0.455	4112.265
341177	aMcAtNloHerwigppEvtGen_UEEE5_CTEQ6L1_CT10ME_ttH125_dil	e4277_s2608_s2183_r7772_r7676_p2949	0.5085	1.00	0.106	35645.684

Table A.6: List of simulated Higgs related processes, including Higgs plus vector boson production and $t\bar{t}H$ processes

Dataset ID	Process	Tags	Cross section [pb]	k-factor	Generator efficiency	$\mathcal{L}_{int} [\text{fb}^{-1}]$
361069	Sherpa_CTI10_llvvjj_ss.EW4	e3836_s2726_r7772_r7676_p2949	0.0258	0.91	1.000	20984.256
361070	Sherpa_CTI10_llvvjj_ss.EW6	e3836_s2608_s2183_r7772_r7676_p2949	0.0434	0.91	1.000	12363.429
361071	Sherpa_CTI10_lllvj_EW6	e3836_s2726_r7772_r7676_p2949	0.0423	0.91	1.000	25415.025
361072	Sherpa_CTI10_llljjj_EW6	e3836_s2608_s2183_r7772_r7676_p2949	0.0315	0.91	1.000	2093.411
361073	Sherpa_CTI10_ggllll	e3836_s2608_s2183_r7772_r7676_p2949	0.0210	0.91	1.000	26331.662
361077	Sherpa_CTI10_gglvv	e3836_s2608_s2183_r7772_r7676_p2949	0.8549	0.91	1.000	256.820
363356	Sherpa_221_NNPDF30NNLO_ZqqZll	e5525_s2726_r7772_r7676_p2949	15.5630	1.00	0.140	2447.129
363359	Sherpa_221_NNPDF30NNLO_WPqWmfv	e5583_s2726_r7772_r7676_p2949	24.7170	1.00	1.000	286.969
363358	Sherpa_221_NNPDF30NNLO_WqqZll	e5525_s2726_r7772_r7676_p2949	3.4370	1.00	1.000	1549.025
363360	Sherpa_221_NNPDF30NNLO_WPvWmqq	e5983_s2726_r7772_r7676_p2949	112.7400	1.00	1.000	63.110
363489	Sherpa_221_NNPDF30NNLO_WlvZqq	e5525_s2726_r7772_r7676_p2949	11.4130	1.00	1.000	622.098
363490	Sherpa_221_NNPDF30NNLO_llll	e5332_s2726_r7772_r7676_p2949	1.2557	1.00	1.000	14195.509
363491	Sherpa_221_NNPDF30NNLO_lllv	e5332_s2726_r7772_r7676_p2949	4.5877	1.00	1.000	3437.907
363492	Sherpa_221_NNPDF30NNLO_llvv	e5332_s2726_r7772_r7676_p2949	12.4650	1.00	1.000	1187.565

Table A.7: List of simulated diboson processes

Dataset ID	Process	Tags	Cross section [pb]	k-factor	Generator efficiency	$\mathcal{L}_{int} [\text{fb}^{-1}]$
407311	Sherpa_221_NNPDF30NNLO_6l0v_EW6	e5473_s2726_r7772_r7676_p2949	0.0001	1.00	1.000	478749.375
407312	Sherpa_221_NNPDF30NNLO_5l1v_EW6	e5473_s2726_r7772_r7676_p2949	0.0006	1.00	1.000	88080.891
407313	Sherpa_221_NNPDF30NNLO_4l2v_EW6	e5473_s2726_r7772_r7676_p2949	0.0044	1.00	1.000	11216.921
407314	Sherpa_221_NNPDF30NNLO_3l3v_EW6	e5473_s2726_r7772_r7676_p2949	0.0158	1.00	1.000	3029.156
407315	Sherpa_221_NNPDF30NNLO_2l4v_EW6	e5655_s2726_r7772_r7676_p2949	0.0058	1.00	1.000	10108.625

Table A.8: List of simulated triboson processes

Dataset ID	Process	Tags	Cross section [pb]	k-factor	Generator efficiency	$\mathcal{L}_{int} [\text{fb}^{-1}]$
364198	Sherpa_221_NN30NNLO_Zmm_MII10_40_MAXHTPTV0_70_BVeto	e5421_s2726_r7772_r7676_p2949	2413.7000	0.98	0.965	3.270
364199	Sherpa_221_NN30NNLO_Zmm_MII10_40_MAXHTPTV0_70_BFilter	e5421_s2726_r7772_r7676_p2949	2414.7000	0.98	0.034	18.427
364200	Sherpa_221_NN30NNLO_Zmm_MII10_40_MAXHTPTV0_280_BVeto	e5421_s2726_r7772_r7676_p2949	50.3180	0.98	0.892	54.088
364201	Sherpa_221_NN30NNLO_Zmm_MII10_40_MAXHTPTV0_280_BFilter	e5421_s2726_r7772_r7676_p2949	50.2850	0.98	0.102	217.538
364202	Sherpa_221_NN30NNLO_Zmm_MII10_40_MAXHTPTV280_E_CMS_BVeto	e5421_s2726_r7772_r7676_p2949	3.2355	0.98	0.853	220.507
364203	Sherpa_221_NN30NNLO_Zmm_MII10_40_MAXHTPTV280_E_CMS_BFilter	e5421_s2726_r7772_r7676_p2949	3.2800	0.98	0.144	538.250
364204	Sherpa_221_NN30NNLO_Zee_MII10_40_MAXHTPTV0_70_BVeto	e5421_s2726_r7772_r7676_p2949	2415.7000	0.98	0.965	3.253
364205	Sherpa_221_NN30NNLO_Zee_MII10_40_MAXHTPTV0_70_BFilter	e5421_s2726_r7772_r7676_p2949	2416.8999	0.98	0.034	18.605
364206	Sherpa_221_NN30NNLO_Zee_MII10_40_MAXHTPTV0_280_BVeto	e5421_s2726_r7772_r7676_p2949	50.4560	0.98	0.891	54.046
364207	Sherpa_221_NN30NNLO_Zee_MII10_40_MAXHTPTV0_280_BFilter	e5421_s2726_r7772_r7676_p2949	50.4270	0.98	0.109	203.183
364208	Sherpa_221_NN30NNLO_Zee_MII10_40_MAXHTPTV280_E_CMS_BVeto	e5421_s2726_r7772_r7676_p2949	3.2538	0.98	0.854	217.853
364209	Sherpa_221_NN30NNLO_Zee_MII10_40_MAXHTPTV280_E_CMS_BFilter	e5421_s2726_r7772_r7676_p2949	3.2519	0.98	0.145	539.771
364210	Sherpa_221_NN30NNLO_Ztt_MII10_40_MAXHTPTV0_70_BVeto	e5421_s2726_r7772_r7676_p2949	2417.8999	0.98	0.965	3.240
364211	Sherpa_221_NN30NNLO_Ztt_MII10_40_MAXHTPTV0_70_BFilter	e5421_s2726_r7772_r7676_p2949	2414.2000	0.98	0.034	18.720
364212	Sherpa_221_NN30NNLO_Ztt_MII10_40_MAXHTPTV0_280_BVeto	e5421_s2726_r7772_r7676_p2949	50.3700	0.98	0.890	54.057
364213	Sherpa_221_NN30NNLO_Ztt_MII10_40_MAXHTPTV0_280_BFilter	e5421_s2726_r7772_r7676_p2949	50.4400	0.98	0.110	200.586
364214	Sherpa_221_NN30NNLO_Ztt_MII10_40_MAXHTPTV280_E_CMS_BVeto	e5421_s2726_r7772_r7676_p2949	3.2834	0.98	0.851	217.328
364215	Sherpa_221_NN30NNLO_Ztt_MII10_40_MAXHTPTV280_E_CMS_BFilter	e5421_s2726_r7772_r7676_p2949	3.2788	0.98	0.143	530.539

Table A.9: List of simulated DrellYan processes

Dataset ID	Process	Tags	Cross section [pb]	k-factor	Generator efficiency	$\mathcal{L}_{int} [\text{fb}^{-1}]$
304014	MadGraphPythia8EvtGen_A14NNPDF23.3top_SM	e4324_a766_a818_r7676_p2949	0.0016	1.00	1.000	121951.219
410080	MadGraphPythia8EvtGen_A14NNPDF23.4topSM	e4111_s2608_s2183_r7725_r7676_p2949	0.0092	1.00	1.000	21607.096

Table A.10: List of simulated multi-top processes

Dataset ID	Process	Tags	Cross section [pb]	k-factor	Generator efficiency	$\mathcal{L}_{int}[\text{fb}^{-1}]$
301535	Sherpa_CTI0_eegammaPt10_35	e3952_s2608_s2183_r7725_r7676_p2949	52.7060	1.00	1.000	94.596
301536	Sherpa_CTI0_mumugammaPt10_35	e3952_s2608_s2183_r7773_r7676_p2949	52.7080	1.00	1.000	94.509
301890	Sherpa_CTI0_enugammaPt35_70	e3952_s2608_s2183_r7725_r7676_p2949	15.3480	1.00	1.000	32.525
301891	Sherpa_CTI0_enugammaPt70_140	e3952_s2608_s2183_r7725_r7676_p2949	1.5282	1.00	1.000	163.591
301892	Sherpa_CTI0_enugammaPt140	e3952_s2608_s2183_r7725_r7676_p2949	0.2415	1.00	1.000	1034.154
301893	Sherpa_CTI0_munugammaPt35_70	e3952_s2608_s2183_r7725_r7676_p2949	15.2720	1.00	1.000	32.674
301894	Sherpa_CTI0_munugammaPt70_140	e3952_s2608_s2183_r7725_r7676_p2949	1.5235	1.00	1.000	163.702
301895	Sherpa_CTI0_munugammaPt140	e3952_s2608_s2183_r7725_r7676_p2949	0.2418	1.00	1.000	1031.303
301896	Sherpa_CTI0_tauaugammaPt35_70	e3952_s2608_s2183_r7725_r7676_p2949	15.2970	1.00	1.000	32.568
301897	Sherpa_CTI0_tauaugammaPt70_140	e3952_s2608_s2183_r7725_r7676_p2949	1.5290	1.00	1.000	163.244
301898	Sherpa_CTI0_tauaugammaPt140	e3952_s2608_s2183_r7725_r7676_p2949	0.2426	1.00	1.000	1028.854
301899	Sherpa_CTI0_eegammaPt35_70	e3952_s2608_s2183_r7725_r7676_p2949	5.2420	1.00	1.000	95.383
301900	Sherpa_CTI0_eegammaPt70_140	e3952_s2608_s2183_r7725_r7676_p2949	0.3846	1.00	1.000	640.749
301901	Sherpa_CTI0_eegammaPt140	e3952_s2608_s2183_r7725_r7676_p2949	0.0472	1.00	1.000	5295.601
301902	Sherpa_CTI0_mumugammaPt35_70	e3952_s2608_s2183_r7725_r7676_p2949	5.2455	1.00	1.000	95.053
301903	Sherpa_CTI0_mumugammaPt70_140	e3952_s2608_s2183_r7725_r7676_p2949	0.3855	1.00	1.000	648.023
301904	Sherpa_CTI0_mumugammaPt140	e3952_s2608_s2183_r7725_r7676_p2949	0.0472	1.00	1.000	5275.190
301905	Sherpa_CTI0_tautaugammaPt35_70	e3952_s2608_s2183_r7725_r7676_p2949	5.2490	1.00	1.000	95.066
301906	Sherpa_CTI0_tautaugammaPt70_140	e3952_s2608_s2183_r7725_r7676_p2949	0.3848	1.00	1.000	649.135
301907	Sherpa_CTI0_tautaugammaPt140	e3952_s2608_s2183_r7725_r7676_p2949	0.0470	1.00	1.000	5295.056

Table A.11: List of simulated $V+\gamma$ processes

A.3 List of signal MC samples

References

- [1] *Standard Model of Elementary Particles*,
https://en.wikipedia.org/wiki/File:Standard_Model_of_Elementary_Particles.svg.
- [2] *Standard Model Feynman Diagram Vertices*,
https://en.wikipedia.org/wiki/File:Standard_Model_Feynman_Diagram_Vertices.png.
- [3] ATLAS Collaboration Collaboration,, *Search for squarks and gluinos in final states with jets and missing transverse momentum using 36 fb⁻¹ of $\sqrt{s} = 13$ TeV pp collision data with the ATLAS detector*, Tech. Rep. ATLAS-CONF-2017-022, CERN, Geneva, Apr, 2017.
<https://cds.cern.ch/record/2258145>.
- [4] S. Farrell, D. Gerbaudo, F. Legger, A. Mete, A. Taffard, E. Tolley, S. Upadhyay, and J. Wittkowski, *Search for electroweak production of chargino and neutralino in the final state $WH \rightarrow \ell^\pm \ell^\pm$ in pp collision data at $\sqrt{s} = 8$ TeV using the ATLAS detector*, Tech. Rep. ATL-COM-PHYS-2014-221, CERN, Geneva, Mar, 2014.
<https://cds.cern.ch/record/1670123>.
- [5] M. D'Onofrio, D. Miller, A. De Santo, A. Cervelli, J. Lorenz, N. Abraham, F. Alonso, D. Bogavac, R. Camacho Toro, R. El Kosseifi, G. E. Gallardo, Y. Gao, M. Gignac, M. Javurkova, O. Jinnouchi, D. M. Koeck, C. Y. Lo, S. Muanza, M. J. R. Olsson, D. Paredes Hernandez, R. Reece, C. Rizzi, I. Santoyo Castillo, B. Schumm, G. H. Stark, M. J. Sullivan, M. J. Swiatlowski, K. Todome, P. Tornambe, F. Trovato, Y. Tu, Y. Yamaguchi, and D. Zhang, *Search for chargino and neutralino production in final state with a Higgs boson, and missing transverse momentum at $\sqrt{s} = 13$ TeV*

- with the ATLAS detector*, Tech. Rep. ATL-COM-PHYS-2018-486, CERN, Geneva, May, 2018. <https://cds.cern.ch/record/2316315>.
- [6] A. Cervelli, G. Gallardo, J. Lorenz, D. M. Koeck, D. Paredes Hernandez, P. Tornambe, M. Javurkova, Y. Tu, D. Zhang, and C. Y. Lo, *Search for chargino and neutralino production in final states with two same-sign leptons, jets and missing transverse momentum at $\sqrt{s} = 13$ TeV with the ATLAS detector*, Tech. Rep. ATL-COM-PHYS-2017-1808, CERN, Geneva, Dec, 2017. <https://cds.cern.ch/record/2298595>.
 - [7] E. Mobs, *The CERN accelerator complex. Complexe des accélérateurs du CERN*, <https://cds.cern.ch/record/2197559>, General Photo.
 - [8] *The accelerator complex*, <https://home.cern/about/accelerators>.
 - [9] *Pulling together: Superconducting electromagnets*, <https://home.cern/about/engineering/pulling-together-superconducting-electromagnets>.
 - [10] *Cryogenics: Low temperatures, high performance*, <https://home.cern/about/engineering/cryogenics-low-temperatures-high-performance>.
 - [11] G. Aad, E. Abat, and J. Abdallah, *The ATLAS Experiment at the CERN Large Hadron Collider*, Journal of Instrumentation **3** (2008) S08003, <http://stacks.iop.org/1748-0221/3/i=08/a=S08003>.
 - [12] J. Pequenao, *Computer generated image of the whole ATLAS detector*, <https://cds.cern.ch/record/1095924>.
 - [13] J. Pequenao and P. Schaffner, *An computer generated image representing how ATLAS detects particles*, <https://cds.cern.ch/record/1505342>.
 - [14] *Different values of pseudorapidity shown against a polar grid*, https://commons.wikimedia.org/wiki/File:Pseudorapidity_plot.svg.
 - [15] ATLAS Collaboration Collaboration, *ATLAS magnet system: Technical Design Report, 1*. Technical Design Report ATLAS. CERN, Geneva, 1997. <http://cds.cern.ch/record/338080>.
 - [16] J. Pequenao, *Computer generated image of the ATLAS inner detector*, <https://cds.cern.ch/record/1095926>.

- [17] J. Pequenao, *Computer Generated image of the ATLAS calorimeter*,
<https://cds.cern.ch/record/1095927>.
- [18] ATLAS Collaboration Collaboration,, *ATLAS liquid-argon calorimeter: Technical Design Report*. Technical Design Report ATLAS. CERN, Geneva, 1996. <https://cds.cern.ch/record/331061>.
- [19] J. Pequenao, *Computer generated image of the ATLAS Muons subsystem*,
<https://cds.cern.ch/record/1095929>.
- [20] A. Barr, C. Lester, and P. Stephens, *m(T2): The Truth behind the glamour*,
J. Phys. **G29** (2003) 2343–2363, [arXiv:hep-ph/0304226 \[hep-ph\]](https://arxiv.org/abs/hep-ph/0304226).
- [21] C. Clement, G. Conti, J. Dietrich, A. Floderus, S. Fratina, S. French,
B. Gjelsten, E. Hines, B. Jackson, P. Klimek, T. Kono, F. Legger, C. Lester,
M. Morii, M. Medinnis, A. S. Mete, A. Petridis, P. Pralavorio, M. Relich,
T. Serre, A. Taffard, E. Thomson, B. Toggersson, M. Tylmad, R. Ueno,
S. Williams, J. Wittkowski, and M. Vincter, *Searching for direct gaugino
production and direct slepton production with two leptons and missing
transverse momentum at $\sqrt{s} = 8$ TeV*, Tech. Rep.
ATL-COM-PHYS-2013-911, CERN, Geneva, Jul, 2013.
<https://cds.cern.ch/record/1560083>.